Advances in
Particle Image Velocimetry

by

Andreas Fouras

B.Eng., M.Eng.Sci.

A Thesis submitted to Monash University

for the degree of

Doctor of Philosophy

November 2007

Faculty of Engineering

Monash Universty

Declaration for thesis based or partially based on conjointly published or unpublished work

In accordance with Monash University Doctorate Regulation 17/ Doctor of Philosophy and Master of Philosophy (MPhil) regulations the following declarations are made:

I hereby declare that this thesis contains no material which has been accepted for the award of any other degree or diploma at any university or equivalent institution and that, to the best of my knowledge and belief, this thesis contains no material previously published or written by another person, except where due reference is made in the text of the thesis.

This thesis includes five published peer reviewed papers and one manuscript still under review. The core theme of the thesis is particle image velocimetry. The ideas, development and writing up of all the papers in the thesis were the principal responsibility of myself, the candidate, working within the Division of Biological Engineering.

In the case of Chapters 2.2, 2.3, 3.2, 3.3, 4.2 & 4.3 my contribution to the work involved the following:

Thesis chapter	Publication title	Publication status	Nature and extent of candidate's contribution
2.2	An improved, free surface, topographic technique	Published	Initiated paper, performed experiments, wrote analysis software, analysed data, wrote manuscript, revised manuscript. (70%)
2.3	Measurement of instantaneous velocity and surface topography of a cylinder at low Reynolds number	Published	Conceived initial ideas, Initiated paper, performed experiments, analysed data, wrote manuscript, revised manuscript. (50%)
3.2	A Simple Calibration Technique for Stereoscopic Particle Image Velocimetry	Published	Conceived initial ideas, initiated paper, performed experiments, wrote analysis software, analysed data, wrote manuscript, revised manuscript. (60%)
3.3	Target-free stereo PIV: A novel technique with inherent error estimation and improved accuracy	Published	Conceived initial ideas, initiated paper, performed experiments, wrote analysis software, analysed data, wrote manuscript, revised manuscript. (60%)
4.2	Three-dimensional Synchrotron X-Ray Particle Image Velocimetry	Published	Conceived initial ideas, initiated paper, performed experiments, wrote analysis software, analysed data, wrote manuscript, revised manuscript. (60%)
4.3	Volumetric Correlation PIV: a New Technique for 3D Velocity Vector Field Measurement	Under review	Conceived initial ideas, initiated paper, performed experiments, wrote analysis software, analysed data, wrote manuscript, revised manuscript. (60%)

In order to generate a consistent presentation within the thesis, I have not renumbered sections of submitted or published papers.

Candidate: Andreas Fouras
Submitted: November 2007

Abstract

A number of papers reporting advances in particle image velocimetry (PIV) are presented. These papers describe a diverse range of techniques in the the areas of free-surface measurement, stereo particle image velocimetry (SPIV) and three-dimensional PIV.

New techniques are presented for measurement of free surface topography, which are valuable for those studies which directly require the measurement of topography, and for when researchers wish to exploit the relationship between the fluid pressure and free surface height. These techniques represent a substantial improvement on previous techniques: an increase in the spatial resolution of the measurements and the partial de-coupling of the quality of the results from the experience level of the practitioner.

An adaptation of this free surface topography technique to simultaneously measure both free surface topography and velocity field data is also presented. To the author's knowledge, no other such technique exists. The intimate relationship between pressure field and free surface topography is discussed.

A series of advances in SPIV are also presented. SPIV is a prominent tool in modern fluid mechanics investigations. The techniques outlined in these papers represent a significant contribution to that technique and therefore are poised to have a significant impact on fluid mechanics.

The calibration phase of SPIV is a significant contributor to both the total time (and hence expense) of performing SPIV measurements and the total error of those measurements. The calibration technology reported in the free surface topography techniques is applied to the calibration of SPIV. This technique results in a significant reduction in complexity of the SPIV process, saving time and money and potentially reducing many sources of error.

The thesis continues with an outline of the development of a SPIV technique utilising three cameras. This work, which builds heavily on the aforementioned SPIV advances, describes how the use of three cameras allows the practitioner to dispense with a separate calibration phase, thereby increasing the robustness of the technique, substantially reducing SPIV errors and allowing for inherent estimation of those errors.

A demonstration of a detailed error analysis of SPIV as a function of the errors of the constituent planar PIV processes and the stereo (geometrical) configuration of the cameras is also presented for both SPIV techniques.

The thesis concludes with a set of advances in PIV which extend the capability of PIV to measure velocity fields in three dimensions. These techniques offer measurements over three

dimensions, but utilising only a single perspective.

A description of the second ever successful implementation of X-ray PIV is presented. This work makes several significant advances over the previous work, including the development of a correction process for the effects of volumetric illumination as provided by an X-ray light source. These advances result in a significant reduction in errors. The paper then demonstrates the development of a new correlation analysis algorithm, which using certain assumptions, allows for the resolution of the full three-dimensional velocity vector field from a single perspective.

The final paper in this thesis continues with an extension to the concept of correlation analysis to yield a three-dimensional velocity vector field. This technique utilises the effect of focus in visible light imaging to allow the velocity to be resolved at each position in depth. A fully three-dimensional vector field without assumptions and without additional perspectives results. This technique offers substantial advantages over other three-dimensional techniques, both in terms of information density (with no limit to the number of vectors per image) and simplicity of experimental set-up (with identical set-up to standard, planar PIV).

Acknowledgments

This has been a long and difficult journey, one only made possible by the help and support of many people. To all the following people I send out my gratitude.

To Professor Kerry Hourigan, who never once directed me down any path, or denied me any other, but whose advice multiplied my skill, experience and love of research.

To Jon Hinwood who took me under his wing at a time when I needed it most, who had absolutely nothing to gain from it and didn't: I did, thank you.

To those who were co-owners of an office fridge in a time long past (in chronological order): David Nicholaides, Jim Kostas, Stephen Wade and John Cater. Those years that could have been so forgettable have many fond memories thanks to you.

To all the staff and students at FLAIR: John Sheridan for his support as both HOD and colleague; Mark Thompson for his advice of all kinds; Greg Sheard and Kris Ryan for the long conversations in their office; David LoJacono for the injection of energy and procrastination; and finally, Karlis Atvars, Anthony Buchanan and especially Jon Dusting for keeping the lab fun during those years - in between.

To the co-authors on the papers that make up this thesis. Writing a paper is a journey, and like all journeys its as much about the company as the destination.

To those staff at Monash who helped me in endless task of buying, building and assembling laboratory equipment, not because they where paid to, but because they could. My thanks go to Long Kim Goh, Mark Symmonds, Ken Sheridan, Hugh Venables and Alex Bain.

To my family. Thanks go to my father, mother, sister and brother for their endless pride, encouragement and understanding. Thanks to Helen's Family for going easier on the jokes than they had to. Thanks to Helen, Dimitri, Alexandra, Christina and Maria for being yourselves: my beautiful people.

Constituent Publications of the Thesis

FOURAS, A., HOURIGAN, K., KAWAHASHI, M. & HIRAHARA, H., "An improved, free surface, topographic technique", *Journal of Visualization,* (2006) 9(1), 49–56.

FOURAS, A., DUSTING, J. & HOURIGAN, K., "A Simple Calibration Technique for Stereoscopic Particle Image Velocimetry", *Experiments in Fluids,* (2007) 42(5), 799–810.

FOURAS, A., DUSTING, J., LEWIS, R. & HOURIGAN, K., "Three-dimensional Synchrotron X-Ray Particle Image Velocimetry", *Journal of Applied Physics,* (2007) 102, 064916, 1–6.

FOURAS, A., LO JACONO, D., SHEARD, G.J., & HOURIGAN, K., "Measurement of instantaneous velocity and surface topography of a cylinder at low Reynolds number", *In Proceedings of the IUTAM Symposium on Unsteady Separated Flows and Their Control (Eds: M. Braza & K. Hourigan),* Corfu, Greece, 18-22 June 2007.

FOURAS, A., LO JACONO, D. & HOURIGAN, K., "Target-free stereo PIV: A novel technique with inherent error estimation and improved accuracy", *Experiments in Fluids, (Available Online).*

FOURAS, A., LO JACONO, D. & HOURIGAN, K., "Volumeteric Correlation PIV: a New Technique for 3D Velocity Vector Field Measurement", *Experiments in Fluids, (Under Review).*

x

Contents

Chapter 1

Introduction

1.1   An Introduction to particle image velocimetry

Particle image velocimetry (PIV) is the most commonly used technique to measure velocity fields and associated properties in the field of fluid mechanics at this time. The two-dimensional region imaged by a camera is typically illuminated over a limited depth by the use of a thin laser sheet, allowing the statistical two-dimensional (2D) measurement to be applicable to any region of flow that is approximately 2D. This measurement works by discretising the 2D image into sampling windows and performing a cross correlation analysis between the sampling windows of frames taken a short time-interval (Δt) apart. The peak in the cross correlation typically represents the modal displacement inside the measurement volume over the time between exposures. The representative velocity inside that sampling window at that time is then simply the ratio of the displacement and the time separation.

Given its growing share of the interest of experimental researchers in this field over a period of time in excess of twenty years, inevitably a large number of excellent review articles describing the history of the technique of PIV exist. Examples of such works include the review article by Grant (1997) and the book on PIV by Raffel et al (1998). More recently, an interesting article outlining the historical development of PIV and making interesting suggestions for the future development of PIV has been written by Adrian (2005). Although a complete review of PIV will not be conducted here in this thesis, a short synopsis of PIV will be presented, followed by a discussion of particular aspects of PIV and how it relates to the work described in the six constituent papers of this thesis.

Over the two decades of use of PIV, many developments have been made to the technique. These developments include sub-pixel accuracy, spurious vector identification and rejection and attempts to increase the dynamic range of the technique.

One of the areas of highest interest in PIV development has been surrounding the idea of calculating the vector to sub-pixel accuracy. Local variation in correlation the peak is mainly due to the statistical certainty of non-integer displacements; interrogation of the local variation of the peak yields an estimate of sub-pixel component of the displacement (Willert and Gharib 1991). The width of the signal peak is typically twice the length of the particle diameter. In the unusual case where there are large displacement gradients inside the imaging plane, the peak is smeared by these gradients. The common solution to this is to estimate the gradients and distort the image to deconvolve, or 'un-smear', the peak against these distortions (Huang et al 1993) thus improving the signal to noise ratio.

Also of interest to many researchers has been the automation of the process of identifying spurious vectors. For many years the technique described in Westerweel (1994), which compares an individual vector to the local median and rejects them based on a user defined threshold, has been the standard. Recently, more advanced algorithms, which seek to avoid the necessity of a single user defined threshold, have been developed (Westerweel and Scarano 2005).

One of the biggest shortfalls of PIV is the lack of dynamic range of the measurements (Adrian 2005). Multi-grid measurement algorithms such as those developed in Westerweel et al (1997) and Scarano and Riethmuller (2000) give the advantages of high spatial resolution of small sampling windows and the high dynamic range of large sampling windows.

Since its inception, PIV has also developed in other ways. This development includes the addition of new techniques to the PIV family. These variants include stereo PIV techniques (Arroyo and Greated 1991; Willert 1997; Prasad 2000) which allow for three-component velocity vector measurements over a plane; and holographic PIV techniques (Zhang et al 1997; Pu and Meng 2000) which allow for three dimensional measurements to be made over a volume. Of most recent popularity, micro PIV (Santiago et al 1998; Meinhart et al 1999; Olsen and Adrian 2000b) has been developed which allows for the measurements to be preformed on micro-fluidics devices.

It appears that in general, the rate of advance is slowing. This is simply a natural indication of the maturity of PIV. However the popularity of the technique means that PIV is continuously under the scrutiny of the fluid mechanics research community and that further developments are inevitable.

Six research papers reporting advances in PIV constitute this thesis. These papers are grouped in pairs based around three basic topics: Topographic PIV, Stereo PIV and Volumetric PIV.

1.2   Topographic PIV

Water wave visualisation is important to the shipping and off shore mining industries. Water wave generation, interaction (Arabadzhi 1996) and evolution can have a number of implications on their design, such as the degree of vibration and erosion. Several interesting studies have also been performed on the dam bursting problem (Cochard and Ancey 2007) which have included visualisation of the water surface.

A number of fluid mechanics studies could benefit from the simultaneous measurement of both velocity field data (and related quantities such as vorticity) and surface topography. Recent examples of such studies are that by Fu and Rockwell of shallow flow around a circular cylinder (Fu and Rockwell 2005b) and the recent study by Buchanan et al (2007) of supersonic jet screech, using the hydraulic analogy. Typically, the free surface topography relates to the pressure field through the low Froude number modified equations of motion Preiswerk (1938).

Water wave visualisation can be achieved in a number of ways. The simplest way to reconstruct a water surface is to observe a number of floats in a grid. At some point in time, a photograph is taken and the heights of each float can be manually recorded. Similar approaches that detect water height at a particular point include pressure, capacitance and resistance gauges (Jahne et al 1994). These methods are intrusive to the flow/waves and are therefore of limited application. Non-intrusive wave visualisation on a water table has primarily been limited to optical techniques including stereo photography, shadowgraphy, laser slope gauges and optical displacement sensors (Brocher and Makhsud 1997). These methods have a number of shortcomings, including poor spatial resolution, low sensitivity and yield a lack of quantitative data. Refraction techniques have been reported to have the highest sensitivity to small waves (Jahne et al 1994). Laser slope gauges measure the gradient of a water surface by observing the refractional dislocation of a collimated laser beam between a reference (flat water) and test (wavy) condition. As the wave angle and height increases, the laser beam is deflected or dislocated further. Appropriate inclusions of lenses into the system can remove the effect of water height on dislocation and yield accurate slope information (Hughes et al 1977). Laser slope gauges are simple to create but only give 1D spatial resolution (or 2D in time) and their application is consequently limited.

The emergence of Speckle Photography followed by Digital Speckle Photography has facilitated the observation of optical inhomogeneities over entire test bodies (Fomim et al 1999). Speckle photography uses image correlation software to quantify the shift that a laser specklegram undergoes when observed through a test section. The distortion of the image can be related to

the system by pertinent physical equations. There is little in the literature discussing the use of refraction based water wave visualisation in 3-D. Zhang et al (1994) have developed a system that utilizes different sources of coloured light illuminating the free surface from different angles. The result is that the reflected light is colour coded by surface angle. Tanaka et al (2000) developed a system that measures the distortion of a collimated speckle pattern. This method in turn was based on the laser speckle techniques from which PIV itself has developed. This method is technically superior, but does require the use of a good quality laser and a high degree of skill to create a collimated speckle pattern. The reliability and quantity of data such a system can supply is strongly coupled to the skill of the operator.

1.3   Stereo PIV

Stereo Particle Image Velocimetry (SPIV) is now a well-established extension of traditional Particle Image Velocimetry (PIV) (Arroyo and Greated 1991; Willert 1997; Prasad 2000). SPIV offers several advantages over standard or planar PIV in cases where measured flow fields are three-dimensional. These advantages include the improved accuracy of in-plane components of the velocity field due to removal of perspective error and the resolution of the out-of-plane components themselves. Recent extensions of SPIV include three-dimensional high speed scanning (Hori and Sakakibara 2004), dual-time SPIV for acceleration measurement (Perret et al 2006), multi-plane SPIV (Schroder and Kompenhans 2004), and stereoscopic micro-PIV (Lindken 2006).

SPIV involves the reconstruction of a three-component velocity field in a two-dimensional plane using two velocity fields derived using PIV. This reconstruction process relies on both simple geometrical equations utilising basic information about the camera setup, and a complicated calibration step to relate information acquired on the image plane to events occurring in the object plane.

There are several ways of classifying SPIV methodologies. The first is by the means of obtaining the different perspectives on the imaging plane. The most common are translational and angular displacement. Of these, angular displacement systems with a Scheimpflug camera/lens configuration are the most popular Prasad (2000).

The SPIV reconstruction techniques, by which the inevitable distortion of the measurement field is taken into account and the two two-dimensional vector fields are reconstructed into a single three-dimensional vector field, can be catergorised as two-dimensional calibration-based reconstruction, three-dimensional calibration-based reconstruction and geometric reconstruction (Prasad 2000).

Geometric reconstruction mathematically relates the parameters of image acquisition and the measured two-dimensional velocity fields through ray tracing to the derived three-dimensional vector field (Prasad and Adrian 1993). It has been argued that as parameters become more complex, the process of geometric reconstruction becomes exponentially more difficult.

Two-dimensional calibration is similar to geometric reconstruction in that it uses information relating to imaging parameters to perform the reconstruction. It differs in that the distortion field is derived from the calibration process, rather than calculating distortion directly from the imaging parameters. In this way, the correction for distortion and the reconstruction are separated into two distinct processes.

Three-dimensional calibration based techniques, such as those described by Soloff et al (1997), are more commonly used than two-dimensional calibration. The main advantage of three-dimensional calibration is that no information regarding the geometric parameters of the stereoscopic image acquisition are required. Instead, a direct mapping function is derived between an object in three-dimensional space and its corresponding location in the image planes. The three-dimensional methods are similar to two-dimensional calibration techniques in that the distortion is corrected by a calibration in the imaging plane. The difference is that they also involve calibration from the object plane to a number of parallel planes near the imaging plane. This additional information frees the technique from the requirement of information relating to the imaging geometry as this information is inferred in the additional calibrations (Prasad 2000; Prasad and Adrian 1993; Raffel et al 1998; Soloff et al 1997).

An interesting idea, developed in Willert (1997) and further in Wieneke (2005), is to utilise the cross correlation of the particle images to generate additional information regarding the relative camera positions and image deformations. This approach has the advantage of correcting for the errors caused by misalignment of the calibration target and the laser sheet. The disadvantages of this approach include further complication of the SPIV technique. Furthermore, any differences in image distortions caused by different camera positions will result in degradation of correlation between images. This problem is tackled in Wieneke (2005) by de-warping the images prior to this step, which however adds further complexity and computational effort.

Almost all two-dimensional and three-dimensional calibration techniques utilise a calibration target, which consists of a discrete number of markers displaced on a regular Cartesian grid (Lawson and Wu 1997b). Typically these targets contain in the order of 100 such markers, i.e. approximately a 10×10 grid. The author believes that it is this limited approach that has largely dictated much of the development of these techniques. The images of the target are compared to the known

positional layout of the target and the relative positions of all markers on the calibration target. The exact method of this comparison varies depending on the PIV software being utilised but is largely based on the PIV algorithms themselves, and may even require the practitioner to manually identify markers in an image and link them to a corresponding marker on the target. The uncertainty in identifying the position of these markers by use of PIV software is proportional to the size of these markers. The calibration data are then fitted by a method such as least squares fitting, both linear and non-linear are used, to obtain general data applicable to the entire measurement region. The dependency of calibration techniques on precise knowledge of the target geometry introduces measurement error and further complicates the SPIV procedure.

1.4 Volumetric PIV

Since its general acceptance as a powerful measurement tool for fluid mechanics, researchers have been searching for means of increasing the dimensionality of PIV above the standard two component velocity measurement over a plane. Throughout the thesis, the mDnC notation will be used, where m represents the dimension of the measurement volume and n represents the dimension of the resolved displacements. As an example, two component velocity measurements over a plane are expressed as 2D2C measurements in this notation.

For three components of velocity vectors over a measurement plane, stereo PIV (SPIV) was one of the first variations in PIV methodology to be introduced. Since its first development (Arroyo and Greated 1991), through to more recent advances (Fouras et al 2007a,c), SPIV has been becoming better understood, more accurate and simpler to implement. With 2D3C systems, six of the nine terms of the velocity gradient tensor are available. In order to obtain all nine terms of the velocity gradient tensor, a pseudo 3D3C system is available by conducting SPIV on two adjacent planes. Multi-plane SPIV (Schroder and Kompenhans 2004; Kahler 2004) allows for differentiation across planes to obtain the remaining three spatial velocity gradients.

Holographic PIV (HPIV) (Barnhart et al 1994; Zhang et al 1997) allows for truly 3D3C velocity measurements. A broad range of HPIV variants are available, each with advantages and disadvantages. In-line HPIV, and more recently available Digital In-line HPIV, is perhaps the simplest and easiest to implement, but is limited by signal to noise ratio (SNR). Furthermore, a limited number of particles can be resolved and therefore a limited number of vectors is achievable. Off-axis HPIV, which does not have this limitation, is dramatically more complex to implement and requires considerable greater laser power. Although HPIV has demonstrated ability to accurately resolve 3D3C velocity fields, due to complexity and expense of implementation, HPIV has not

enjoyed wide popularity.

A different approach to that of Holography is Tomographic image reconstruction. Tomographic PIV (Elsinga et al 2006) utilises multiple cameras in different positions to image an illuminated volume. A 3D image pair is reconstructed and 3D cross-correlation analysis is performed. This new technique shows promise as an alternative 3D3C measurement tool. Unfortunately, like other techniques that reconstruct the image rather than the velocity field, this approach is also limited in the number of particles that can be resolved.

An elegant technique, simpler to implement, that achieves 3D3C results is defocusing PIV (Willert and Gharib 1992; Pereira et al 2000). This technique utilises a lens mask to alter the point spread function (PSF) of the imaging system. The mask creates a PSF that is asymmetric about the focal plane. Particles out of focus appear as triangles, which invert as they cross the focal plane. This technique allows particles to be tracked throughout the illuminated volume, producing 3D3C particle tracking velocimetry (PTV). However, as a PTV variant, this technique is necessarily limited in the number of particles that can be individually identified. Furthermore, the introduction of the lens mask substantially reduces the light gathering power of the imaging system. Despite these limitations, the technique is gaining popularity and has achieved some considerable success recently (Forouhar et al 2006). Another development similar to defocusing PIV is based on deconvolution imaging (Park and Kihm 2006). This once again allows the direct identification and measurement of particles in 3D space, allowing 3D3C PTV.

As discussed above, many techniques are available that have successfully resolved 3D3C vector fields. However, these techniques are typically based on the reconstruction of particle images, followed by either 3D cross-correlation or particle tracking analysis, which limits maximum spatial resolution. Furthermore, these techniques require additional or modified hardware not required for traditional PIV.

The ability to resolve the instantaneous velocity field across a three-dimensional volume is a highly desirable technology that has eluded fluid mechanics experimentalists. Three-dimensional holographic Particle Image Velocimetry (PIV) has reportedly been used to measure instantaneous turbulent flow fields in three dimensions (Zhang et al 1997), but this technique has several shortcomings. These include an immensely complex optical set-up for data acquisition and reconstruction (Pu and Meng 2000), a very poor signal to noise ratio, and the inability to record a time sequence of velocity fields. Scanned, multi-plane PIV (Brucker 1997) or Stereoscopic Particle Image Velocimetry (SPIV) (Hori and Sakakibara 2004) can be used to compile 3D flow fields, however scanning techniques require the data within each plane to be captured at different points

in time and therefore necessitate the interrogated flow to be stationary in time.

1.4.1 Volumetric X-ray PIV

As many traditional fields of fluid mechanics reach maturity and as the values of modern society shift, increasing attention has been paid to the application of fluid mechanics to the study of human health. This shift is demonstrated by the number of research articles published in this field. A review of research articles relating specifically to whole-field blood velocity measurements can be found in Vennemann et al (2007).

The potential applications for three-dimensional flow resolution inside closed, opaque vessels are numerous and significant. For instance, the detailed measurement of flow fields within blood vessels would facilitate more advanced research into the role of hemodynamics in the development and potential treatment of cardiovascular disease. Diseased conditions of the vasculature such as stenosis and aneurysm are the continued focus of much research (Ross 1993; Radermacher et al 2001). New techniques to measure the fluid dynamics properties of the blood flow through the affected vascalature with increased resolution and accuracy are key to developing new treatments and understanding of these diseases (Moore et al 1994; Anayiotos et al 1994; He and Ku 1996; Ku and Giddens 1987). Many current blood flow measurement techniques can only quantify peak systolic velocity, a single indicator of the average flow field. Fully 3D velocity measurements would also yield a number of more useful flow parameters such as flow rate, wall shear and turbulence levels. Other possible biomedical applications include the study of flow through optically opaque heart valves and artificial hearts, both of which are challenging flow geometries to evaluate.

It is problematic to measure flows within opaque vessels, such as blood vessels, using current technologies. Most common spatially resolved flow measurement techniques, such as PIV or SPIV, require clear optical access to the region of interest. Medical imaging techniques that have previously been used to measure flows *in vivo*, such as Ultrasonography and Magnetic Resonance Imaging (MRI), are generally restricted to velocity field measurements with spatial resolutions of millimeter precision.

X-ray imaging has also rarely been applied to flow measurement. Seeger et al (2001) tracked individual particles in a bubble column in three-dimensional space using dual X-ray detector systems. In general though, particle tracking velocimetry (PTV) leads to low levels of information being recorded as it relies on identification of individual tracers that must be present in low numbers, especially when used with volume illumination. Lee and Kim (2003) subsequently used PIV rather than PTV and achieved far higher resolution. PIV is a newer flow measurement technique

than PTV, however it is well established within the field of fluid mechanics. Importantly, it has been shown to be capable of accurately measuring instantaneous velocity fields that have a high dynamic range. In PIV, regions of fluid containing multiple tracer particles are imaged at two points in time separated by a known time interval, and processed using correlation software. This process produces correlation 'peaks' at separate sampling window locations across the interrogation region, which are then converted into velocity vectors by assuming that the mode value represents the average velocity within the window. As it is statistically based, PIV can work with poorer signal to noise ratios and higher particle numbers than PTV.

Using an X-ray light source to conduct PIV poses significant problems, particularly due to the fact that the fluid region is volume-illuminated. In PIV, the light source is ideally narrowed to a flat plane, meaning that only a single cross-section of the flow is interrogated and any velocity variations in the out-of-plane (or z) direction are not recorded. As the light sheet is thickened, the velocity variation in z is included within the imaged region, and contaminates the PIV signal. This is particularly serious for flows that vary significantly in the out-of-plane direction, such as a pipe flow viewed from the side. As Lee and Kim (2005) used a flow with a Poiseuille velocity profile, they were only capable of measuring pipe flow in a z-averaged sense. The problem of volume illumination is also currently endemic to micro-PIV (Meinhart et al 2000b; Olsen and Adrian 2000b). The amount of information contaminating the flow from outside the desired imaging plane is a function of the depth of focus and is therefore mostly controlled by the numerical aperture of the microscope lens. This makes resolution of velocity data in the z direction from a volume-averaged cross-correlated particle field even more advantageous. Synchrotron phase-contrast X-ray imaging is a powerful tool for anatomical measurement and offers much improved contrast over conventional imaging for biological tissues (Lewis 2004; Lewis et al 2005).

Lee and Kim (2005) have reported the 2D measurement of a duct flow using X-ray PIV. While the flow in the axial (x) and vertical (y) axes was presented, the flow in the out-of-plane direction (z), was not shown. However, any gradients in the z direction will certainly contribute to variation of the correlation peaks from which the 2D measurement was derived. Lee and Kim understood this and explained their substantial underestimation of the velocity field as being caused by the PIV measurement representing the mean velocity. However, PIV measures the modal, rather than the mean, velocity at each window location.

1.4.2   Volumetric Correlation PIV

It is well understood that particle images appear differently when they are not on the focal plane. Olsen and Adrian (2000*b*) discuss the effect of these out-of-focus particles on the measurement of the velocity field. In micro-PIV (μPIV) systems, the entire volume is illuminated. Therefore several aspects of an out-of-focus particle image contribute to the velocity measurements. These include the point spread function (PSF) of the imaging system which can be simplified in this case as the response of the imaging system to an impulse response as a function of distance from the focal plane.

Of interest, Meinhart et al (2000*a*) and Olsen and Adrian (2000*b*) introduced the depth of correlation parameter. It defines the depth over which particles significantly contribute to the correlation function z_{corr} for "simple flowfields". This relation must be modified if the flowfield contains either significant Brownian motion (Olsen and Adrian 2000*a*) or out-of-plane motion (Olsen and Bourdon 2003). It is important to note that for cases where the PSF does not match the aforementioned theory, it has been shown (Bourdon et al 2004) that the PSF can be readily measured experimentally.

It had previously been thought (Meinhart et al 2000*a*; Olsen and Adrian 2000*b*) that the major problem in μPIV is that the out-of-focus particles in as far as they contribute to the correlations produce bias. Therefore, several attempts have been made to overcome these difficulties by filtering, subtracting, and then tracking these particles. It is proposed here that the additional information provided by these out-of-focus particles should not be discarded. Instead, it provides the opportunity to resolve the displacement as a function of depth.

1.5   Continued development

It can be seen from the available literature that PIV is a mature technique with reducing scope for continued development of the basic technique. However, as the range of applications of PIV continues to expand and the range of variants of PIV (such as SPIV) continues to grow in number, that there is a continued need for development of PIV. The following papers provide a significant contribution to this much needed development.

Chapter 2

Topographic PIV

2.1   Overview

This chapter discusses two techniques for measurement of free surface topography, which may be of use for those studies which directly value the measurement of topography and when researchers wish to exploit the relationship between fluid pressure and local fluid elevation.
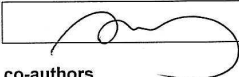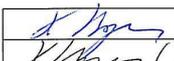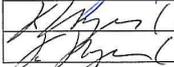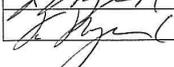
The chapter begins with a paper by Fouras et al (2006), which describes the development of a technique to measure free surface topography. This work is based largely on a similar technique (Tanaka et al 2000) which measures the deformation (refraction) of a laser speckle pattern when projected though a free surface by use of PIV analysis. This work represents a substantial improvement on the previous technique by the replacement of the laser speckle pattern by a image generated by the illumination of a ground glass plate with a pseudo-parallel light source. This method of illumination has two major benefits: the increase in the spatial resolution of the measurement technique caused by the increase in information density transmitted by the ground glass and the partial de-coupling of the quality of the results from the experience level of the practitioner. This second effect is a result of the ease-of-use and reproducibility of the speckle pattern created by the ground glass, while a laser speckle pattern of high quality can be difficult to produce.

The chapter continues with a paper by Fouras et al (2007*d*), which describes the adaptation of the free surface topography technique to simultaneously measure both free surface topography and velocity field data. To the author's knowledge, no other such technique exists. This paper also discusses the intimate relationship between pressure field and free surface topography and opens the door for the possibility of a technique which can measure both velocity and pressure field data as a function of time.

11

2.2 An improved, free surface, topographic technique

The following paper was published in 2006 in *Journal of Visualization*. This work was co-authored by K. Hourigan, M. Kawahashi and H. Hirahara, and is entitled *"An improved, free surface, topographic technique"*. The paper is reproduced in this thesis directly from the version published online.

Declaration

Declaration for manuscript included in PhD Thesis

Monash University

Declaration for Thesis Chapter 2.2

Declaration by candidate

In the case of Chapter 2.2, the nature and extent of my contribution to the work was the following:

Nature of contribution	Extent of contribution (%)
Initiated the paper, performed experiments, wrote analysis software, analysed data, wrote manuscript, revised manuscript.	70

The following co-authors contributed to the work. Co-authors who are students at Monash University must also indicate the extent of their contribution in percentage terms:

Name	Nature of contribution	Extent of contribution (%) for student co-authors only
Professor K. Hourigan	Co-wrote manuscript	N.A.
Professor M. Kawahashi	Collaboration led to initial idea, technical advice	N.A.
Professor H. Hirahara	Collaboration led to initial idea, technical advice	N.A.

Candidate's Signature		Date 08 NOV 07

Declaration by co-authors

The undersigned hereby certify that:

(1) the above declaration correctly reflects the nature and extent of the candidate's contribution to this work, and the nature of the contribution of each of the co-authors.
(2) they meet the criteria for authorship in that they have participated in the conception, execution, or interpretation, of at least that part of the publication in their field of expertise;
(3) they take public responsibility for their part of the publication, except for the responsible author who accepts overall responsibility for the publication;
(4) there are no other authors of the publication according to these criteria;
(5) potential conflicts of interest have been disclosed to (a) granting bodies, (b) the editor or publisher of journals or other publications, and (c) the head of the responsible academic unit; and
(6) the original data are stored at the following location(s) and will be held for at least five years from the date indicated below:

Location(s)	Division of Biological Engineering, Monash University.

		Date
Signature 1		8/11/2007
Signature 2	(HOD ON BEHALF OF M. KAWAHASHI)	8/11/2007
Signature 3	(HOD ON BEHALF OF H. HIRAHARA)	8/11/2007

An Improved, Free Surface, Topographic Technique

Fouras, A.*[1], Hourigan, K.*[1], Kawahashi, M.*[2] and Hirahara, H.*[2]

*1 Fluids Laboratory for Aeronautical and Industrial Research (FLAIR), Dept. Mechanical Engineering,
   Monash University, Wellington Road Clayton, Victoria 3800, Australia. Tel:+61-3-9905-9624 /
   Fax:+61-3-9905-9639, E-mail: Kerry.Hourigan@eng.monash.edu.au
*2 Dept. Mechanical Engineering, Saitama University, 255 Shimo-Okubo, Sakura-ku, Saitama-shi,
   Saitama 338-8570, Japan. Tel: +81-48-858-3443/Fax: +81-48-858-3711

Abstract: Current techniques of water wave visualisation such as shadowgraphy and stereo photography are widely used but are deficient in many aspects. Refraction based visualisation observes the bending of light as it traverses across a liquid-air interface. This work describes the continued development of techniques to measure the surface height of a liquid free surface. The method, Reference Image Topography, utilizes refraction of light at the free surface as a function of the local angle of that surface. Particle Image Velocimetry (PIV) software is used to evaluate apparent dislocations of the target image viewed through the free surface, which are approximately proportional to the surface angle. High-resolution images are presented of the dynamic surface topography for a point source and the shallow water flow around a vertical cylinder.

Keywords: Visualization, Free Surface, Topography, PIV

1. Introduction

Water wave visualisation is important to the shipping and off shore mining industries. Water wave generation, interaction and evolution can have a number of implications on their design, such as the degree of vibration and erosion.

Water wave visualisation can be achieved in a number of ways. The simplest way to reconstruct a water surface is to observe a number of floats in a grid. At some point in time, a photograph is taken and the heights of each float can be manually recorded. Similar approaches that detect water height at some point include pressure, capacitance and resistance gauges (Jahne et al., 1994). These methods are intrusive to the flow/waves and are therefore of limited application.

Non-intrusive wave visualisation on a water table has primarily been limited to optical techniques including stereo photography, shadowgraphy, laser slope gauges and optical displacement sensors (Brocher and Makhsud, 1997). These methods have a number of shortcomings, including poor spatial resolution, low sensitivity and yield a lack of quantitative data.

Refraction techniques have been reported to have the highest sensitivity to small waves (Jahne et al, 1994).

Laser slope gauges measure the gradient of a water surface by observing the refractional dislocation of a collimated laser beam between a reference (flat water) and test (wavy) condition. As the wave angle and height increases, the laser beam is deflected or dislocated further. Appropriate inclusions of lenses into the system can remove the effect of water height on dislocation and yield accurate slope information (Hughes et al., 1977). Laser slope gauges are simple to create but only give 1D spatial resolution (or 2D in time) and their application is consequently limited.

50   An Improved, Free Surface Topographic Technique
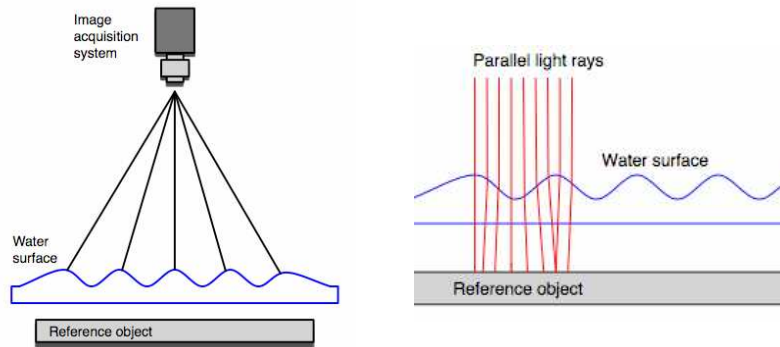

Figure 1: (a) Schematic of system showing reference object, liquid surface, image acquisition system and general case of ray tracing. (b) Ray tracing diagram showing light rays from illuminated reference object being refracted at liquid surface. In this case imaging system is sufficiently far from liquid surface that rays traveling from liquid surface are nearly parallel.

The emergence of Speckle Photography followed by Digital Speckle Photography has facilitated the observation of optical inhomogeneities over entire test bodies (Fomim et al., 1999). Speckle photography uses image correlation software to quantify the shift that a laser specklegram undergoes when observed through a test section. The distortion of the image can be related to the system by pertinent physical equations.

There is little in the literature discussing the use of refraction based water wave visualisation in 3-D. Hence it is the purpose of this investigation to design, fabricate and test a system that reconstructs the topography of a water surface with reference to a distorted image. This work describes the continued development of techniques to measure the surface height of a liquid free surface. The method utilizes refraction of light at the free surface as a function of the local angle of that surface. This method utilizes Particle Image Velocimetry (PIV) interrogation of a target image viewed through the free surface.

Similar methods have been developed by at least two groups.

Zhang et al. (1994) have developed a system that utilizes different sources of coloured light illuminating the free surface from different angles. The result is that the reflected light is colour coded by surface angle. Tanaka et al. (2000) developed a system that measures the distortion of a collimated speckle pattern. This in turn was based on the laser speckle techniques from which PIV itself has developed. This is a technically superior system, but does require the use of a good quality laser and a high degree of skill to create a collimated speckle pattern. The reliability and quantity of data such a system can supply is strongly coupled to the skill of the operator. The system outlined in this paper is a variation of the system developed in Tanaka et al., leading to a simpler, more economical and more accessible system.

2. Methodology

The current system is based on the simple concept of viewing a reference image through the free surface. By imaging this reference while the free surface is still (and level) and then at later times when the surface is disturbed, we can compare the images using any PIV software. By performing ray tracing, it is then possible to establish the local free surface angle as a function of the measured local displacement of the reference image. In the simplest case of ray tracing, the light from the wavy surface being collected by the imaging system is parallel. To satisfy this condition,

51   Fouras, A., Hourigan, K., Kawahashi, M. And Hirahara, H.

collimating optics are employed between the free surface and the camera, or the ratio of the camera to surface distance and surface to reference distance is sufficiently high and the local surface angle is directly proportional to the reference distortion.

The reference object used is a ground glass plate illuminated by a nearly parallel white light source (see Figure 1). Ordinary light globes, placed inside a long aspect ratio box, lined with reflective coating, back illuminate the semi-translucent reference object. This reference image setup is very inexpensive, requires little skill to operate and yields PIV performance of high quality with excellent reproducibility.

PIV analysis performs best when it tracks particles in a flow that are of the order 5 pixels. The glass plate was coarsely sand blasted to give the best image quality with image grains of this order. The glass plate can be replaced to suit the required field of view and camera resolution and maintain this image grain size. In this way, the performance of the PIV can be maximized.

The pattern on the speckled reference image is more uniformly distributed and more evenly illuminated than a typical laser illuminated PIV image or laser specklegram. The authors have found standard PIV software can obtain sufficient information from laser speckle images to achieve good signal to noise ratio with interrogation window sizes of 32 pixels square. This means independent measurements are spaced 32 pixels apart. With ground glass images the data density is so much higher that a higher signal to noise ratio can be achieved with interrogation windows of 8 pixels square and an acceptable quality at 4 pixels square. This leads to a linear increase in data density of at least a factor of 4 and a total increase in the quantity of measurements of a factor of between 16 and 64.

The rate at which this system can acquire free surface elevation fields is limited only by the rate at which the camera system employed can capture single frames of data. Black and white cameras of moderate framing rate are relatively inexpensive. While the framing rate of a given imaging system is partly limited by the intensity of the illumination system, very bright lights can be purchased quite inexpensively. As opposed to most PIV type systems, the images are compared to a single reference image captured during setup and not to an image captured over an interrogation time scale, which is small. This means that simpler, standard cameras can be utilized as opposed to double framing cameras-which are typically used for cross correlation PIV image acquisition. These simpler cameras are at least 3-4 times cheaper than their more complex counterparts.

The reference image (image acquired under still conditions) is compared to each image taken under wavy conditions in turn. The images will appear to have local distortions whereby relative local displacements can be measured using a standard PIV analysis of each image pair.

As mentioned above, these relative displacements between images are directly proportional to the 2D angle vectors dh/dx and dh/dy, where h is the liquid free surface elevation. The constant of proportionality can be readily achieved either by direct calibration of the system or by mathematical analysis.

A straightforward integration of these vectors then yields the scalar quantity h at all points. Since this set of derivatives over-specifies the scalar quantity, sophisticated integration schemes can be used to significantly reduce the signal to noise ratio. The use of this additional information is of significant benefit and means that even relatively noisy gradient data can yield highly accurate elevation data.

3. Validation of Methodology

To validate the technique, the surface of a portion of wavy glass was measured. This offered substantial benefits, in terms of validation, over measuring wavy water surfaces because the glass can easily be measured for surface properties allowing not only quantitative comparison of the nature of the wavy features of the glass but also their height. Figure 2 shows both a photograph (a) and a shadowgraph (b) of the glass plate used.

(a)

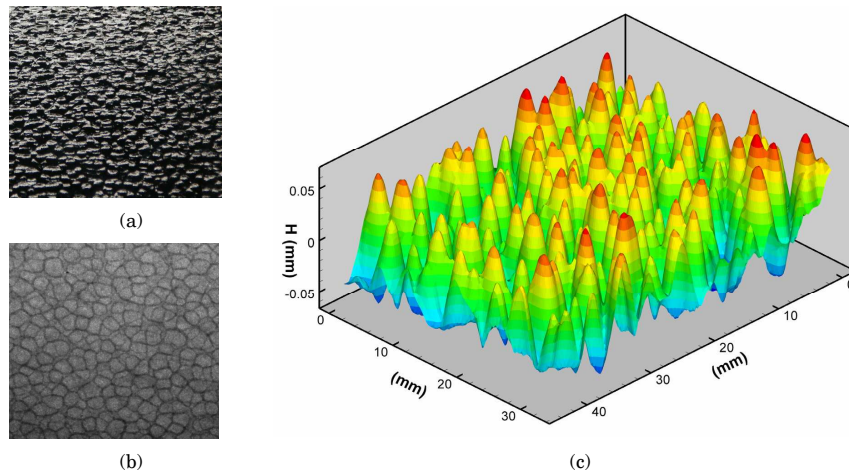(b)   (c)

Figure 2: Photo (a) and shadowgraph (b) of a wavy glass panel used to validate surface heights measured using the surface topographic technique. Figure 2 (c): Surface plot of height elevation data of same portion of wavy glass. Notice contour lines and surface elevation heights listed on H-axis (scaled by 100 to show detail).

Shown in figure 2(c) are the results of this calibration. The heights of wavy features in the surface of the glass were measured by passing an extremely fine pointed dial gauge along straight-line paths over the glass surface. Over the measurement area, the peak to trough displacement, was measured to be 0.005"+/-0.0002" or 0.127mm with an uncertainty of 4%. From the free surface topographic measurements taken of the same area, a peak to trough displacement of 0.125mm was measured. This falls well within the measurement uncertainty. The shape and spatial distribution of the surface waves on the glass were also found to match the measurements. This provides validation of the ray tracing methodology and in particular the quantitative nature of the measurement. Further validation of the technique was achieved by measurement of several predictable water wave conditions in a ripple tank and shallow water table.

4. Results and Discussion

The system has been extensively validated and calibrated against many known surface wave conditions, such as the double slit, various reflecting conditions and, reported here, a periodic point source and the shallow flow around a vertical circular cylinder. The first experiment was conducted by measuring the surface waves created by applying a point source disturbance of varying frequency and amplitudes. Both the spatial and temporal wave characteristics were found to be well captured.

In the present experiments, images were recorded for a point source generating waves. Shadowgraphy is a traditional qualitative method for viewing wave patterns on water. A shadowgraph and matching photograph of the radially emanating waves in the ripple tank is indicated in Figure 3. A periodic source produces a series of circular waves at expanding radii.

Figure 4 illustrates the results of the free surface topographic technique applied to the wavy conditions for a forcing frequency of 2 Hz in the form of (a) a PIV vector plot, (b) a rendered surface elevation plot and (c) a projection of the reconstructed heights coloured by height values.

In Figure 4, the patterns we would expect and that can be seen from the photograph of the experimental setup in Figure 3 are clearly visible. When the sequence of images was scrolled through, clear evidence of wave movement could be resolved. In Figure 4a, the surface displacement gradient vectors point towards the troughs and away from the crests. The rendered

53   Fouras, A., Hourigan, K., Kawahashi, M. And Hirahara, H.

surface elevation plot shows the water surface in striking detail. As an aid to visualization the data (measured on the right hand side) have been mirrored about the plane of symmetry passing through the point source. The clarity and spatial resolution of the data is such that the interference pattern formed by the primary waves and the secondary waves caused by their reflection at the nearby wall of the apparatus (seen in Figure 4b) are clearly visible.

The authors stress that the data in figure 4 are quantitative representing over 250,000 discrete measurements of the height of the liquid surface. The same data can be readily displayed as a contour plot to allow easier extraction of quantitative information on the surface elevation.

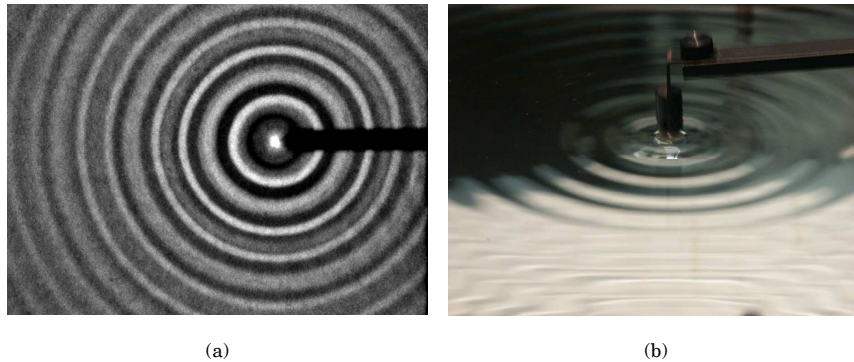(a)   (b)

Figure 3: Shadowgraph (a) and photograph (b) of ripple tank used to conduct experiments shown in figure 4. This qualitative visualization shows the familiar concentric rings formed when a liquid surface is disturbed. As the apparatus used was quite small, reflected waves can be seen at the top and more clearly at the bottom of this photograph.

Further interesting scope for the use of this technique has been highlighted by recent study by Fu and Rockwell (2005). This work has been focused on the flow around simple bodies submerged in shallow water. In this case, the flow studied was flow around a circular cylinder (diameter D) at a Reynolds number of 500 and at a depth of 0.8 D. Shown in Figure 5 is the wake immediately behind the cylinder in this flow. Consistent with the results of Fu and Rockwell (2005), the wake pattern observed here is very nearly symmetric. This demonstrates that substantially different mechanisms control this flow than those at work in the more fully immersed or deep water case. While a study of this flow is beyond the scope of this work, it highlights the utility of this technique and is well worth further investigation in the near future.

Finally, it should be pointed out that there are fundamental differences between Speckle Photography and the current method, Reference Image Topography. In Speckle Photography, the camera must be defocused from a speckle image in order to record the shift associated with refractive index change. In laser Speckle Photography, a single beam is observed. That is, the same beam is tracked from the reference to the test situation. The test and reference images can be sharply focused and still result in image dislocation. However, the optical system of Reference Image Topography requires no defocus from the speckle source, since there are no "preferred rays". This method is unlikely to suffer from the meticulous defocusing problems associated with Speckle Photography.

5. Conclusions

The method of Reference Image Topography to investigate liquid surface distortions has been economized and improved. A number of existing technologies and theories to reconstruct a water surface have been integrated into the diagnostic system.

54   An Improved, Free Surface Topographic Technique
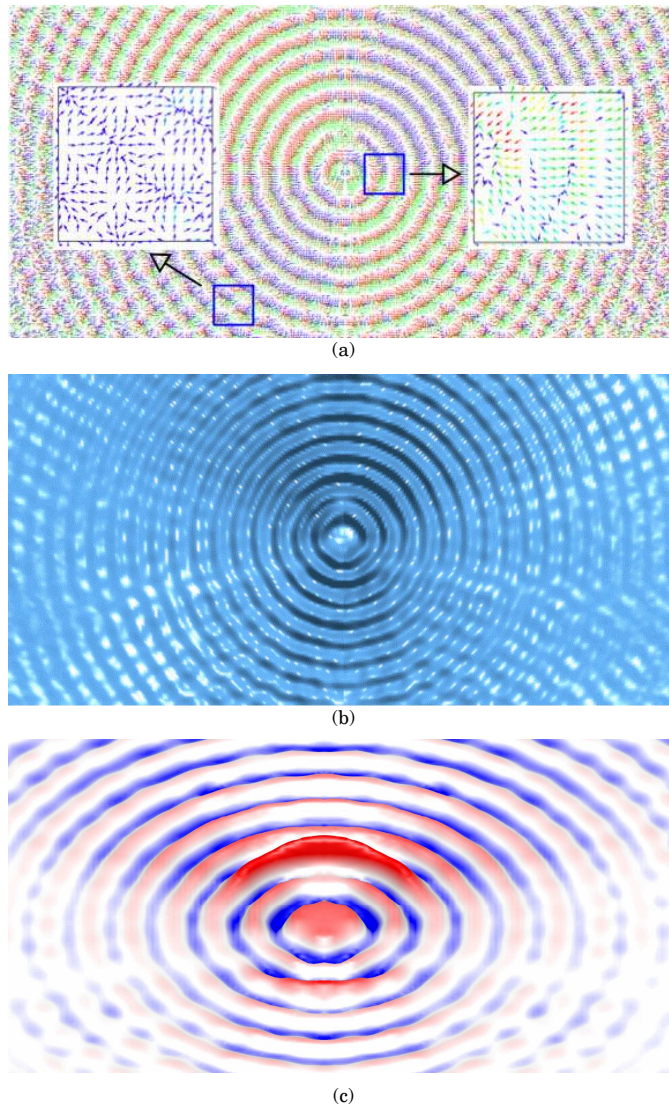

(a)

(b)

(c)

Figure 4: Mirrored surface plot of (a) vector dislocation data (vectors are drawn with fixed length and are coloured by magnitude) (b) rendered surface elevation data (c) projection of surface elevation measurements coloured by height.
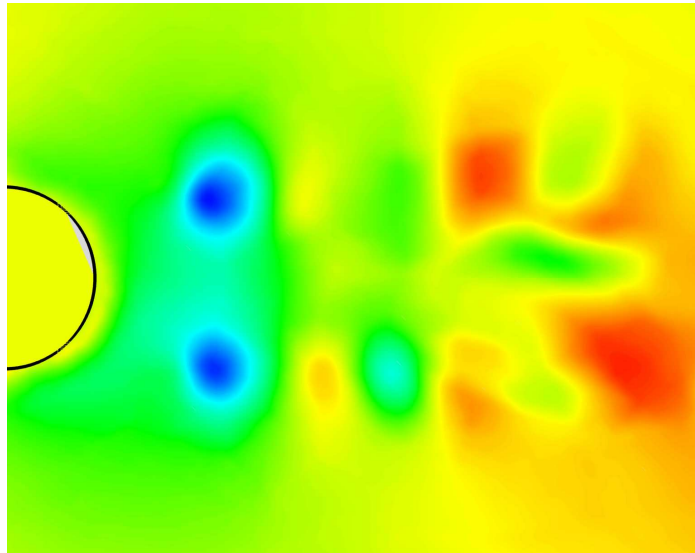
55   Fouras, A., Hourigan, K., Kawahashi, M. And Hirahara, H.

Figure 5: surface height measurements of the wake behind a circular cylinder at a Reynolds number of 500 and at a depth of 0.8 D. Yellow indicates neutral height, green/blue and red indicate below and above neutral respectively.

This optical system has been designed to capture the distortions/dislocations that emerge when water waves travel along a test section. The rig designed uses a speckled glass light box and a camera mounted below and above the test section respectively to capture the reference (still water) and test (wavy water) images.

The correlation of images has been successfully achieved using PIV software to quantify the dislocation between the reference and test speckled images. A sound physical relation approximation has been devised to relate the dislocation of an image into surface angles. A surface reconstruction program facilitates the visualisation of the water surface. This software utilizes the over specification of the integral equations to substantially improve signal to noise ratio.

The system has yielded some visualisations of wave structures that were produced by a point source. These visualisations capture detailed quantitative fields of surface distortions. While not shown here time resolved measurements of similar phenomena have been achieved. The system has also accurately resolved the detail of the surface of a piece of wavy glass, measuring the heights of those waves to within accuracy of the measurements of those heights.

The current system is inexpensive, requiring only standard light globes for an illumination source in the place of a laser, and can use any kind of camera for imaging. This is a relative cost saving of approximately three orders of magnitude for the light source and at least a factor of three for the camera. Furthermore, by using sandblasted glass as the reference image, not only is superior image quality possible, but also repeatability is guaranteed, with quality of results being substantially de-coupled from the skill and experience of the practitioner. By the use of a least squares or similar integration scheme, the signal to noise ratio of the system is further improved.

In conclusion, Reference Image Topography is potentially a very effective means for studying water waves simply and economically. Further testing on the system will be undertaken. Nevertheless, there exists a potential for the wider application of the technology in topographical characterisation involving transparent test media.

56   An Improved, Free Surface Topographic Technique

References

Adrian, R. J., Particle-imaging techniques for experimental fluid mechanics, Ann. Rev. Fluid Mech., 23 (1991), 261.

Brocher, E., Makhsud, A., New look at the screech tone mechanism of underexpanded jets, Eur. J. Mech. B/Fluids, 16(1997), 877.

Fomim, N., Lavinskaja, E., Merzkirch, W., Vitkin, D., Speckle photography applied to statistical analysis of turbulence, Optics & Laser Tech., 31 (1999), 13.

Fu, H. and Rockwell, D., Shallow flow past a cylinder: Control of near wake, JFM, 539 (2005), 1.

Hughes, H.A., Grant, H.L., Chappell, R. W., A fast response surface-wave slope meter and measured wind-wave moments, Deep-Sea Research, 24 (1977), 1211.

Jahne, B., Klinke, J., Waas, S., Imaging of short ocean wind waves: a critical theoretical review, J. Opt. Soc. Am. A, 11(1994), 2197.

Tanaka, G., Okamoto, K., Madarame, H., Experimental investigation on the interaction between a polymer solution jet and a free surface, Exp. Fluids, 29 (2000), 178.

Zhang, X., Dabiri, D., Gharib, M., A novel technique for free surface elevation mapping, Phys. Fluids 6(1994), S11.

Author Profile

Andreas Fouras: He received his M.Eng.Sci. in Mechanical Engineering in 1998 from Monash University. He has worked at Monash University since then in the areas of Quantitative Imaging, Quantitative Flow Visualisation and Bluff Body Turbulence. His particular area of interest is PIV technique and software development.

Kerry Hourigan: He is Professor of Mechanical Engineering, Director of the Biomedical Engineering Technology Alliance (MuBeta) and a Director of the Fluids Laboratory for Aeronautical and Industrial Research (FLAIR) at Monash University. Professor Hourigan obtained his Ph.D. in astronomy from Monash University in 1981 and was a NASA/NRC Research Associate at Caltech Jet Propulsion Laboratory (1982-83), a Senior Principal Research Scientist at the CSIRO (1984-95), and a visiting professor at Caltech GALCIT, Saitama University, Universite d'Aix-Marseille and IMF, Toulouse. His research interests include: aerodynamics, biomedical and biofluids engineering, optical diagnostics, CFD, and bluff body wakes and vortex induced vibration.

Masaaki Kawahashi: He received his MSc (Eng) degree in mechanical engineering in 1968 from University of Electro-Communication (UEC), and his PhD (Eng) from The University of Tokyo in 1978. After graduating from UEC, he joined at Saitama University as Research Associate. His current position is Professor of Fluid Dynamics in Department of Mechanical Engineering, Saitama University. His research subjects are finite amplitude wave motion, development of acoustic compressor, PIV applications to centrifugal fan, analysis of oscillatory air-flow in bronchial model by using micro-PIV.
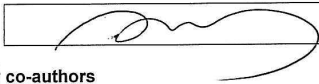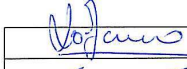

Hiroyuki Hirahara: He received his Master of Mechanical Engineering degree in 1983, and his Doctor of Engineering degree in 1986 in Kyushu University. After the DE course, he worked in atomic power plant engineering section in Toshiba Co.Ltd. He worked as a Research Assistant and Lecturer of Saitama University, before taking up his current position. He is an Associate Professor of Saitama University, and his research subjects are high speed flow, supersonic flow with condensation and evaporation, flow measurement techniques, optical measurement techniques, development of micro wind turbines and creature's flow simulation.

2.3 Measurement of instantaneous velocity and surface topography of a cylinder at low Reynolds number

The following paper was presented in 2007 at the *IUTAM Symposium on Unsteady Separated Flows and Their Control*. This work was co-authored by D. Lo Jacono, G.J. Sheard and K. Hourigan, and is entitled *"Measurement of instantaneous velocity and surface topography of a cylinder at low Reynolds number"*. The paper is reproduced in this thesis directly from the version published in the proceedings.

Declaration

Declaration for manuscript included in PhD Thesis

Monash University

Declaration for Thesis Chapter 2.3

Declaration by candidate

In the case of Chapter 2.3, the nature and extent of my contribution to the work was the following:

Nature of contribution	Extent of contribution (%)
Conceived initial ideas, initiated the paper, performed experiments, analysed data, wrote manuscript, revised manuscript.	50

The following co-authors contributed to the work. Co-authors who are students at Monash University must also indicate the extent of their contribution in percentage terms:

Name	Nature of contribution	Extent of contribution (%) for student co-authors only
Dr D. LoJacono	Performed experiments, analysed data	N.A.
Dr G. Sheard	Wrote analysis software, co-wrote manuscript	N.A.
Professor K. Hourigan	Co-wrote manuscript	N.A.

Candidate's Signature		Date 08 NOV 07

Declaration by co-authors

The undersigned hereby certify that:

(7) the above declaration correctly reflects the nature and extent of the candidate's contribution to this work, and the nature of the contribution of each of the co-authors.
(8) they meet the criteria for authorship in that they have participated in the conception, execution, or interpretation, of at least that part of the publication in their field of expertise;
(9) they take public responsibility for their part of the publication, except for the responsible author who accepts overall responsibility for the publication;
(10) there are no other authors of the publication according to these criteria;
(11) potential conflicts of interest have been disclosed to (a) granting bodies, (b) the editor or publisher of journals or other publications, and (c) the head of the responsible academic unit; and
(12) the original data are stored at the following location(s) and will be held for at least five years from the date indicated below:

Location(s)	Division of Biological Engineering, Monash University.

		Date
Signature 1		
Signature 2		
Signature 3		

MEASUREMENT OF INSTANTANEOUS VELOCITY AND SURFACE TOPOGRAPHY

Measurement of Instantaneous Velocity and Surface Topography of a Cylinder at Low Reynolds Number

Andreas FOURAS[1,2]**, David LO JACONO**[2]**, Gregory J. SHEARD**[2] **and**

Kerry HOURIGAN[1,2]

[1] *Division of Biological Engineering, Monash University, Australia.*
[2] *Fluids Laboratory for Aeronautical and Industrial Research (FLAIR), Department of Mechanical Engineering, Monash University, Australia.*

Abstract. A technique capable of simultaneous measurement of free surface topography and velocity vector field data is developed. This technique offers substantial benefits of both reduced complexity and enhanced accuracy over all other techniques known to offer the same measurements. The flow behind a circular cylinder at low Reynolds numbers is measured using this technique. The velocity and vorticity fields as well as Strouhal number closely match the expected results. The free surface topography, which can be related to the pressure field, exhibits an intimate relationship to the vorticity field.

Key words: PIV, pressure field, wake.

1. Introduction

A number of fluid mechanics studies could benefit from the simultaneous measurement of both velocity field data (and related quantities such as vorticity) and surface topography. Recent examples of such studies are the study by Fu *et al.* [7] of shallow flow around a circular cylinder and the recent study by Buchanan *et al.* [2] of supersonic jet screech, using the hydraulic analogy. Typically, the free surface topography relates to the pressure field through the low Froude number modified equations of motion [2].

A number of point and area measurement techniques have been developed over recent decades to measure the free surface topography. The most promising of these techniques are the optical area measurement techniques detailed in Tanaka *et al.* [11] and Zhang *et al.* [14]. These techniques were enhanced by Fouras *et al.* [4] with a new technique that is more accurate and simpler to implement.

2. Methodology

The new technique described in this paper is based on an integral combination of Particle Image Velocimetry (PIV) [9] and the reference image topography technique described in [4]. In this technique, experiments are conducted in a glass bottomed water table. The water is seeded with particles and the horizontal plane (selected as the plane for velocity measurement) is illuminated by a laser sheet. Twin cameras are symmetrically installed on the water table with one above the free surface and

1

Top Camera

Water surface   Laser sheet
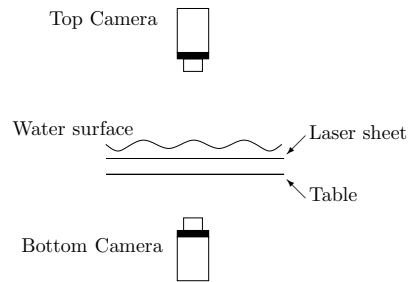
Table

Bottom Camera

Figure 1. Schematic of the configuration of cameras and light sheet relative to the surface.
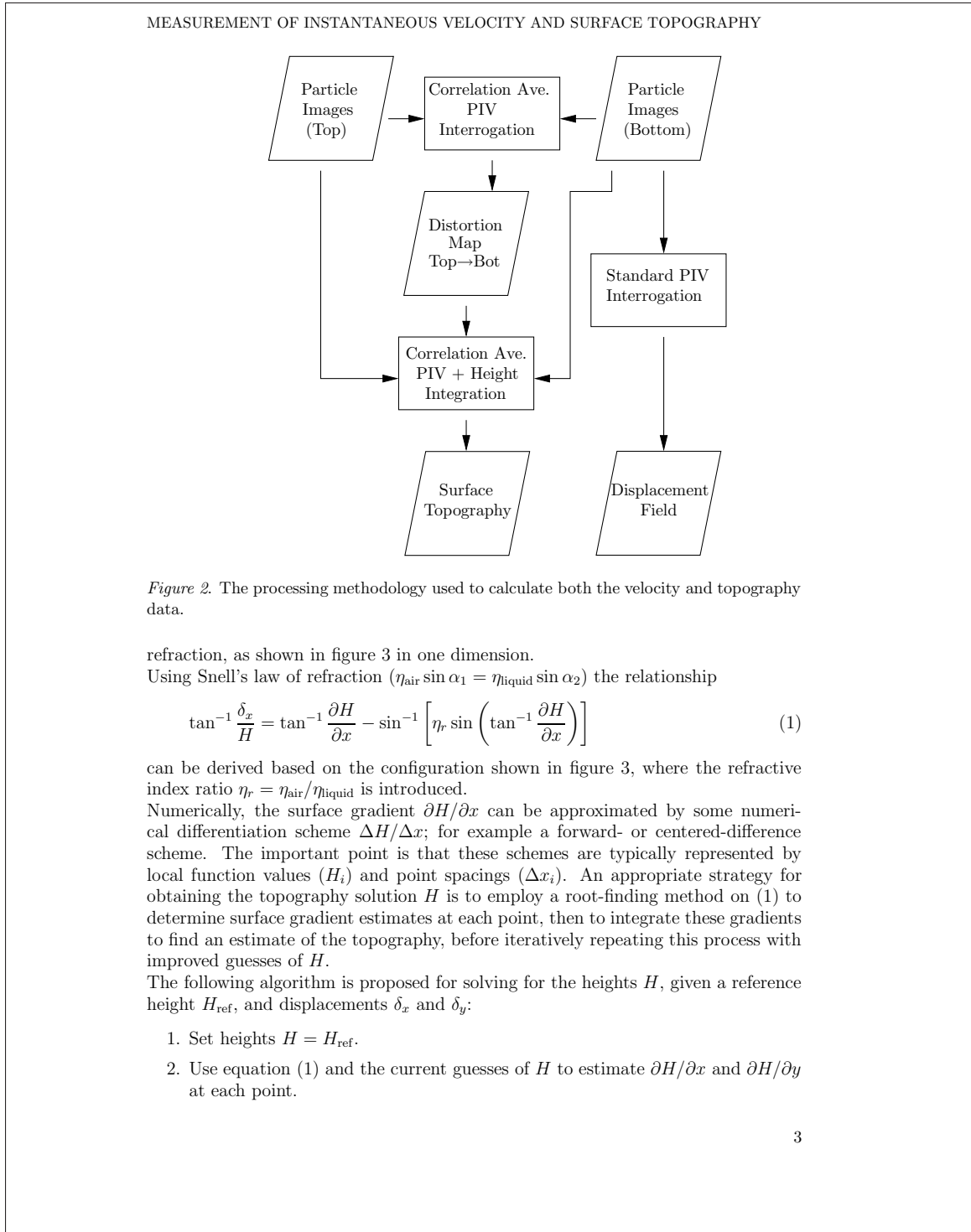
one below the glass bottom, as shown in Figure 1. These cameras are positioned to achieve approximately the same magnification and field of view. Under conditions of a flat water surface, the images from the top camera can be related to the images from the bottom camera by a mapping function which can be evaluated using techniques described by Fouras *et al.* [3, 5].

Figure 2 describes the process of analysing the data from the top and bottom cameras to yield the velocity and height data. The images acquired through the flat glass bottom can be interrogated to yield the velocity data using PIV analysis. When the images from the top and bottom are compared using PIV analysis (taking into account the mapping function evaluated under flat or still conditions), the resultant apparent displacement field must be the result of refraction of light through the distorted free surface. The displacement field is related to free surface gradients, which can be integrated to yield the free surface topography. An algorithm to perform this integration with minimal sensitivity to noise while maintaining fine detail is described in section 2.1.

2.1. Obtaining surface topography from PIV displacement data

The PIV analysis of the experimental images produces a grid of displacement vectors corresponding to the optical distortion laser light scattered by the seeding particles due to refraction through the surface of the liquid-air interface. At each point, the components of the displacement vector in Cartesian coordinates are (δ_x, δ_y). The goal of the numerical surface height integration is to obtain the height H at each point, given a reference height H_{ref}. In this paper, a robust technique for obtaining the surface topography in a manner devoid of any positional bias is proposed. It will later be shown that the least-squares integration approach filters random remaining errors from the PIV process, while reproducing fine details in the true free-surface topography.

At each location, the gradient of the surface is $\partial H/\partial \mathbf{x}$ where the spatial coordinate vector $\mathbf{x} = \langle x, y \rangle$. The surface gradient is related to H, δ_x and δ_y by the physics of
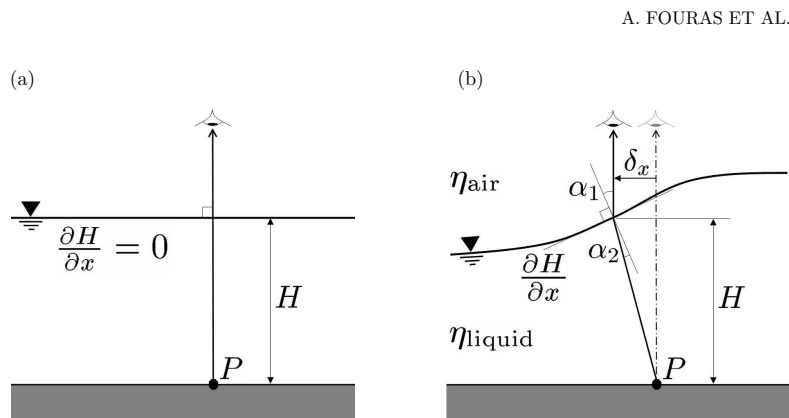
2

MEASUREMENT OF INSTANTANEOUS VELOCITY AND SURFACE TOPOGRAPHY

Figure 2. The processing methodology used to calculate both the velocity and topography data.

refraction, as shown in figure 3 in one dimension.

Using Snell's law of refraction ($\eta_{\text{air}} \sin \alpha_1 = \eta_{\text{liquid}} \sin \alpha_2$) the relationship

$$\tan^{-1} \frac{\delta_x}{H} = \tan^{-1} \frac{\partial H}{\partial x} - \sin^{-1} \left[\eta_r \sin \left(\tan^{-1} \frac{\partial H}{\partial x} \right) \right] \qquad (1)$$

can be derived based on the configuration shown in figure 3, where the refractive index ratio $\eta_r = \eta_{\text{air}}/\eta_{\text{liquid}}$ is introduced.

Numerically, the surface gradient $\partial H/\partial x$ can be approximated by some numerical differentiation scheme $\Delta H/\Delta x$; for example a forward- or centered-difference scheme. The important point is that these schemes are typically represented by local function values (H_i) and point spacings (Δx_i). An appropriate strategy for obtaining the topography solution H is to employ a root-finding method on (1) to determine surface gradient estimates at each point, then to integrate these gradients to find an estimate of the topography, before iteratively repeating this process with improved guesses of H.

The following algorithm is proposed for solving for the heights H, given a reference height H_{ref}, and displacements δ_x and δ_y:

1. Set heights $H = H_{\text{ref}}$.

2. Use equation (1) and the current guesses of H to estimate $\partial H/\partial x$ and $\partial H/\partial y$ at each point.

3

24

(a)   (b)

Figure 3. (a) The undistorted position of a point P (on the laser sheet, shaded grey) viewed from a distant location through an undisturbed free surface. (b) The apparent displacement δ_x of point P due to refraction through the surface at height H with gradient $\partial H/\partial x$. Refractive indices of the air (η_{air}) and liquid (η_{liquid}) phases are shown, as are the refraction angles α_1 and α_2.

3. Integrate gradients ($\partial H/\partial x$ and $\partial H/\partial y$) to find estimate of heights (H_{est}).

4. Shift H_{est} to minimize the error between measured refraction displacements, and those predicted by numerical ray tracing.

5. The adjusted heights H_{adjust} can be refined by repeating steps 2-4 until the difference between successive H_{adjust} values converges.

The following section describes in detail the procedure used to integrate the gradient data for the surface topography (step 3).

2.2.   INTEGRATION OF SURFACE GRADIENTS FOR SURFACE TOPOGRAPHY

At each point on the surface, gradients in x and y are known. If the total number of data points is N, then based on numerical estimates of the surface gradients, an over-prescribed matrix system

$$\mathbf{AH} = \mathbf{b},\qquad\qquad\qquad\qquad\qquad (2)$$

can be established where $\mathbf{A}$ is a $(2N+1)\times N$ matrix containing numerical derivative estimates in x and y for each point, plus a function of the reference height H_{ref} to maintain the consistency of the matrix, $\mathbf{H}$ is a solution vector of length N representing the surface heights, and $\mathbf{b}$ is a vector of length $2N+1$ containing the gradients obtained from the refraction physics and displacement data. Written in full, this

4

MEASUREMENT OF INSTANTANEOUS VELOCITY AND SURFACE TOPOGRAPHY

becomes

$$\mathbf{AH} = \left[\begin{array}{c} \mathbf{D_x} \\ \mathbf{D_y} \\ \mathbf{A}_{\mathrm{ref}} \end{array}\right] \left[\begin{array}{c} H_1 \\ \vdots \\ H_N \end{array}\right] = \mathbf{b} = \left[\begin{array}{c} \frac{\partial H}{\partial x}\big|_1 \\ \vdots \\ \frac{\partial H}{\partial x}\big|_N \\ \cdots\cdots \\ \frac{\partial H}{\partial y}\big|_1 \\ \vdots \\ \frac{\partial H}{\partial y}\big|_N \\ \cdots\cdots \\ b_{\mathrm{ref}} \end{array}\right]. \tag{3}$$

As $\mathbf{A}$ is not square, the solution for $\mathbf{H}$ cannot be obtained by direct inversion of $\mathbf{A}$. Instead, a solution is found in a least-squares sense by obtaining the pseudo-inverse of $\mathbf{A}$, i.e.,

$$\mathbf{H} = (\mathbf{A}^T\mathbf{A})^{-1}\mathbf{A}^T\mathbf{b} \tag{4}$$

For problems of a practical size, $\mathbf{A}$ quickly becomes too large to store in full. For example, when $N = 50 \times 50$, $\mathbf{A}$ becomes a 5001×2500 matrix. Fortunately, with an appropriate selection of derivative approximation technique $\mathbf{A}$ is very sparse. For instance, forward or centered difference approximations, produce only 2 non-zero elements per row, with the exception of the final row. The final row of $\mathbf{A}$ specifies an equation relating the unknown heights $\mathbf{H}$ to the reference height H_{ref}. An ideal equation would equate the mean height to the reference height

$$\sum_{i=1}^{N} H_i = NH_{\mathrm{ref}}, \tag{5}$$

but this generates a full row in $\mathbf{A}$, which then renders the matrix product $\mathbf{A}^T\mathbf{A}$ full. A high sparsity of $\mathbf{A}^T\mathbf{A}$ can be maintained if a simpler reference height relationship (e.g., $H_1 = H_{\mathrm{ref}}$) is adopted instead.

In the present implementation, $\mathbf{A}$ and $\mathbf{A}^T\mathbf{A}$ were constructed using the Compressed Sparse Row (CSR) sparse matrix storage format, with derivatives at the edges of the image estimated using forward- and backward-differences, and at interior points using centered-differences. The solution of the linear problem

$$\left(\mathbf{A}^T\mathbf{A}\right)\mathbf{H} = \mathbf{A}^T\mathbf{b} \tag{6}$$

was obtained using the PARDISO package [10]. The symmetry of $\mathbf{A}^T\mathbf{A}$ meant that only the upper-diagonal component needed to be stored, further reducing the strain on storage requirements.

In the present implementation of the surface topography integration technique, the assembly of $\mathbf{A}$, and the assembly and factorization of $\mathbf{A}^T\mathbf{A}$ were completed prior to entering the iterative loop, leaving only a sparse matrix-vector product operation ($\mathbf{A}^T\mathbf{b}$), and a sparse matrix solve to be completed during each iteration.
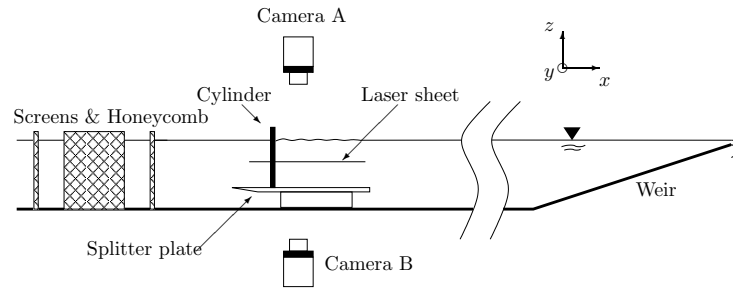
5

Figure 4. Schematic diagram showing the setup of the cylinder wake experiments on the water table. The combination of screen, honeycomb and screen was used to reduce free-stream turbulence levels. The splitter plate was used to reduce the size and effect of the bottom wall boundary layer on the two-dimensionality of the flow. Also shown are the cameras and axis co-ordinates.

3. Results

The experiments reported in this paper were performed on a water table shown schematically in Figure 4. The splitter plate was 25 mm above the table floor. The water height above the splitter plate was about $H_{\text{ref}} = 51$ mm and the cylinder had diameter $D = 3.9$ mm. At each Reynolds number, 200 frame pairs were acquired. The acquisition frame rate 5 Hz and the between pairs was equal to 20 ms. A Reynolds number is defined as $Re = UD/\nu$, where U is the velocity of the oncoming flow, D is the cylinder diameter, and ν the kinematic viscosity. A Strouhal number is defined as $St = fD/U$ where f is the frequency of shedding. For parallel shedding, previous studies (e.g., Williamson [12]) propose a linear relationship between the shedding frequency and the inverse square root of the Reynolds number. The vorticity is calculated by a combination of least-squares fitting of a second-order polynomial, and analytical differentiation, which has been shown to produce results that are insensitive to random errors in the PIV calculation [6]. Results for an experiment conducted at $Re = 76$ is shown in Fig. 5. The observed Strouhal number was 0.157±0.001, whereas the expected Strouhal number based on the relationship proposed by Williamson [12] is 0.152.

The Strouhal number discrepancy is most likely due to non-uniformities in the spanwise direction; either due to oblique shedding patterns (which are known to occur beyond $Re \approx 60$ for a circular cylinder [13]), or other irregularities resulting from the mismatched cylinder end-conditions. The vorticity contour plot in figure 5 bears a close resemblance to two-dimensional computations obtained at similar Reynolds numbers (such as Braza *et al.* [1], Green *et al.* [8] and independent computations performed by the authors), validating the PIV measurements.

The true power of this technique is demonstrated in Figure 6, which shows three-dimensional renderings of the reconstructed surface topography. The overlaid vor-

6

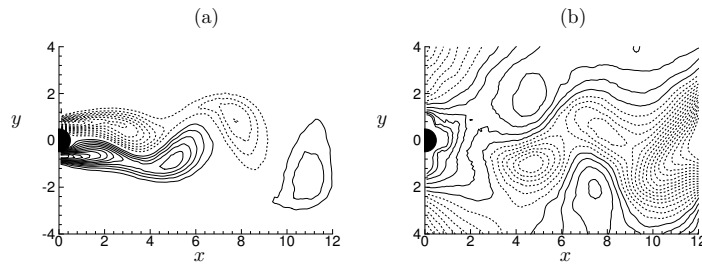MEASUREMENT OF INSTANTANEOUS VELOCITY AND SURFACE TOPOGRAPHY

Figure 5. Plots of (a) vorticity and (b) relative height taken at a Reynolds number $Re = 76$. Solid and dashed lines represent positive and negative values.
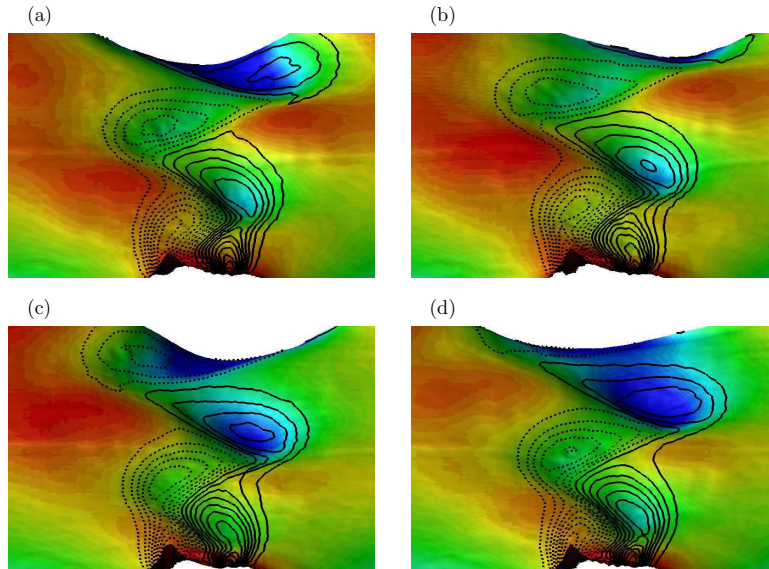

Figure 6. Three-dimensional iso-surface of calculated surface height overlaid with vorticity contours. Data are shown for Reynolds number $Re = 76$ for different phases, (a) $t = 0$; (b) $t = T/4$; (c) $t = T/2$; (d) $t = 3T/4$, where T is the shedding period. Solid and dashed lines represent positive and negative values of vorticity. The cylinder is located at the bottom of each frame, and flow is from bottom to top. Coloured contours denote surface height, with blue and red corresponding to low and high regions, respectively.

ticity contours highlight that a strong relationship exists between the measured velocity field (captured on the plane of the submerged laser sheet), and the deformation of the free surface. Hydrodynamic theory dictates that the deformation in

7

28

the surface height relates to the total pressure in the flow, though surface tension and other forces will also contribute to the final topography.

The data also elucidate the high sensitivity of the topography measurements. In the vicinity of the cylinder, the meniscus is clearly visible, with significantly greater relative height than variations measured in the wake. In practice, the meniscus is of the order 1 mm in height. When conducting the experiments, the surface deformation arising from the motion of the wake was invisible to the naked eye. Hence surface deformations an order of magnitude smaller than the scale of the cylinder have been resolved using this technique.

4.   Conclusions

A novel technique for the simultaneous measurement of free surface topography and velocity vector field has been developed. The flow behind a circular cylinder at low Reynolds numbers has been measured using this technique. Both the vorticity field and the Strouhal number closely match the expected results. The free surface topography, which can be related to the pressure field, exhibits an intimate relationship to the vorticity field. The nature of this relationship is the subject of further investigation.

Acknowledgments

References

[1] M. Braza, P. Chassaing, and H.H. Minh. Numerical study and physical analysis of the pressure and velocity fields in the near wake of a circular cylinder. *Journal of Fluid Mechanics*, 169:79–130, 1986.

[2] A. Buchanan, R. Macartney, M.C. Thompson, E. Brocher, and K. Hourigan. Hydraulic analogy study of supersonic rectangular jet screech control with cylinders. *Accepted for publication in AIAA Journal*, 2007.

[3] A. Fouras, J. Dusting, and K. Hourigan. A simple calibration technique for stereoscopic particle image velocimetry. *Experiments in Fluids (In Press)*, 2007.

[4] A. Fouras, K. Hourigan, M. Kawahashi, and H. Hirahawa. An improved free surface topographic technique. *Journal of Visualization*, 9:49–56, 2006.

[5] A. Fouras, D. Lo Jacono, and K. Hourigan. Target-free Stereo PIV: a novel technique with inherent error estimation and improved accuracy. *Under consideration for publication in Exp. Fluids*, 2007.

[6] A. Fouras and J. Soria. Accurate out-of-plane vorticity calculation from in-plane velocity vector field data. *Experiments in Fluids*, 25:409–430, 1998.

[7] H. Fu and D. Rockwell. Shallow flow past a cylinder: transition phenomena at low Reynolds number. *Journal of Fluid Mechanics*, 540:75–97, 2005.

[8] R.B. Green and J.H. Gerrard. Vorticity measurements in the near wake of a circular cylinder. *Journal of Fluid Mechanics*, 246:657–691, 1993.

[9] M. Raffel, C. E. Willert, and J. Kompenhans. *Particle Image Velocimetry: A Practical Guide*. Springer, Berlin, Germany, 1998.

8

MEASUREMENT OF INSTANTANEOUS VELOCITY AND SURFACE TOPOGRAPHY

[10] O. Schenk and K. Gartner. Solving unsymmetric sparse systems of linear equations with pardiso. *Future Generation Computer Systems 20*, 3:475–487, 2004.

[11] G. Tanaka, K. Okamoto, and H. Madarame. Experimental investigation on the interaction between a polymer solution jet and a free surface. *Experiments in Fluids*, 29:178–183, 2000.

[12] C. H. K. Williamson. Defining a universal and continous Strouhal-Reynolds number relationship for the laminar vortex shedding of a circular-cylinder. *Physics of Fluids*, 31(10):2742–2744, 1988.

[13] C. H. K. Williamson. Oblique and parallel modes of vortex shedding in the wake of a circular cylinder at low Reynolds numbers. *Journal of Fluid Mechanics*, 206:579–672, 1988.

[14] X. Zhang, D. Dabiri, and M. Gharib. A novel technique for surface elevation mapping. *Physics of Fluids*, 6:S11, 1994.

9

Chapter 3

Stereo PIV

3.1 Overview

This chapter discusses a series of advances in stereo PIV (SPIV). SPIV is clearly an important tool in modern fluid mechanics investigations and moderate improvements in these techniques can have a significant impact.

The chapter begins with a paper by Fouras et al (2007a), which is based on the application of the ground glass technique discussed in Chapter 2 and Fouras et al (2006), which addresses the problem of calibration in SPIV. The calibration of SPIV is a significant contributor to the total time (and hence expense) of performing SPIV measurements and the total error of those measurements. The paper also demonstrates a detailed error analysis of SPIV as a function of the errors of the constituent planar PIV processes and the stereo (geometrical) configuration of the cameras. This detailed analysis allows the practitioner to optimise the geometrical configuration for a reduction in errors.

The chapter continues with a paper by Fouras et al (2007c) which outlines the development of a SPIV technique utilising three cameras. This paper, which builds heavily on the previous paper, describes how the use of three cameras (with one in the paraxial position - normal to the light sheet) allows the practitioner to dispense with a separate calibration phase. The availability of data from a third perspective increases the robustness of the technique. Finally the paper describes how the technique substantially reduces SPIV errors and allows for inherent estimation of those errors. As with the previous paper, this paper also demonstrates a detailed error analysis of this improved methodology as a function of the errors of the constituent planar PIV processes and the geometrical configuration of the cameras.

3.2   A Simple Calibration Technique
for Stereoscopic Particle Image Velocimetry

The following paper was published in 2007 in *Experiments in Fluids*. This work was co-authored by J. Dusting and K. Hourigan, and is entitled *"A Simple Calibration Technique for Stereoscopic Particle Image Velocimetry"*. The paper is reproduced in this thesis directly from the version published online.
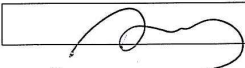
Declaration

Declaration for manuscript included in PhD thesis

Monash University

Declaration for Thesis Chapter 3.2

Declaration by candidate

In the case of Chapter 3.2, the nature and extent of my contribution to the work was the following:

Nature of contribution	Extent of contribution (%)
Conceived initial ideas, initiated the paper, performed experiments, wrote analysis software, analysed data, wrote manuscript, revised manuscript.	60

The following co-authors contributed to the work. Co-authors who are students at Monash University must also indicate the extent of their contribution in percentage terms:

Name	Nature of contribution	Extent of contribution (%) for student co-authors only
Dr. J. Dusting	Performed experiments, analysed data, co-wrote manuscript	N.A.
Professor K. Hourigan	Co-wrote manuscript	N.A.

Candidate's Signature		Date 08 Nov 07

Declaration by co-authors

The undersigned hereby certify that:

(13)   the above declaration correctly reflects the nature and extent of the candidate's contribution to this work, and the nature of the contribution of each of the co-authors.
(14)   they meet the criteria for authorship in that they have participated in the conception, execution, or interpretation, of at least that part of the publication in their field of expertise;
(15)   they take public responsibility for their part of the publication, except for the responsible author who accepts overall responsibility for the publication;
(16)   there are no other authors of the publication according to these criteria;
(17)   potential conflicts of interest have been disclosed to (a) granting bodies, (b) the editor or publisher of journals or other publications, and (c) the head of the responsible academic unit; and
(18)   the original data are stored at the following location(s) and will be held for at least five years from the date indicated below:

Location(s)	Division of Biological Engineering, Monash University.
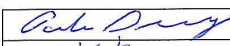
Signature 1		Date
Signature 2		

RESEARCH ARTICLE

A simple calibration technique for stereoscopic particle image velocimetry

**Andreas Fouras · Jonathan Dusting ·
Kerry Hourigan**

Abstract A novel Stereo PIV technique, with improvements over other techniques, is presented. The key feature of the new technique is the direct measurement of calibration data at each point in space on the measurement grid, so that no interpolation is necessary. This is achieved through the use of a contiguous target which can be analysed using standard PIV processing software. The technique results in three-dimensional measurements of high accuracy with a significantly simpler calibration phase. This has the benefit of improving ease of use and reducing the time taken to obtain data. Thorough error analysis shows that while previously-described error trends are correct, additional facets of the technique can be optimised to allow highly accurate results. The new technique is rigorously validated here using pure translation and rotation test cases. Finally, the technique is used to measure a complex swirling flow within a cylindrical vessel.

1 Introduction

Stereo particle image velocimetry (SPIV) is now a well-established extension of traditional particle image velocimetry (PIV) (Arroyo and Greated 1991; Willert 1997; Prasad 2000). SPIV offers several advantages over standard or planar PIV in cases where measured flow fields are three-dimensional. These advantages include the improved

A. Fouras (✉) · J. Dusting · K. Hourigan
Fluids Laboratory for Aeronautical and Industrial Research
(FLAIR) Department of Mechanical Engineering,
Monash University, P.O. Box 31, Clayton 3800, Australia
e-mail: fouras@eng.monash.edu.au

accuracy of in-plane components of the velocity field due to removal of perspective error and the resolution of the out-of-plane components themselves. Recent extensions of SPIV include three-dimensional high speed scanning (Hori and Sakakibara 2004), dual-time SPIV for acceleration measurement (Perret et al. 2006), multi-plane SPIV (Schroder and Kompenhans 2004), and stereoscopic micro-PIV (Lindken 2006).

SPIV involves the reconstruction of a three-component velocity field in a two-dimensional plane using two velocity fields derived using PIV. This reconstruction process relies on both simple geometrical equations utilising basic information about the camera setup, and a complicated calibration step to relate information acquired on the image plane to events occurring in the object plane. The techniques, by which the inevitable distortion of the measurement field is taken into account and the two two-dimensional vector fields are reconstructed into a single three-dimensional vector field, can be categorised as two-dimensional calibration-based reconstruction, three-dimensional calibration-based reconstruction and geometric reconstruction (Prasad 2000).

Geometric reconstruction mathematically relates the parameters of image acquisition and the measured two-dimensional velocity fields through ray tracing to the derived three-dimensional vector field (Prasad and Adrian 1993). It has been argued that as parameters become more complex, the process of geometric reconstruction becomes exponentially more difficult.

Two-dimensional calibration is similar to geometric reconstruction in that it uses information relating to imaging parameters to perform the reconstruction. It differs in that the distortion field is derived from the calibration process, rather than calculating distortion directly from the imaging parameters. In this way, the correction for

⚛ Springer

33

distortion and the reconstruction are separated into two distinct processes.

Three-dimensional calibration based techniques, such as those described by Soloff et al. (1997), are more commonly used than two-dimensional calibration. The main advantage of three-dimensional calibration is that no information regarding the geometric parameters of the stereoscopic image acquisition are required. Instead, a direct mapping function is derived between an object in three-dimensional space and its corresponding location in the image planes. The three-dimensional methods are similar to two-dimensional calibration techniques in that the distortion is corrected for by a calibration in the imaging plane. The difference lies in that they also involve calibration from the object plane to a number of parallel planes near the imaging plane. This additional information frees the technique from the requirement of information relating to the imaging geometry as this information is inferred in the additional calibrations (Prasad 2000; Prasad and Adrian 1993; Raffel et al. 1998; Soloff et al. 1997).

An interesting idea, central to the theme of this paper, was developed in Willert (1997) and further in Wieneke (2005). This idea is to utilise the cross correlation of the particle images to generate additional information regarding the relative camera positions and image deformations. This has the advantage of correcting for the errors caused by misalignment of the calibration target and the laser sheet. The disadvantages of this approach include further complication of the technique. Furthermore, any differences in image distortions caused by different camera positions will result in degradation of correlation between images. Wieneke (2005) tackle this problem by de-warping the images prior to this step, but this adds further complexity and computational effort.

Almost all two-dimensional and three-dimensional calibration techniques utilise a calibration target, which consists of a discrete number of markers displaced on a regular Cartesian grid (Lawson and Wu 1997b). Typically these targets contain in the order of 100 such markers, i.e. approximately a 10×10 grid. The authors believe that it is this limited approach that has largely dictated much of the development of these techniques. The images of the target are compared to the known positional layout of the target and the relative positions of all markers on the calibration target. The exact method of this varies depending on the PIV software being utilised but is largely based on the PIV algorithms themselves. For some software this even requires the practitioner to manually identify markers in an image and link them to a corresponding marker on the target. The uncertainty in identifying the position of these markers by use of PIV software is proportional to the size of these markers. The calibration data are then fitted by a

method such as least squares fitting, (both linear and non-linear are used), to obtain general data applicable to the entire measurement region. The dependency of calibration techniques on precise knowledge of the target geometry introduces measurement error and further complicates the SPIV procedure.

2 New technique

The new calibration technique described in this paper is based on the same principles as previous two-dimensional calibration techniques but differs considerably in implementation. The main improvement offered by the new technique is that interpolation is not necessary at any stage of the calibration and reconstruction process. In other words, the calibration is performed on a 1:1 basis: each resultant three-dimensional vector is calculated in object space. Each pair of two-dimensional vectors is similarly interrogated from a region in object space that is determined by a process similar to calibration. Lawson and Wu (1997b) also used a contiguous target to obtain information for calibration purposes, but did not use their cross correlated results to directly obtain calibration vectors at each PIV window location.

A schematic diagram of the configuration and co-ordinate system used in this paper is shown in Fig. 1. A flow chart of the entire procedure is shown in Fig. 2. Unlike most two-dimensional calibration techniques, much of the analysis is completed using standard PIV interrogation, and the final reconstruction is a relatively simple process.

A significant difference in methodology between the new technique and other two-dimensional calibration techniques is that a contiguous calibration target is utilised rather than a regular grid. Instead of comparing the target images with a priori knowledge, the target image is digitally compared with a second image acquired through paraxial imaging. This combination of a contiguous target and a reference paraxial calibration target image allows calibration data to be measured by any PIV interrogation software.

One example of a contiguous calibration target that can be successfully used for this technique is a sandblasted glass plate. The distortion of the random surface pattern produced by sandblasting is better correlated by typical PIV analysis software than a regular pattern. Indeed, sandblasted surface patterns have been used successfully in other distortion measurement imaging techniques involving cross correlation (Fouras et al. 2006). In that case, it was shown that sandblasted glass gave a remarkably high level of information, allowing very high resolution correlation measurements. Ideally, the reference plate is positioned in
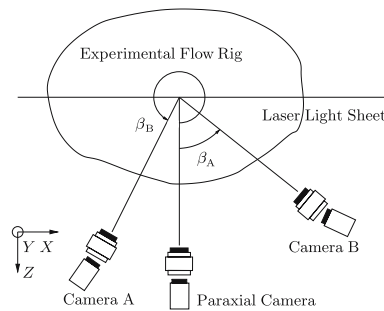
Fig. 1 Schematic diagram of generic stereo PIV configuration including the co-ordinate systems used in this paper. Shown on the figure are the X, Y and Z axes. The origin of the coordinate system is the point on the laser sheet plane center in the center of the imaged region of interest. Here an example of two cameras, denoted left (L) and right (R) for simplicity are shown. Also shown is the Scheimpflug configuration and the definition of the camera angles β_L, β_R and camera positions X_L, Z_L and X_R, Z_r. Also shown is the paraxial camera in its fixed position with $\beta = 0$
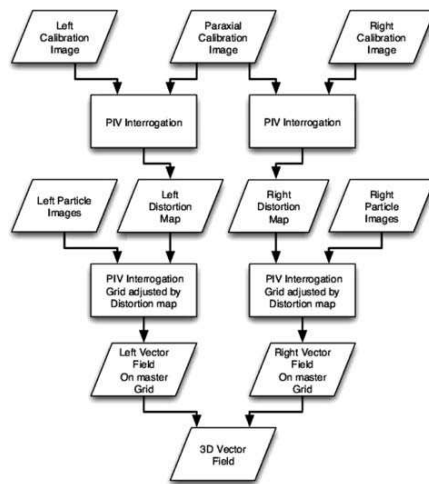
Fig. 2 Description of the new technique to yield three-dimensional vector fields using the analysis of target and flow images. Rhomboids represent input or output and rectangles represent processes. The five sets of input images are included. Also shown is the direct process resulting from the 1:1 mapping achieved by interrogating a contiguous target

the camera field of view so that the test pattern aligns in such a way as to represent an artificial laser-illuminated particle field, i.e. at the same angle to the camera lens as

the measurement plane. Back-illumination of the plate using diffuse white light sources positioned in line with the CCD cameras helps optimise the contrast in the images, and thus improves the PIV signal to noise ratio.

If the field of view in the horizontal (X) direction is the same for the angularly displaced camera images as it is for the paraxial image, then the field of view in the vertical (Y) direction will be larger in the paraxial image. Therefore, the paraxial image must be digitally stretched in the Y direction by a factor of 1/sin (β), where β is the camera displacement angle. Alternatively, the two angled camera images may be shrunk in the Y direction. Bi-cubic interpolation is an appropriate method for stretching or shrinking these images. It is then necessary but straightforward to crop the paraxial image in the Y direction so that the images are of the same size. When superimposed onto one another, the images of the reference plate from the angled perspective and the stretched paraxial perspective appear similar to Fig. 3. In the combined image, the magnification heterogeneity across the field of view is clearly visible, as is the point where the magnifications of the two images are matched.

By selecting the paraxial calibration target image as the first image in the interrogation process, by ensuring that only sampling windows in the displaced images are shifted during any offset interrogation processes, and by performing the PIV interrogation process with exactly the same input parameters (e.g. sampling window offset, overlap, etc.), the resulting vector fields are in fact 1:1 vector maps of the distortion caused by the angular offset.

For example, the image pair shown in Fig. 3 can be used to derive a left-to-paraxial calibration field such as that
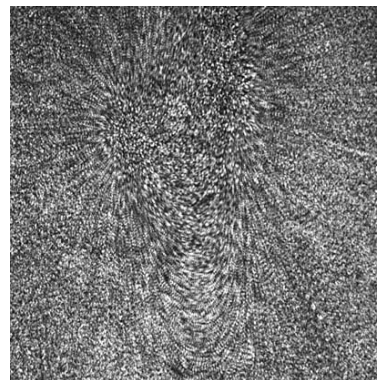

Fig. 3 Superimposed stretched paraxial and left camera images of a sandblasted glass plate reference pattern

shown in two-dimensional vector form in Fig. 4a. The vectors quantify the degree to which each regularly-spaced interrogation window on the paraxial image is distorted in the left image because of the angular offset. The shaded bands represent the distortion in the Y component. Solid contour lines denote regions of positive Y distortion while dashed contour lines denote regions of negative Y distortion. The edges of Fig. 4a have the greatest magnitude of distortion, which is representative of the fact that the greatest magnification difference between the angularly displaced and paraxial images occurs in these regions. The edge of the image plane nearest to the angularly displaced camera is on the left hand side, where the vectors point away from the center. Similarly, the vectors on the right hand side of Fig. 4a point toward the center of the image, as the right edge of the image plane is the furthest from the camera. It is worth noting that an additional stretching of the X component occurs across the entire field of view as the process takes into account any mismatch between the paraxial and displaced camera fields of view.

A right-to-paraxial calibration vector field, corresponding to the same example, is presented in Fig. 4b. In this case, the near edge of the field of view is on the right hand side of the right camera image, and the far edge is on the left hand side. Theoretically, the expectation is that this calibration field should resemble a Y-axis reflection of the left-to-paraxial calibration field. While this is approximately the case, in reality there are subtle differences between the two fields caused by slight discrepancies in camera positioning and magnification. Herein lies a demonstration of one of the advantages of the improved calibration technique; that is, by measuring the distortions directly, the positional and magnification imprecision associated with the angularly displaced cameras is compensated for automatically.

When the PIV interrogation is performed to determine the two two-dimensional vector flow fields, the base position of each flow vector is offset by the corresponding vector at the same location on the calibration vector field. This results in all measurements being performed on the same grid in real space. Moreover, an added benefit is obtained whereby the distortion field can be differentiated to yield local magnification data, allowing velocity vectors to be corrected to this additional error of perspective. This differentiation can be performed to high accuracy using any advanced numerical differentiation technique, such as that described by Fouras and Soria (1998). This leaves just the straightforward, well-documented step of reconstructing the three-component vectors from matching pairs of two-component vectors measured at that same location (Lawson and Wu 1997a).

3 Error analysis

The equations for geometric reconstruction are simply derived using similar triangles or parametric equations. For the current analysis, we define the two cameras as camera A and B, with position co-ordinates (X_a, Y_a, Z_a) and (X_b, Y_b, Z_b), respectively. As the two cameras are typically positioned on the horizontal plane, Y_a and Y_b are assumed to be zero. The projected displacement vectors on camera A and B are also needed to derive the stereoscopic velocity field. We define these as $\hat{x}_a, \hat{y}_a$ and $\hat{x}_b, \hat{y}_b$, respectively.

The solution to the equations is defined as the reconstructed vector $\mathbf{R}$ with components $\Delta x, \Delta y$, and Δz. The solution for Δy is over-constrained and can be acquired just as easily in two different ways. Usually the average of the two solutions is used. The solutions for Δx and Δz are much more interesting than Δy and discussion here is limited to these components:

$$\Delta x = ((\hat{x}_a - X_a)\hat{x}_b Z_b + (\hat{x}_b - X_b)\hat{x}_a Z_a)/D_1,$$
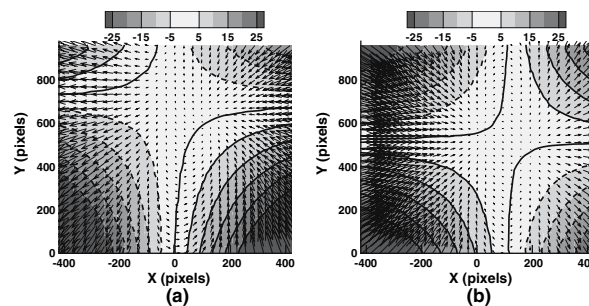$$\Delta z = (\hat{x}_a - \hat{x}_b)Z_a Z_b/D_1, \tag{1}$$

where

Fig. 4 Left-to-paraxial (**a**) and right-to-paraxial (**b**) distortion calibration field in two-dimensional vector form for $\beta = 45°$. The contour levels represent vertical (Y) distortion

$$D_1 = (\hat{x}_a - X_a)Z_b + (\hat{x}_b - X_b)Z_a.$$

To calculate sensitivity of $\mathbf{R}$ to errors in the underlying PIV, we calculate $\mathbf{R}'(\hat{x}'_a, \hat{x}'_b)$ by substituting the following expressions into Eq. 1:

$$\begin{aligned} \hat{x}'_a &= \hat{x}_a + \varepsilon_{\hat{x}a}, \\ \hat{x}'_b &= \hat{x}_b + \varepsilon_{\hat{x}b}, \end{aligned} \qquad (2)$$

where $\varepsilon_{\hat{x}a}$ and $\varepsilon_{\hat{x}b}$ represent the errors in measuring the projected displacement vector.

We can then define ε as $\mathbf{R}' - \mathbf{R}$ or

$$\begin{aligned} \varepsilon_x &= R'_x - R_x, \\ \varepsilon_z &= R'_z - R_z. \end{aligned} \qquad (3)$$

To then simplify Eq. 3, we make the assumption that $X_a, X_b, Z_a, Z_b, \hat{x}_a, \hat{x}_b >> \varepsilon_{\hat{x}a}, \varepsilon_{\hat{x}b}$. Using this assumption, we expand terms in Eq. 3 and then remove terms of least significance. This produces the equations:

$$\begin{aligned} \varepsilon_x &= (\varepsilon_{\hat{x}a} X_b Z_a - \varepsilon_{\hat{x}b} X_a Z_b)/D_4, \\ \varepsilon_z &= ((\varepsilon_{\hat{x}b} - \varepsilon_{\hat{x}a}) Z_a Z_b)/D_4, \end{aligned} \qquad (4)$$

where

$$D_4 = (X_b Z_a - X_a Z_b).$$

We define σ_x, σ_z, σ_a, σ_b to be the standard deviations of the random variables $\varepsilon_x, \varepsilon_z, \varepsilon_{\hat{x}a}, \varepsilon_{\hat{x}b}$.

Of use is the variable σ_{PIV} which is used to represent the expected uncertainty in the PIV processing, taking into account all the conditions and qualities of the PIV process, but with a paraxial perspective. For consistency with previous work we also define σ_p, which is almost identical to σ_{PIV} but is related to the direct processing error not normalised for stereo angle β.

$$\begin{aligned} \sigma_{pa} &= \sigma_{\text{PIV}}/\cos(\beta_a), \\ \sigma_{pb} &= \sigma_{\text{PIV}}/\cos(\beta_b). \end{aligned} \qquad (5)$$

Using the definition of the standard deviation, assuming that $\varepsilon_{\hat{x}a}, \varepsilon_{\hat{x}b}$ are independent random variables with standard deviation σ_{pa}, σ_{pb}, and converting to polar co-ordinates for convenience, we have:

$$\begin{aligned} \sigma_x &= \sigma_{\text{PIV}}\sqrt{(\sin^2(\beta_a) + \sin^2(\beta_b))/\sin^2(\beta_b - \beta_a)}, \\ \sigma_z &= \sigma_{\text{PIV}}\sqrt{(\cos^2(\beta_a) + \cos^2(\beta_b))/\sin^2(\beta_b - \beta_a)}. \end{aligned} \qquad (6)$$

It is interesting to note that the radius terms from the polar equations cancel, leaving the expression only in terms of β_a, β_b. These general equations are easily solved for any

geometry and allow us to solve for optimisation of errors. In Figs. 5 and 6, we present this information over the entire circle about the measurement volume.

For Fig. 5, there are a few interesting observations. First, the minimum error, relative to paraxial camera PIV error, is $1/\sqrt{2}$. Furthermore, it is clearly preferable to use a symmetric geometry with a small stereo angle to minimise this relative error in the reconstructed Δx component.
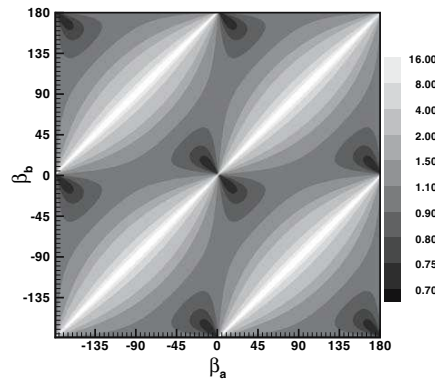

Fig. 5 Error in reconstructed Δx (lateral) displacements expressed relative to the expected PIV for a paraxial camera measuring a 2D flow as a function of camera angles β_a and β_b measured in degrees
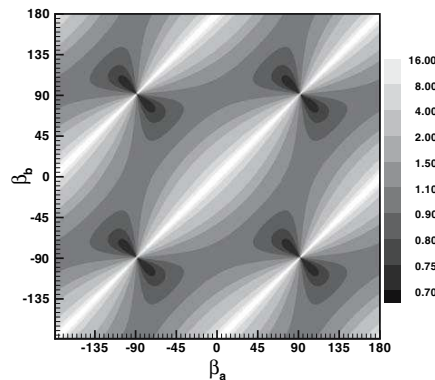

Fig. 6 Error in reconstructed Δz (out-of-plane) displacements expressed relative to the expected PIV for a paraxial camera measuring a 2D flow as a function of camera angles β_a and β_b measured in degrees

In Fig. 6, we see a pattern of sensitivity for the Δz component similar to, albeit asymmetrically out of phase with, the Δx sensitivity. We see the same minimum sensitivity level; it occurs with a symmetric camera geometry but at camera offset angles approaching 90°, which is not unexpected.

Figure 7 shows the combined sensitivity of both Δx and Δz components of the reconstructed vector. This combination is simply calculated as half of the sum of the two components. Two key points can be derived from this figure. First, it can be seen that the minimum of the average is not in fact $1/\sqrt{2}$, but 1.0. While the reconstruction allows increased accuracy due to an averaging process, the regions of high accuracy are out of phase and thus are suppressed in the averaged plot. Second, we see that the measurements least sensitive to error can theoretically be achieved at any mean stereo angle, as long as the two cameras are positioned orthogonal to one another. This expands on the previously reported finding by Lawson and Wu (1997a), that the best relative sensitivity for a symmetric configuration occurs when $\beta = \pm45°$. It should be remembered, however, that when β is close to $\pm90°$, the measurements would most likely suffer from additional higher order errors and in any case at such oblique measurement angles, other practical issues will make measurements difficult.

Since most practitioners use symmetric camera geometries, it is appropriate to force these conditions on the above equations. The conditions of symmetry are:

Fig. 7 Average of both the X and Z errors in reconstructed X displacements expressed relative to the expected PIV for a paraxial camera measuring a 2D flow. Note that the minimum value is 1.0, and lies on the line of $\beta_a - \beta_b = 90°$

$$\begin{aligned}
\sigma_p &= \sigma_{pa} = \sigma_{pb},\\
X_c &= X_a = -X_b,\\
Z_c &= Z_a = Z_b.
\end{aligned} \tag{7}$$

This time we define σ_p as the PIV error relative to an angularly displaced camera rather than to a paraxial camera. This produces the familiar result found in Prasad and Adrian (1993) and Zang and Prasad (1997) of:

$$\begin{aligned}
\sigma_x &= \sigma_{\text{PIV}}/\left(\sqrt{2}\cos(\beta)\right) = \sigma_p/\sqrt{2},\\
\sigma_z &= \sigma_{\text{PIV}}/\left(\sqrt{2}\sin(\beta)\right) = \sigma_p/\left(\sqrt{2}\tan(\beta)\right).
\end{aligned} \tag{8}$$

We can use a similar approach to determine the sensitivity of the new technique to the practitioner's ability to accurately measure the positions of the cameras relative to the measurement volume. This is particularly important as a means of validating the new technique, as unlike the technique of Soloff et al. (1997), the use of geometric reconstruction depends on the measurements of camera position. The sensitivity test can be undertaken by analysing the error in the reconstruction error caused by errors in X_a, X_b, Z_a and Z_B. Solving for the equivalent of Eq. 4 yields:

$$\begin{aligned}
\varepsilon_x = &((\varepsilon_{xa}X_b + \varepsilon_{xb}X_a)Z_aZ_b\\
&- (\varepsilon_{za}Z_b + \varepsilon_{zb}Z_a)X_aX_b)/D_9,\\
\varepsilon_z = &(\varepsilon_{xa}Z_aZ_b^2 - \varepsilon_{xb}Z_bZ_a^2\\
&- \varepsilon_{za}X_aZ_b^2 - \varepsilon_{zb}X_bZ_a^2)/D_9,
\end{aligned} \tag{9}$$

where

$$D_9 = (X_a^2Z_b^2 - 2X_aX_bZ_aZ_b + X_b^2Z_a^2)/(\hat{x}_a - \hat{x}_b).$$

These equations can be expressed in various ways to help the practitioner establish the sensitivity of the resolved stereo vector field to the accuracy of the measurements of camera positions, as a function of those camera positions. They could also be further expressed in statistical terms and for any geometry. Once again they are expressed here only for the symmetric case with the same assumptions for symmetry as in Eq. 7. We further assume that positional errors for X_a, X_b, Z_a and Z_b are equally represented by σ_m.

$$\sigma_x = \sigma_z = \sigma_m\sqrt{X_c^2 + Z_c^2}(\hat{x}_a - \hat{x}_b)/(2\sqrt{2}X_cZ_c). \tag{10}$$

This solution is based on the assumption that ε_{xa}, ε_{xb}, ε_{za} and ε_{zb} are independent random variables. However, this is rarely the case. Most practitioners mount both stereo cameras on some form of support structure. Let us now consider the particular case whereby the structure used
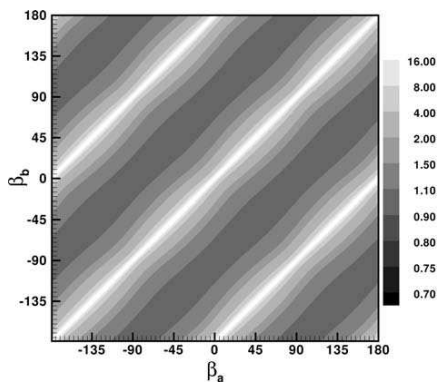
constrains the cameras so that they must lie on the pro-jected stereo angle. This means that the positional error would be sensitive to the distance from the measurement volume R and not β.

Now we use polar co-ordinates, along with symmetry conditions on the errors as well as the camera co-ordinates. This produces the straightforward but interesting result of:

$$\sigma_x = \sigma_z = 0. \tag{11}$$

This result is highly significant in that it implies that, to first order accuracy, the measurement accuracy of positions is of secondary importance, so long as the mechanism for holding the cameras in place constrains the cameras to lie on the angle β.

4 Translation test

The performance of the improved two-dimensional cali-bration technique was tested on a precision optical table (Melles-Griot, UK). Two Pixelfly CCD cameras (PCO, Germany) of $1,360 \times 1,024$ pixels resolution were installed on the table in an angular displacement configuration which included individual Scheimpflug devices. This popular camera configuration has been described previously (Zang and Prasad 1997; Prasad 2000). Separate experiments were undertaken to test the ability of the new system to measure object translation and rotation. The various test cases are listed in Table 1.

The translation experiments were carried out using two different camera displacement angles (β), as SPIV system performance often varies with β (Lawson and Wu 1997b). Camera angles of $\beta = 45°$ (Case A) and $\beta = 30°$ (Case B) were chosen, as these represent typical offsets that produce significant image distortion.

The test configuration for the translation experiments is illustrated schematically in Fig. 8. For these cases, the flow field was simulated by a sheet of paper printed with a pseudo-random pattern. This paper was held stationary between glass plates and affixed to a linear traverse con-structed with a 1 mm lead screw (THK, Japan) and an 18:1 geared stepper motor (Oriental Motor, Japan). Alignment
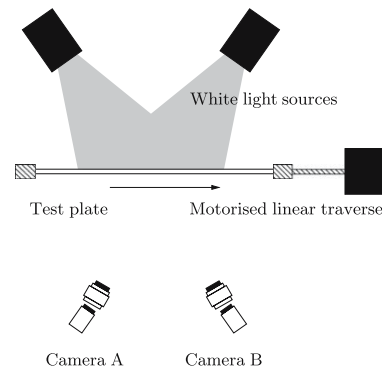

Fig. 8 Test configuration for the translation cases. Configuration is based on a test plate mounted on a PC controlled linear traverse illuminated by twin white light sources. Also shown are symmetric CCD cameras in the standard Scheimpflug configuration

of the traverse at an angle β to the cameras was maintained by screwing all apparatus to the optical table. The object was positioned for each image using a micro-stepping, stepper motor controller (National Instruments, USA).

Images were recorded at 101 positions with a small known displacement between each image. This allowed a flexible system of analysis. By integrating against different pairs, different length vectors were achieved. Frame 1 was compared with frame 2 and frame 2 with 3 and so on for a data set with displacement δx. Frame 1 was compared to frame 3 and 2 with 4 for a data set with displacement $2 \delta x$. In this manner, the complete data set was used to develop 16 reliable data sets of increasing magnitude. Since image quality and other PIV acquisition and processing parame-ters were held constant, PIV errors were also held constant in absolute terms. By normalising each data set by the known displacement, 16 nearly identical data sets, with varying levels of PIV accuracy, were achieved.

After resolving the two displacement vector fields onto the object plane using the calibration fields shown in Fig. 4a, b, and then applying the basic three-dimensional reconstruction equations, the resultant vector field ap-peared, as expected, to have a consistent horizontal (Δx) component and zero vertical (Δy) or out-of-plane (Δz) component. Figure 9 represents probability density func-tions of the difference, ε, between the expected displace-ment and the measured displacement, for Case A and Case B, respectively. ε was found to vary between each vector component, as well as between Cases A and B. For Case A, with a displacement of $15\delta x$, the standard deviation of the error, σ_R, in the resolved Δx component was 1.33×10^{-3} compared to a signal of unit value, whereas the standard

Table 1 List of test cases used for the validation of calibration technique

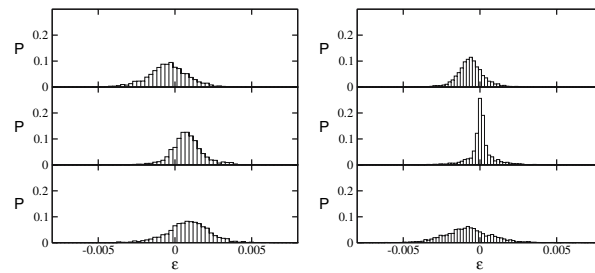| Case	Motion	Displacement	β (°)
A	Translation	$\delta x - 16\delta x$	45
B	Translation	$\delta x - 16\delta x$	30
C	Rotation	1.0°	45
D	Rotation	0.5°	45

Fig. 9 Probability density function of error ε in the measured displacement components, for (*left*) the $\beta = 45°$ translation case (Case A) and (*right*) for the $\beta = 30°$, translation case (Case B). The top plot shows the Δx component, the middle plot shows the Δy component and the lower plot shows the Δz component. The displacement between frames was equal to $15\delta x$ (≈ 33.95 px). The figure demonstrates the relative magnitudes of reconstructed displacement errors and their Gaussian nature

deviations in the remaining components, Δy and Δz, were 1.11×10^{-3} and 1.40×10^{-3}, respectively. For Case B, with the same displacement, σ_R was 1.15×10^{-3} for the Δx component, 0.87×10^{-3} for Δy, and 1.88×10^{-3} for Δz. The lower σ_R values corresponding to the Δx and Δy components in Case B may be attributable to the lower optical errors occurring when $\beta = 30°$ than when $\beta = 45°$ (Lawson and Wu 1997b). The larger discrepancy between Δx and Δz when $\beta = 30°$ than when $\beta = 45°$ is also consistent with the results of Eq. 8 and previously published error analyses (Lawson and Wu 1997b; Prasad 2000).

Overall, the histograms of error presented in Fig. 9 demonstrate the success of the technique in measuring linear translation. The error values are relatively small compared to the signal, which has been normalised so that δx is equal to one. Furthermore, the error distribution is unskewed. Any deviation from zero of the median ε value in the Δy or Δz components appears to be due to very minor movements of the displaced paper target in the vertical or out-of-plane directions. Similarly, any deviation of the median ε value from zero of the median ε value in the Δx component may be attributable to imprecision in the mechanical translation system.

As described above, the methodology undertaken to test the SPIV technique for translation cases allowed the level of PIV accuracy to be controlled. By varying the displacement of the target between images, 16 different values of σ_p, the standard deviation of the PIV processing error, were achievable. This facilitated a comparison between the standard deviation of the reconstructed stereo error σ_R, and σ_p. In this way it was possible to verify the performance of the system on the basis of the theoretical prediction of the ratio of σ_R on σ_p (see Eq. 8).

The symbols in Fig. 10 illustrates the measured relationship between σ_R and σ_p for cases A and B, respectively. The lines in each figure represent Eq. 8. For Case A, the

lines corresponding to the σ_x component and the σ_z component are co-linear, as tan (β) in Eq. 8 reduces to 1. For both β, the data show good agreement with the predicted results in both components.

5 Rotation test

Test Cases C and D were undertaken under pure rotational conditions, with the displacement occurring in the Z direction. As with the translation test, the first stage of the procedure involved capturing paraxial and angled perspective images of a sandblasted glass plate aligned with the image plane, in order to derive the 1:1 calibration offset vector map.

The second stage of the test procedure involved placing a sandblasted glass test block on a turntable mechanism so that the front surface was aligned with the image plane. From this position, designated as 0°, the turntable was rotated in the counter-clockwise direction to a position of 0.50°, measured using a dial gauge to an accuracy of ±0.03°. An image was recorded on each CCD camera, and then the turntable was rotated in the clockwise direction to a position of –0.5°, where another set of images was recorded. This procedure ensured that the theoretical Δx and Δy values were 0 when comparing the stereoscopic displacement fields between the two positions. The rotation angle of $\theta = 1.0°$ in Case C provided an opportunity to test the SPIV reconstruction system under conditions involving large displacements, large displacement variations, and a large out-of-plane to in-plane displacement ratio. The procedure also involved a movement of the recorded plane off the focused object plane, thus testing the sensitivity of the two-dimensional calibration technique to slight out-of-focus effects. The test was repeated for Case D with a rotation angle $\theta = 0.5°$. The test
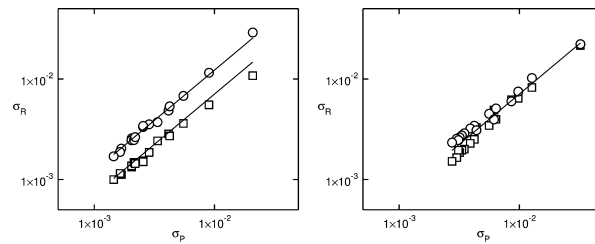
Fig. 10 Reconstructed vector field standard deviation (σ_R) as a function of PIV processing error (σ_p), for (*left*) the $\beta = 30°$, translation case (Case A) and (*right*) the $\beta = 45°$, translation case

(Case B). *open circle* symbols denote the standard deviation of Δz (σ_z) while *open square* symbols indicate the standard deviation of Δx (σ_x). The line represents the theoretical prediction of Eq. 8

configuration for the rotation experiments is illustrated schematically in Fig. 11.

As illustrated by Fig. 12, the resultant three-component vector field accurately depicts solid body rotation. The scatter-plots in Fig. 13 show only the measured Δz components, and thus clearly demonstrate the ability of the technique to measure the out-of-plane component in both directions. For both Cases C and D, the rotation angle, determined by applying a linear regression to the Δz information, was found to match the expected θ value to an accuracy well within that of the dial gauge measurement. In both cases the R^2 coefficient of the Δz regression line exceeded 0.99.

Fig. 11 Test configuration for the rotation cases. Configuration is based on a test plate mounted on a PC controlled turntable illuminated by twin white light sources. Also shown are symmetric CCD cameras in the standard Scheimpflug configuration

The probability density functions for the three components are plotted in Fig. 14 for Case C. As the signal varies with X, the measurements have not been normalised, meaning that the ε values are greater than those presented in Fig. 9. As with Fig. 9, the ε probability density function is similar for the Δx and Δz components.

6 Measurement of a rotating flow

A complex rotating flow was measured as a final demonstration of the new technique. A cylindrical container was screwed onto the turntable setup used for the solid-body rotation test, in such a way that the rotating platform fit closely to the cylinder wall but was capable of independent rotation. As illustrated schematically in Fig. 15, a column of water of height, H, equal to 1.5 times the radius of the disk, R, was added to the cylinder. The disk was rotated at constant angular velocity (ω) using the micro-stepping controller. The camera angles used were ±45°, respectively. The Reynolds number of the flow, given by $Re = \omega R^2/v$, where v is the kinematic viscosity, was equal to 1,200. The flow produced in a cylinder with a free-surface by a rotating disk was first observed by Spohn et al. (1993) and has recently been used to study potential bio-reactor applications (Dusting et al. 2006). At $Re = 1,200$, there are strong radial, axial and azimuthal velocity components, as well as significant spatial velocity variations across the vessel. As a result, the flow provides a good demonstration of the capabilities of the new technique.

For the SPIV measurements, silver-coated hollow glass spheres of 12 μm diameter (Potters Industries, USA) were seeded into the working fluid and illuminated using Nd:Yag lasers (Spectra-Physics, USA). The laser light sheet was aligned vertically with the meridional plane so that the recirculation pattern in the upper portion of the vessel could be captured. Calibration was undertaken by imaging a sandblasted glass plate and processing using the
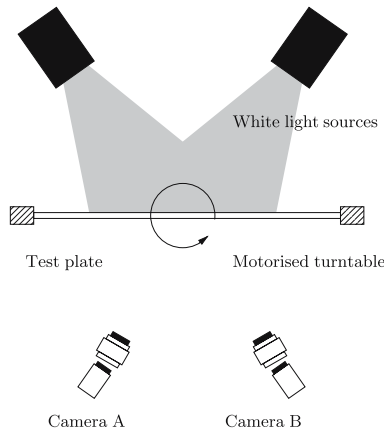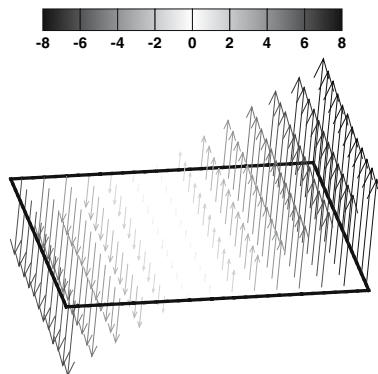
Fig. 12 Reconstructed three-dimensional test case vector field for $\theta = 1.0°$ (Case C). Shading indicates Δz component magnitude
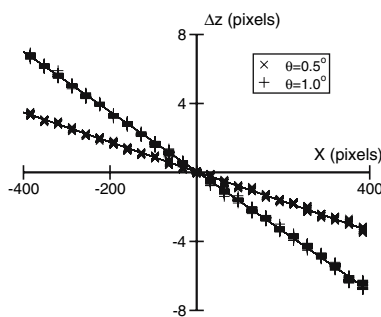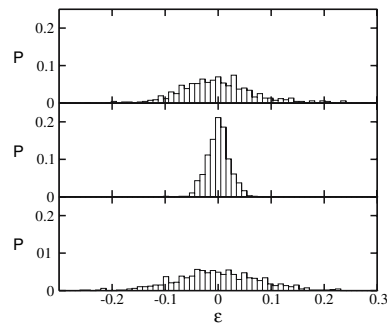

Fig. 14 Probability density function of error ε in the measured displacement components, for the $\beta = 45°$, $\theta = 1.0$ rotation case (Case C). The top plot shows the Δx component, the middle plot shows the Δy component and the lower plot shows the Δz component
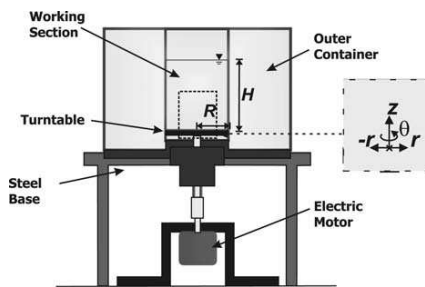

Fig. 13 Reconstructed Δz component as a function of X, for the $\beta = 45°$, rotation cases. The different shaped symbols represent the two different solid body rotation angles, as denoted by the figure legend

Fig. 15 Experimental setup for the rotating flow, including coordinate system and the measured region of interest

three-component reconstruction, thus illustrating the robustness of the new technique.

new technique, as described previously. The resulting normalised three-component vector field for the $Re = 1,200$ case is shown in Fig. 16. For the sake of clarity, every second vector has been omitted and only the right-hand side is shown. The in-plane vector field, shown in Fig. 17, contains excellent resolution of a reversed-flow vortex breakdown bubble located near the cylinder axis of symmetry, as well as the main meridional-plane recirculation. The corresponding azimuthal velocity (v_θ) distribution is shown in Fig. 18. The predominantly azimuthal flow produces a large out-of-plane component, meaning that it is likely that the left and right camera PIV vector fields have relatively high σ_p errors. Despite this, the three-component SPIV vector field was successfully captured by performing

7 Conclusions

A new calibration technique for Stereo PIV has been developed. The use of a contiguous target and PIV interrogation to derive the distortion map makes the process simple to implement, as much of the geometric analysis is no longer necessary. Furthermore, no interpolation is required since a common grid is used for both the distortion analysis and the flow analysis. Importantly, the calibration process also automatically takes into account any discrepancy between the field of view on the left and right camera images, thus reducing the sensitivity to camera misalignments, lens misalignments, or magnification differences.
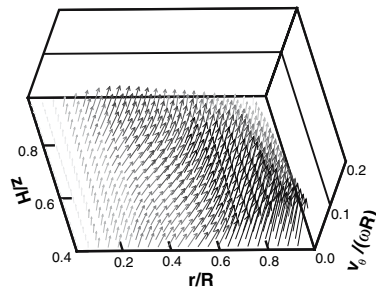
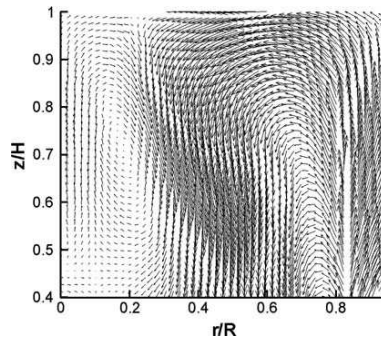**Fig. 16** Three-dimensional vector field for the rotating flow

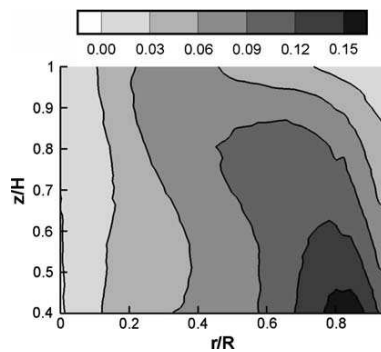**Fig. 17** Meridional plane vector field for the rotating flow

Fig. 18 Distribution of azimuthal velocity component normalised by maximum disk speed for the rotating flow

The new system has been tested under conditions of pure translation and pure rotation. As part of this process, the system has been tested for the case where there is

significant motion in the out-of-plane direction, as well as significant motion within the image plane. The system has also been evaluated at multiple camera displacement angles. In all cases, accurate measurement of the test sample motion was obtained in Δx, Δy, and Δz. Standard deviations of less than 0.2% of the signal were consistently achieved.

A thorough error analysis of the geometric reconstruction has been performed. The measured ratios of σ_x and σ_z to σ_p agree closely with the trends predicted by Prasad and Adrian (1993). The most accurate configuration for the measurement of Δx and Δz was determined to be a symmetric camera geometry, with small camera spacing for Δx and large camera spacing for Δz. The optimal configuration for overall measurement accuracy was found to be any geometry with a relative angle of 90° between cameras. Furthermore, it was found that under certain achievable circumstances, the error due to inaccurate measurement of camera geometry was zero. The level of measurement accuracy resulting from this new, simple technique may reduce the advantage in using more complicated SPIV techniques such as three-dimensional calibration.

References

Arroyo M, Greated C (1991) Stereoscopic particle image velocimetry. Meas Sci Technol 2:1181–1186

Dusting J, Sheridan J, Hourigan K (2006) A fluid dynamics approach to bioreactor design for cell and tissue culture. Biotechnol Bioeng 94:1196–1208

Fouras A, Soria J (1998) Accurate out-of-plane vorticity calculation from in-plane velocity vector field data. Exp Fluids 25:409–430

Fouras A, Hourigan K, Kawahashi M, Hirahawa H (2006) An improved free surface topographic technique. J Vis 9:49–56

Hori T, Sakakibara J (2004) High-speed scanning stereoscopic piv for 3d vorticity measurement in liquids. Meas Sci Technol 15:1067–1078

Lawson N, Wu J (1997a) Three-dimensional particle image velocimetry: error analysis of stereoscopic techniques. Meas Sci Technol 8:894–900

Lawson N, Wu J (1997b) Three-dimensional particle image velocimetry: experimental error analysis of a digital angular stereoscopic system. Meas Sci Technol 8:1455–1464

Lindken R (2006) Stereoscopic micro particle image velocimetry. Exp Fluids 41:161–171

Perret L, Braud P, Fourment C, David L, Delville J (2006) 3-component acceleration field measurement by dual-time stereoscopic particle image velocimetry. Exp Fluids 40:813–824

Prasad A (2000) Stereoscopic particle image velocimetry. Exp Fluids 29:103–116

Prasad A, Adrian R (1993) Stereoscopic particle image velocimetry applied to liquid flows. Exp Fluids 15:49–60

Raffel M, Willert CE, Kompenhans J (1998) Particle image velocimetry: a practical guide. Springer, Berlin

Schroder A, Kompenhans J (2004) Investigation of a turbulent spot using multi-plane stereo particle image velocimetry. Exp Fluids 36:82–90
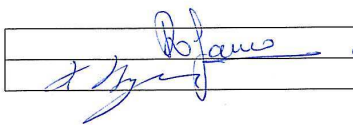
Soloff SM, Adrian RJ, Liu ZC (1997) Distortion compensation for generalized stereoscopic particle image velocimetry. Meas Sci Technol 8:1441–1454

Spohn A, Mory M, Hopfinger EJ (1993) Observations of vortex breakdown in an open cylindrical container with a rotating bottom. Exp Fluids 14:70–77

Wieneke B (2005) Stereo-piv using self-calibration on particle images. Exp Fluids 39:267–280

Willert C (1997) Stereoscopic digital particle image velocimetry for application in wind tunnel flows. Meas Sci Technol 8:1465–1479

Zang W, Prasad A (1997) Performance evaluation of a scheimpflug stereocamera for particle image velocimetry. Appl Opt 36:8738–8744

3.3 Target-free stereo PIV: A novel technique with inherent error estimation and improved accuracy

The following paper was published in 2007 in *Experiments in Fluids*. This work was co-authored by D. Lo Jacono and K. Hourigan, and is entitled *"Target-free stereo PIV: A novel technique with inherent error estimation and improved accuracy"*. The paper is reproduced in this thesis directly from the version published online.

Declaration

Declaration for manuscript included in PhD Thesis

Monash University

Declaration for Thesis Chapter 3.3

Declaration by candidate

In the case of Chapter 3.3, the nature and extent of my contribution to the work was the following:

Nature of contribution	Extent of contribution (%)
Conceived initial ideas, initiated the paper, performed experiments, wrote analysis software, analysed data, wrote manuscript, revised manuscript.	60

The following co-authors contributed to the work. Co-authors who are students at Monash University must also indicate the extent of their contribution in percentage terms:

Name	Nature of contribution	Extent of contribution (%) for student co-authors only
Dr D. LoJacono	Performed experiments, analysed data, co-wrote manuscript	N.A.
Professor K. Hourigan	Co-wrote manuscript	N.A.

Candidate's Signature		Date 08 Nov 07

Declaration by co-authors

The undersigned hereby certify that:

(19) the above declaration correctly reflects the nature and extent of the candidate's contribution to this work, and the nature of the contribution of each of the co-authors.
(20) they meet the criteria for authorship in that they have participated in the conception, execution, or interpretation, of at least that part of the publication in their field of expertise;
(21) they take public responsibility for their part of the publication, except for the responsible author who accepts overall responsibility for the publication;
(22) there are no other authors of the publication according to these criteria;
(23) potential conflicts of interest have been disclosed to (a) granting bodies, (b) the editor or publisher of journals or other publications, and (c) the head of the responsible academic unit; and
(24) the original data are stored at the following location(s) and will be held for at least five years from the date indicated below:

Location(s)	Division of Biological Engineering, Monash University.

Signature 1		Date
Signature 2		

RESEARCH ARTICLE

Target-free Stereo PIV: a novel technique with inherent error estimation and improved accuracy

**Andreas Fouras · David Lo Jacono ·
Kerry Hourigan**

Abstract A novel, accurate and simple stereo particle image velocimetry (SPIV) technique utilising three cameras is presented. The key feature of the new technique is that there is no need of a separate calibration phase. The calibration data are measured concurrently with the PIV data by a third paraxial camera. This has the benefit of improving ease of use and reducing the time taken to obtain data. This third camera also provides useful velocity information, considerably improving the accuracy of the resolved 3D vectors. The additional redundancy provided by this third perspective in the stereo reconstruction equations suggests a least-squares approach to their solution. The least-squares process further improves the utility of the technique by means of the reconstruction residual. Detailed error analysis shows that this residual is an accurate predictor of resolved vector errors. The new technique is rigorously validated using both pure translation and rotation test cases. However, while this kind of validation is standard, it is shown that such validation is substantially flawed. The case of the well-known confined vortex breakdown flow is offered as an alternative validation. This flow is readily evaluated using CFD methods, allowing a detailed comparison of the data and evaluation of PIV errors in their entirety for this technique.

A. Fouras (✉) · D. Lo Jacono · K. Hourigan
Fluids Laboratory for Aeronautical and Industrial Research
(FLAIR), Division of Biological Engineering,
Monash University, PO Box 31,
Clayton, VIC 3800, Australia
e-mail: fouras@eng.monash.edu.au

1 Introduction

Stereo particle image velocimetry (SPIV) is now a well-established extension of traditional PIV (Arroyo and Greated 1991; Willert 1997; Prasad 2000). SPIV offers several advantages over standard (or planar) PIV in addition to the resolution of the out-of-plane components. These advantages include the improved accuracy of in-plane components of the velocity field due to removal of perspective error. Recent extensions of SPIV include three-dimensional (3D) high-speed scanning (Hori and Sakakibara 2004), multi-plane SPIV (Schroder and Kompenhans 2004), dual-time SPIV for acceleration measurement (Perret et al. 2006), and stereoscopic micro-PIV (Lindken 2006).

The three-component velocity field is reconstructed based on two velocity fields derived from PIV. This reconstruction process relies on both geometrical equations based on the camera setup, and a calibration step linking the acquired image plane to the object plane.

Following the terminology of Prasad (2000), several techniques exist in order to reconstruct the 3D velocity field from distorted 2D fields, namely geometric reconstruction (Prasad and Adrian 1993), 2D calibration-based reconstruction and 3D calibration-based reconstruction (Soloff et al. 1997).

The calibration based methods correct the unavoidable distortion from the image plane. The difference between two- and 3D techniques is that the latter also involves calibration from the object plane to a number of parallel planes near the imaging plane. These additional calibrations indirectly provide the information relating to the imaging geometry (Prasad 2000; Prasad and Adrian 1993; Raffel et al. 1998; Soloff et al. 1997). These calibration based methods are sensitive to alignment errors in the

\textcircled{2} Springer

positioning of the calibration plate relative to the measurement plane. However, as described by Willert (1997) and furthered by Wieneke (2005) and Fouras et al. (2007), cross-correlation between cameras (of particle images taken at the same instant) can also provide calibration information. For example, Wieneke (2005) provides a system to use this information to provide correction for misalignment of the calibration plate.

Almost all calibrations utilise a target, which consists of a discrete number of markers placed on a regular Cartesian grid (Lawson and Wu 1997). Typically, these targets contain in the order of 100 such markers, i.e., 10×10 grid. The exact method of undertaking this calibration varies depending on the Stereo PIV software being utilised. However, it is largely based on the PIV algorithms themselves and may even require the practitioner to manually identify markers in an image and link them to a corresponding marker on the target. The uncertainty in identifying the position of these markers by use of PIV software is proportional to the size of these markers. The calibration data are then fitted to a polynomial function by least-square means (both linear and non-linear are used).

A technique that offers the advantages of the above techniques, with even greater improvements in reconstruction accuracy and without the requirement of the practitioner to conduct a distinct calibration phase, has been developed based on the work by Fouras et al. (2007). This calibration target free technique utilises a third camera placed in the paraxial (normal to the light sheet) position. This technique is of greatest utility when the paraxial view has minimal distortion or when it is not convenient to place a calibration target in the measurement region. The paper will be divided as follows: a description of the three camera technique; followed by an experimental validation and an extensive error analysis will be presented. The paper concludes with a comparison of Stereo PIV measurements using the novel technique and CFD of a confined vortex breakdown.

2 Description of novel technique

Before PIV interrogation of the image pairs begins, PIV interrogation of the images captured at the same instant is undertaken to determine the distortion or calibration map. The calibration map can be acquired with an accuracy far outstripping that of any discrete system of large markers. This is for two reasons. First, the ability to accurately determine the position of any object is proportional to the size of that object and PIV particles are smaller than the markers on calibration targets. Second, the calibration data can be averaged over the entire series of data acquired under the same stereo imaging parameters. This means that

as the number of PIV measurements increases, the RMS error of the calibration maps approaches zero. Faster convergence to this zero error state can be achieved by the use of correlation averaging (Meinhart et al. 2000). Rather than averaging instantaneous vector fields, this technique involves averaging the cross-correlation function before the peak is determined.

In addition, further improvement is made by making use of the information provided by the third paraxial camera. During the reconstruction phase, there is now considerably more information available than for typical two camera SPIV. A definition of the key spatial variables can be found in Fig. 1. Standard reconstruction solves four equations (δx and δz component of the displacement vector from two cameras) with three unknown terms (δx, δy and δz components of the reconstructed vector). In reality, however, the solution of the δx and δz components of the reconstructed vector are almost completely de-coupled from the solution of the δy component. (Here, as shown in Fig. 1, the plane in which the cameras lie is the xz plane.) This means that the solution of the δy component is, to a large extent, simply the average of the δy component from each camera and that the solution of the δx and δz components of the reconstructed vector is fully constrained problem with two equations and two unknowns. With data available from the third camera, there are now six equations. This allows not only further averaging for the δy component, (reducing errors to $\sqrt{2/3}$ of the level with two cameras), but also now allows for a least-square solution of the δx
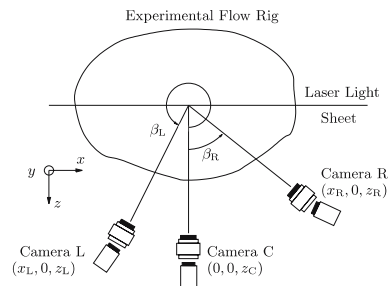

Fig. 1 Schematic diagram of generic Stereo PIV (*SPIV*) configuration including the co-ordinate systems used in this paper. Shown on the figure are the *x*, *y* and *z* axes. The origin of the coordinate system is the point on the laser sheet plane in the center of the imaged region of interest, from the central camera denoted camera C. Also, two additional cameras, denoted left (L) and right (R) for simplicity are shown. Also shown is the Scheimpflug configuration and the definition of the camera angles β_L and β_R, as well as their positions (x_L, 0, z_L) and (x_R, 0, y_R). The paraxial camera (camera C) is held at the angle ($\beta_C = 0$) and at a fixed position (0, 0, z_C) throughout the paper

and δz components with three equations and two unknowns, once again improving accuracy.

The additional information also increases the redundancy contained within the system. In other SPIV systems, if the data from one image are unavailable for some reason during the reconstruction process, such as data rejection during PIV interrogation, a hole appears in those data, as two geometric equations will not suffice to solve for all three unknowns. In the three camera case, if data are unavailable from one camera, then a solution from the remaining two cameras is still viable. The effects of this redundancy grow dramatically with increasing vector failure rates. For the case of 5% vector failure rates, a standard two camera stereo will suffer a failure rate of 9.75%, whereas a three camera technique will only suffer a 0.75% failure rate.

Along with a definition of the key spatial variables, a typical camera configuration for the three camera stereo technique can be found in Fig. 1. The origin of the angles is defined by the paraxial or central camera (here defined as camera C). The practitioner is free to move the cameras to any configuration they choose. This includes the popular arrangement where cameras are symmetrically placed about the laser sheet as opposed to being symmetrically placed about the paraxial position as shown in the schematic.

The entire Stereo PIV technique is described schematically in Fig. 2. All PIV interrogation is performed in real world co-ordinates as measured by the paraxial camera C. This means that measured data are directly utilised in the reconstruction process without the need for any interpolation. To achieve this, mapping functions (MF) for the co-ordinate systems as measured by the stereographic cameras, relative to the paraxial camera, are required. These MFs are directly measured by cross-correlating the images from the paraxial camera with matching images (taken at the same instant in time) from each stereographic camera in turn. These MFs are simply the displacement vector fields of apparent motion of particles as a result of differences of perspective between cameras. It should be noted that, unlike other target based systems where the number of points in the system is limited (i.e., generally in the order of 100), here the number of points is equal to the number of vectors to be sought (typically in the order of $64 \times 64 = 4,096$). These MFs are now used as inputs into the window shifting function (WS) of the PIV software developed by the authors (see CC loop in Fig. 2, right). The displacement vector fields caused by the fluid motion as measured from each of the three perspectives are now measured. Almost all modern PIV software performs WS to improve accuracy and dynamic range. The accuracy can be still further improved by symmetrically shifting both
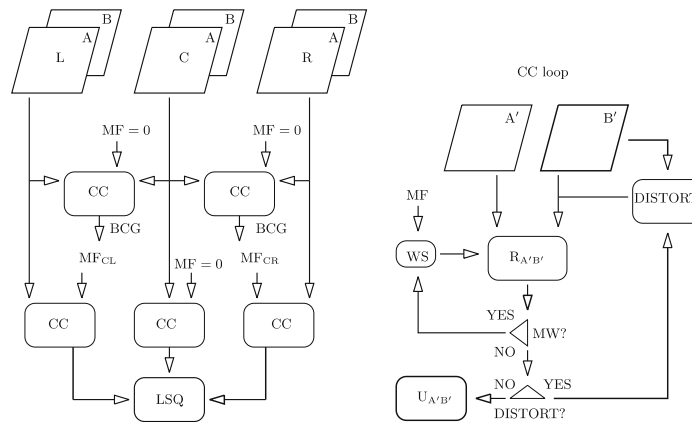

Fig. 2 Schematic diagram showing (*left*) the proposed target-free, three camera Stereo PIV process. Inputs are the image pair sets(denoted *A* and *B*) from the three cameras (here denoted *L*, *C* and *R*). Each set is cross-correlated with the paraxial set (here *C*) in the CC loop in order to generate the corresponding mapping functions (*MF*). These MFs will in turn be used as inputs for the window shifting (*WS*) for the cross-correlation of each set. Finally, the displacement fields of each set are used in a least-square geometric reconstruction method (*LSQ*) to generate the three component vector field. Also shown (*right*) is the cross-correlation process (CC loop) including WS based on the MF and multi-window iteration (*MW*). To reduce peak-locking in the sub-pixel component, an additional distortion loop is included

windows to achieve the same relative displacement (Meunier and Leweke 2003). The only special feature of the PIV software required to perform this calibration is to accept as an input to the displacement vector field of the MF and to displace both windows in the cross-correlation analysis by this amount.

By including the MF into the technique in this way, the requirement to interpolate the data (either the image before the PIV interrogation or the vectors after) is avoided provided the MF data are calculated on the same grid as that on which the flow is to be measured. This grid is defined from the perspective of the paraxial camera.

It can be seen in Fig. 2 that particle image distortion (PID) is employed to reduce peak locking. This PID is used globally (i.e., on the entire image) and not locally (i.e., PIV interrogation window). The interpolation scheme chosen is a bi-cubic interpolation as used by Chen and Katz (2005). The effects of the first pass of PID are shown in Fig. 3.

Specifically in the case of the MFs, peak locking errors may be completely eradicated by replacing the measured data with an analytical representation. This not only removes peak locking but any remaining random errors. The authors wish to stress that PIV random errors will be small because of the averaging process described earlier and that analytical representation is not necessarily required. In this case a cubic representation was chosen. The choice of a cubic dependence in x and y is arbitrary and chosen for its simplicity and high performance (Soloff et al. 1997).

$$\text{MF}(x, y) = a_0 + a_1 x + a_2 x^2 + a_3 x^3 + a_4 xy + a_5 x^2 y \\ + a_6 xy^2 + a_7 y + a_8 y^2 + a_9 y^3, \tag{1}$$

where $\mathbf{a}_i$ are vector valued coefficients to be determined. Because of the large number of points, a least-squares solution by means of a bi-conjugate gradients method (BCG) has been used to determined the coefficients (Press et al. 1992).

Finally, each of the three displacement fields is used in a least-squares geometric reconstruction method (LSQ) to generate the three component vector field on a point by point basis. This is achieved by using the standard pinhole model at each location on the element grid, since each displacement vector field is calculated in the same co-ordinates as the paraxial or center camera. The least-square solver is implemented with singular value decomposition as described in Press et al. 1992). More precisely, the above formulation can be expressed as follows:

$$\begin{bmatrix} 1 & 0 & (\Delta x_1 - x_1)/z_1 \\ 0 & 1 & (\Delta y_1 - y_1)/z_1 \\ \vdots & \vdots & \vdots \\ 1 & 0 & (\Delta x_N - x_N)/z_N \\ 0 & 1 & (\Delta y_N - y_N)/z_N \end{bmatrix} \begin{bmatrix} \delta_x \\ \delta_y \\ \delta_z \end{bmatrix} = \begin{bmatrix} \Delta x_1 \\ \Delta y_1 \\ \vdots \\ \Delta x_N \\ \Delta y_N \end{bmatrix} \tag{2}$$

where (x_i, y_i, z_i) and $(\Delta x_i, \Delta y_i) = (gx_c + \delta_{x_i}, gy_c + \delta_{y_i})$ are the position and the measured projection of the ith camera (measured δ_{x_i} displacement added with the grid position (gx_c, gy_c) from the center of the center camera for varying viewing angle across the image), respectively; and N is the total number of cameras used.

Alternatively, instead of a pinhole model and a single plane calibration technique, a practitioner employing a more widely used technique such as that proposed in Soloff et al. (1997) could utilise many of the advantages described in this paper by making only minor changes to their practice. These changes would include calibrating by traversing the light sheet through their measurement volume and solving the reconstruction equations with a least-squares method.

3 Validation

The performance of the three camera technique was investigated initially with two separate experiments undertaken to test the ability of the new system to measure the classical test cases of pure translation and pure, solid-body rotation. Only a brief overview is given here, since a detailed description of these experiments can be found in Fouras et al. (2007), with the primary difference that three cameras were used in this case as opposed to the standard configuration of two cameras in that work.
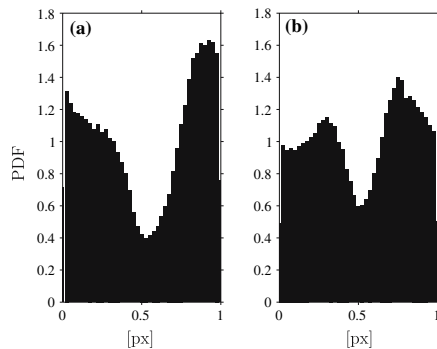

Fig. 3 a Probability density function (*PDF*) of typical sub-pixel component of cross-correlation process. **b** PDF after second image pair is globally distorted by resultant displacement field using bi-cubic interpolation scheme. The figure shows the extent of the peak locking and reduction caused by distortion process

The translation experiments were carried out using two different symmetric camera angles, as SPIV system performance often varies with the camera positions (Lawson and Wu 1997). Camera angles of $\beta_R = -\beta_L = 30°$, and $\beta_R = -\beta_L = 45°$ were chosen, as these represent typical offsets that produce significant image distortion. The flow field was simulated by a sheet of paper printed with a pseudo-random pattern. This paper was fixed between glass plates and attached to a linear traverse driven by a precision ground lead screw driven by a geared stepper motor. The object was positioned for each image using a micro-stepping, stepper motor controller. Images were recorded at 101 positions with a small known displacement between each image. This allowed a flexible system of analysis; by interrogating against different pairs, different length vectors were achieved. Different vector lengths ($k\delta x$: $k = 1,16$) were obtained by analysing $CC(i, i + k)$, where i is the frame number, k is the number of skipped frames, and CC is the cross-correlation process (see Fig. 2). In this manner, 16 reliable data sets of increasing magnitude were obtained. Since image quality and other PIV acquisition and processing parameters were held constant, PIV errors were also held constant in absolute terms. By normalising each data set by the known displacement, 16 data sets with varying levels of PIV accuracy were achieved.

The rotational test cases were performed by rotating a fluid body within a cylindrical vessel. The vessel was first accelerated to a constant rotational rate of $\omega_1 = \pi/4$ rad/s, and the relative fluid motion allowed to decay resulting in solid-body rotation. The rate of decay and the continued damping of any relative fluid motion were enhanced by the use of a glycerine/water mixture as the working fluid. In a manner similar to the translation case, this whole data set was analysed twice to produce data with apparent rotation rates of $\omega_1 = \pi/4$ rad/s and $\omega_2 = \pi/2$ rad/s.

As the theoretical displacements of the translation and rotation test cases are known, statistics can be compiled regarding errors relative to these theoretical values. The theoretical values for the rotation case are based on the known rotation rate, with the center of rotation determined by least-squares fit. The global values for bias (μ) and standard deviation (σ), associated with the 45° translation case (with $k = 16$ corresponding to $\delta x = 33.95$ px) and the ω_1 rotation case are outlined in Table 1. The values are expressed in pixels and represent a combination of the accuracy of the PIV as well as the stereo reconstruction process. The values demonstrate that all three displacement vector components were evaluated with a high degree of precision.

Detailed results from the rotational test cases are displayed in Fig. 4. The figure shows the out of plane displacements δz_1, δz_2 plotted as a function of r^*, the normalised radial position for $\omega_1 = \pi/4$ and $\omega_2 = \pi/2$ rad/s.

Table 1 Table of numerical values of bias (μ) and standard deviation (σ) associated with the ω_1 case shown in Fig. 4

	μ	σ
Translation case (%)		
δx	2.12	1.15
δy	-1.21	0.71
δz	0.61	1.88
Rotation case (10^{-2} px)		
δx	1.01	5.41
δy	0.96	6.35
δz	NA	7.01

As the center of rotation was fitted, the bias value for δz is necessarily zero and hence is not included

Solid lines indicate the theoretical $\delta z_{(1,2)}$ values. Error bars show the localised (for each r^*) standard deviation of the measured values when compared to the theoretical ones. The error bars clearly show that the relative errors are small and do not vary significantly over the radius.

Figure 5 shows the probability density function (PDF) of errors associated with δz_1 case shown in Fig. 4. The error is simply the difference between the measured and the theoretical value. The theoretical values of δx and δy are assumed to be zero. The solid lines shown in Fig. 5 indicate Gaussian curves with standard deviations and means taken from Table 1. The PDF envelopes closely match Gaussian profiles indicating the Gaussian nature of the errors. This information is of importance and will be be utilised in the error analysis of Sect. 4.
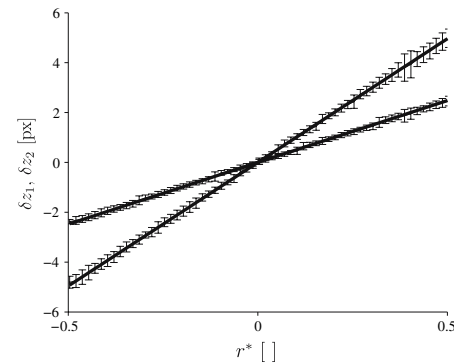

Fig. 4 Out of plane displacement components δz_1 and δz_2 plotted as a function of r^*, the normalised radial position, for the rotational cases of $\omega_1 = \pi/4$ rad/s and $\omega_2 = \pi/2$ rad/s, respectively. *Solid lines* indicate theoretical $\delta z_{(1,2)}$ values based on these rotation rates, with the center of rotation determined by least-squares fit. *Error bars* show the standard deviation of the measured values when compared to the theoretical ones
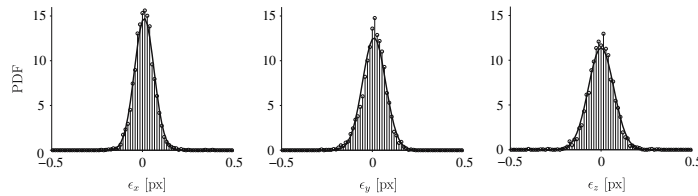
Fig. 5 Probability density function of errors (denoted $\epsilon = (\epsilon_x, \epsilon_y, \epsilon_z)$) for each of three components associated with ω_1 case shown in Fig. 4. Theoretical values of δx and δy are assumed to be zero. *Solid lines* indicate Gaussian curves with matching values for the standard deviation and mean. Error data closely match Gaussian profiles indicating the Gaussian nature of the errors

Table 2 shows the changes in the statistics shown in Table 1 with one of the MFs set to null. The changes are typically less than 2%. The results clearly show the insensitivity to changes in the MF and hence the calibration technique. The insensitivity of these results to very large errors in the MF calls into question the very practice of using these classical test cases to validate SPIV techniques. The authors believe that other more complex test cases are required to properly validate SPIV techniques. This is supported by the findings of Scarano et al. (2005) that a truly 3D flow configuration is required to fully test their stereo configurations. One alternative validation case is discussed in Sect. 5.

4 Error analysis

Several authors have derived error analysis from the equations of the reconstruction process. The current technique differs from those techniques in that the reconstruction process is a least-squares process and while analytical error analysis of a least-squares process is possible (Fouras and Soria 1998), it is limited and not straightforward. In this case, it is more appropriate to perform a Monte Carlo simulation to assess the sensitivity

Table 2 Table of numerical values of relative changes to bias ($\Delta\mu$) and standard deviation ($\Delta\sigma$) associated with the translation and rotation case when one of the MFs are set to null

	$\Delta\mu$ (%)	$\Delta\sigma$ (%)
Translation case		
δx	1.90	0.03
δy	0.20	<0.01
δz	4.90	0.02
Rotation case		
δx	0.98	1.13
δy	0.32	1.97
δz	0.07	0.17

of the reconstructed 3D vector errors to the multiple input 2D vector errors.

The input errors will be denoted as ϵ_{in}, which are the two component random displacement errors as viewed from each camera. The standard deviation of ϵ_{in} is defined as $\boldsymbol{\sigma}_{\mathrm{in}} = (\sigma_{\mathrm{in}}^x, \sigma_{\mathrm{in}}^y) = \sigma(\epsilon_{\mathrm{in}})$. A variable σ_{piv} which represents the PIV measurement error of a single component as measured by the paraxial camera is used here. Because vector errors are proportional to particle image size, component stereographic displacement vectors have the following errors relative to σ_{piv}:

$$\begin{aligned} \sigma_{\mathrm{in}}^x &= \sigma_{\mathrm{piv}} / \cos(\beta), \\ \sigma_{\mathrm{in}}^y &= \sigma_{\mathrm{piv}}. \end{aligned} \tag{3}$$

The output errors will be denoted as ϵ_{out}, which is the three component reconstructed displacement error. The standard deviation of ϵ_{out} is defined as $\boldsymbol{\sigma}_{\mathrm{out}} = (\sigma_{\mathrm{in}}^x, \sigma_{\mathrm{in}}^y, \sigma_{\mathrm{in}}^z) = \sigma(\epsilon_{\mathrm{out}})$.

Monte Carlo simulations were performed by creating displacement vector fields with pseudo-random Gaussian distributions. It was then confirmed that similar to the errors shown in Fig. 5, the output errors were Gaussian and proportional to the input errors. As a result, we are freed to investigate the sensitivity or the ratio of the output error to the input error at any arbitrary input error level. All further simulations were conducted with the arbitrary input error of $\sigma_{\mathrm{piv}} = 0.1$ px with δx and δy component errors dictated by equations (Eq. 3). The left and right displacement fields were used with and without the center camera displacement field, to simulate both two and three camera technique sensitivities, respectively.

The base case for these Monte Carlo simulations was the symmetric 45° camera configuration. Figure 6 shows the result of 3,600 samples (4% of total data volume used for statistics) of the Monte Carlo simulation for the base case. Shown in the figure is the mean (averaged across two or three cameras as appropriate) of the norm of the input errors, $\mu(\|\epsilon_{\mathrm{in}}\|)$, versus the norm of the reconstructed errors, $\|\epsilon_{\mathrm{out}}\|$, for both two and three cameras, denoted with the superscript 2c and 3c, respectively. In both cases, an

Fig. 6 Scatter plot of the norm of the mean of the norm of the input errors, $\mu(\|\epsilon_{in}\|)$, versus the norm of the reconstructed errors, $\|\epsilon_{out}\|$, for two and three cameras (denoted with the superscript 2c and 3c, respectively) on the left and right, respectively
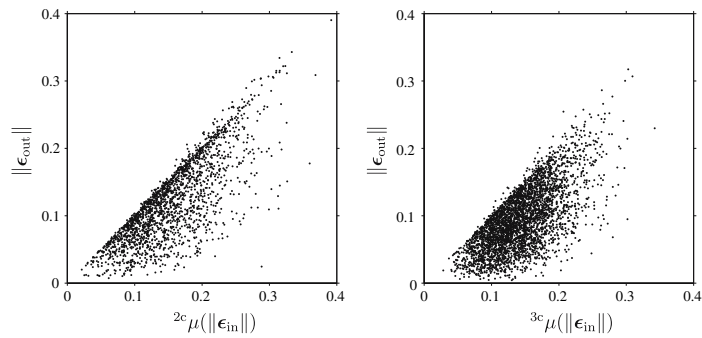

upper bound on the $\|\epsilon_{out}\|$ data is apparent. This indicates that all cases of a high output error are the result of a high input error. A linear fit to each scatter plot yields values for the residual of 0.625 and 0.467 for two and three cameras, respectively. This signifies that high values of input errors are less likely to result in high values of output errors in the three camera case than for the two camera case. This is further evidenced by the fact that, overall, the $\|\epsilon_{out}\|$ data are lower for the three camera case than the two camera case.

Wieneke (2005) utilised the residual of the reconstruction process to identify errors in the input displacement vectors; these data are then rejected from the process. This is an interesting idea worth investigating. Figure 7 shows the results from the same Monte Carlo simulation, as discussed above, as a scatter plot of the square-root of the residual of reconstruction, $\chi = \sqrt{\chi^2}$, versus the mean of the norm of the input errors $(\mu(\|\epsilon_{in}\|))$ for two and three cameras on the left and right, respectively. For the two camera data (on the left), the solid line follows $\mu(\|\epsilon_{in}\|) = \sqrt{2}\chi$. In this figure, we can see that for the case of two cameras the data are upper bound by the line

$\mu(\|\epsilon_{in}\|) = \sqrt{2}\chi$ but only weakly correlated. This indicates that using the residual as an indicator of input errors would be inaccurate and unreliable. For example, a low value of χ does necessarily correspond to a low value of $^{2c}\mu(\|\epsilon_{in}\|)$. However, a high value of χ does not at all necessarily correspond to a high value of $^{2c}\mu(\|\epsilon_{in}\|)$. While this indicator is not reliable for the two camera case, for three cameras the data were more strongly correlated (the line of best fit indicated by the solid line). This means that the indicator is in general more accurate. This is manifested in the fact that a high value of χ corresponds to an increased probability of a high value of $^{3c}\mu(\|\epsilon_{in}\|)$. However, it must be noted that even in the three camera case, the reconstruction residual is not reliable on an individual, point-by-point, basis.

It is also interesting to investigate the possible correlation between the residual of the reconstruction process with errors in the reconstructed vector. Figure 8 shows the results from the same Monte Carlo simulation, discussed above, as a scatter plot of the residual of reconstruction, χ, versus the norm of the output errors $(\|\epsilon_{out}\|)$ for two and three cameras on the left and right, respectively. Note that

Fig. 7 Scatter plot of the residual of reconstruction, χ, versus the norm of the input errors, $\|\epsilon_{in}\|$, for two and three cameras (denoted with the superscript 2c and 3c, respectively) on the *left* and *right*, respectively. The *solid lines* on the graphs follow $\|\epsilon_{in}\| = \sqrt{2}\chi$ and the line of best fit for the left and right, respectively
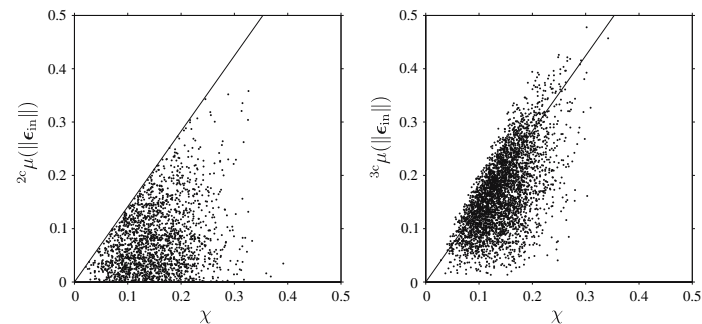
Fig. 8 Scatter plot of the residual of reconstruction, χ, versus the norm of the reconstruction errors, $\|\boldsymbol{\epsilon}_{\text{out}}\|$, for two and three cameras on the *left* and *right*, respectively. Note that in the case of two cameras, the data are completely uncorrelated, while for the case of three cameras the scatter plot shows only very weak correlation which indicates that there is little value in using χ as a metric of the output error on a point-by-point basis
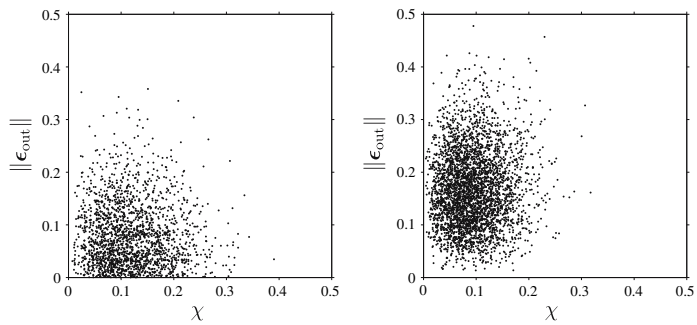
in the case of two cameras, the data are completely uncorrelated, and that for the three camera configuration the scatter plot shows only very weak correlation. This signifies that there is little value in using χ as a metric of the output error on a point-by-point basis.

What is significant, however, is that while these values are not very well correlated to each other on a point-by-point basis, on an ensemble or global basis the correlation is perfect. Figure 9 illustrates the perfect correlation between χ and both the input errors σ_{piv} and output errors $\|\boldsymbol{\sigma}_{\text{out}}\|$ for a 45° camera setup. This suggests that when the pinhole model reconstruction equations are solved using a least-squares method, the global mean of the residual, χ, may be used as an indicator of not only the input errors, but more usefully, the errors in the reconstructed vectors.

Several further points can be made about the data in Fig. 9. The unity slope in the log–log plot indicates that the relationship between $\mu(\chi)$ and the input and output errors is linear. Furthermore, the slightly greater difference between σ_{piv} and $\|\boldsymbol{\sigma}_{\text{out}}\|$, on the left figure compared to the right shows that the three camera technique is less sensitive to input errors.

The data from the Monte Carlo simulation can now be analysed to calculate the sensitivity of the least-squares reconstruction process, by comparing the global standard deviation of the outputs errors and the reconstruction residual to the global standard deviation of the input errors σ_{piv}. This analysis can be repeated for all values of β_L and β_R. The results of these simulations can be seen in Fig. 10.

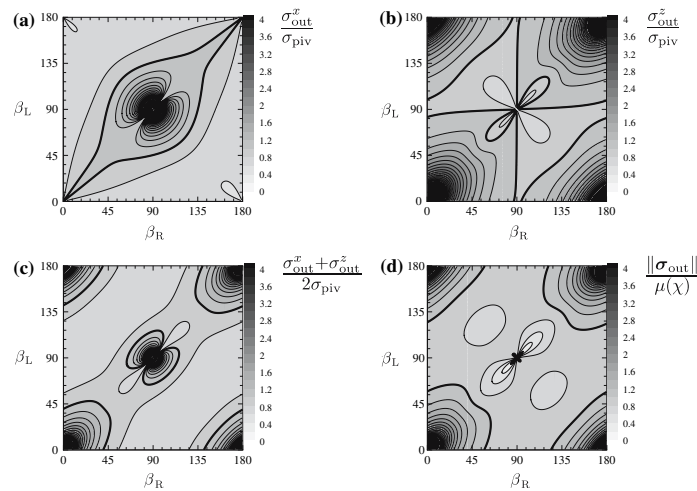For the δx projection, Fig. 10a, the sensitivity to input errors is lowest when the cameras are placed close to the paraxial position and symmetrically opposed to each other (or the opposite paraxial position). However, in this case, there appears a second area of low sensitivity along the line of $\beta_L = \beta_R$. This counter-intuitive result can be explained by the presence of the paraxial camera and the fact that along this line, the errors on stereographic cameras will cancel. This analysis assumes that errors are independent variables and ignores the impracticality of conducting experiments with $\beta_L \approx \beta_R$. One final point to note is that the sensitivity results shown are significantly less than those for two cameras reported in Fouras et al. (2007) and Lawson and Wu (1997).

Fig. 9 For a 45° camera setup, several magnitudes of random error, σ_{piv}, were introduced. Plotted against the global mean of the square-root of χ^2 ($\mu(\chi)$) are σ_{piv} (*square*) and $\|\boldsymbol{\sigma}_{\text{out}}\|$ (*circle*) showing a perfect dependency for both two camera (*left*) and three camera (*right*) configurations. The *solid line* follows a linear best fit
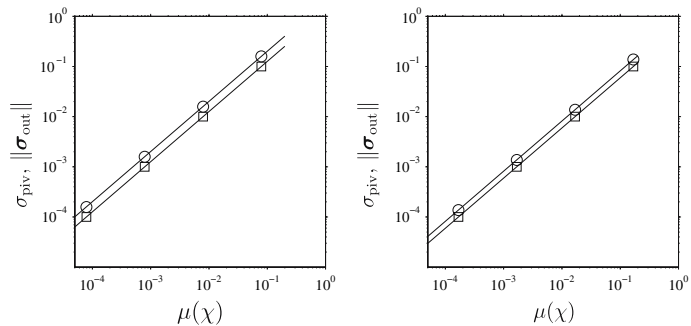
Fig. 10 Sensitivity of the three camera technique calculated by numerical Monte Carlo analysis as a function of camera angles with one camera fixed at the paraxial position (camera C). **a**, **b** Show the sensitivity of the x and z components. **c** is the average of **a** and **b**. **d** Shows the global mean of the residuals from the least-square solution ($\mu(\chi)$) of the 3D vector reconstruction. The *bold line* indicates the boundary of the iso value equal to 1.0, and the iso-values vary in steps of 0.2

Logically the next quantity to examine for sensitivity is δy. This is not shown in the figure, since the result is trivial. The reconstructed δy component is effectively always equal to the average of the δy measurements from each of the stereographic cameras. This results in the values for the sensitivity of $1/\sqrt{2}$ for two cameras and $1/\sqrt{3}$ for three cameras.

Along the δz projection, Fig. 10b, the sensitivity to input errors is the lowest when the cameras are placed far from the paraxial position (i.e., close to the laser position) and symmetrically opposed to each other (or the opposite paraxial position). Again in this case appears a second area of low sensitivity along the line of $\beta_L = \beta_R$, for which an explanation similar to that for the δx projection is viable.

The form of Fig. 10c, showing the measure of the average of σ_{out}^x and σ_{out}^z, is readily explained via the results of the components. Of interest is that, while similar to the two camera case (Fouras et al. 2007) with a minimum along the line of $\beta_L - \beta_R = 90°$ (which includes the symmetric case of $\beta = \pm45°$), there is a very broad minimum along a curved line near to $\beta_L - \beta_R = 90°$. In this case the minimum lies at $\beta = \pm50°$. This broader stereo angle is explained by the reduction in the δx error, affording more significance to the δz component, which is reduced by broader stereo angles.

Finally, in Fig. 10d, we can see a plot of $\|\sigma_{out}\|/\mu(\chi)$ as a function of β_L and β_R. The authors wish to stress that by calculating this value for their experimental configuration, a practitioner has direct access to an effective estimate of both their input and output errors. The practitioner simply has to calculate the ensemble average of the residual χ of

the least-squares reconstruction process, multiply this value by the gradient value and they have this accurate indication of the errors of a particular set of stereo measurements. This is without any theoretical or computational estimate of the displacement or velocity field. An example application of this predictor will be presented in Sect. 5.

As described in Sect. 3, the methodology undertaken to test the SPIV technique for translation cases allowed the level of PIV accuracy to be controlled. By varying the displacement of the target between images, 16 different values of σ_{in}^x, the standard deviation of the PIV processing error, σ_{piv}, were achievable. This facilitated a comparison between the standard deviation of the reconstructed stereo error, $\|\sigma_{out}\|$, and σ_{piv}. The solid lines follow the theoretical prediction taken from the error analysis shown in Fig. 10. This further verifies this analysis as the agreement between experimental values and Monte Carlo simulation are excellent.

These results are significant not only for their validation of the Monte Carlo simulation but also when compared to the results of other papers that describe this sensitivity for standard two camera stereo techniques. A complete error analysis for the standard two camera stereo system is performed in Fouras et al. (2007). For the symmetric case (as is displayed in Fig. 11), the same results have also been reported by Lawson and Wu (1997). In Table 3 the results for the cases of $\beta_L = -\beta_R = 30°$ and $\beta_L = -\beta_R = 45°$ are compared with the results calculated in Figs. 10 and 11. The results for the two cameras show perfect agreement with the published values in Fouras et al. (2007) and Lawson and Wu (1997) which both utilise different techniques. Significant

Fig. 11 Sensitivity of the three camera technique measured with $\beta_L = -\beta_R = 30°$ (*left*) and $\beta_L = -\beta_R = 45°$ (*right*). Measurements taken on the translation experiment with 16 different displacements. *Diamond* and *square symbols* represent σ_{out}^z and σ_{out}^x, respectively. Associated *solid lines* follow the theoretical prediction taken from the error analysis shown in Fig. 10
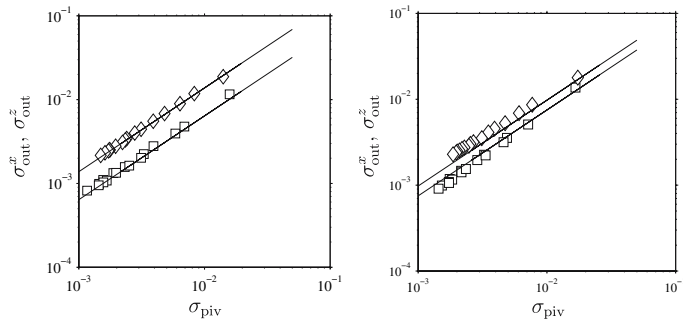

Table 3 Sensitivity of 3D reconstructed σ_{out}^x and σ_{out}^z to σ_{in}^x for symmetric 30° and 45° cases with both two and three cameras

	$^{3c}\sigma_{out}^x$	$^{2c}\sigma_{out}^x$	$^{3c}\sigma_{out}^z$	$^{2c}\sigma_{out}^z$
30°	0.640	1.000	1.383	1.732
45°	0.750	1.000	0.976	1.000

Note the sensitivity of the δx component is reduced while the sensitivity of the δz component is unchanged

improvement in the sensitivities of the δx and δy components are apparent when using three cameras.

5 Comparison with CFD of confined vortex breakdown

The flow within a closed cylindrical cavity with a rotating lid is considered. This type of flow has been the focus of earlier studies (see for example Vogel 1968; Escudier 1984; Lopez 1990; Sørensen and Christensen 1995; Spohn et al. 1998). Surprisingly, this flow has not been measured experimentally in a quantitative manner, with more than two velocity components. A similar flow has been measured at FLAIR (Dusting et al. 2006), however, this was for the particular case with a free surface. Due to the simple geometry of the closed cavity and the existence of efficient axisymmetric Navier–Stokes solvers, this type of problem is highly suitable as a benchmark for all SPIV measurements. The simulation presented here was produced by an axisymmetric DNS solver. A detailed description of the formulation and numerical implementation can be found in Sørensen and Loc (1989).

5.1 Experimental setup

As shown in Fig. 12, the experimental apparatus consisted of an octagonal shaped container. A circular cylinder (radius $R = 32.5$ mm) was placed in its center. The aspect
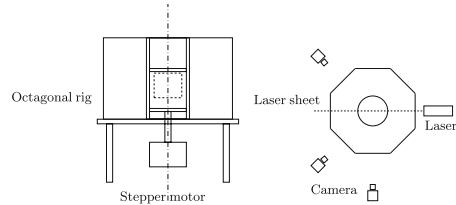

Fig. 12 Schematic diagram of the experimental apparatus. *Left* side-view, where the *dashed window* shows the measured region. *Right* top-view showing apparatus and position layout of the laser sheet and the cameras. Note the octagonal shaped rig used to reduce distortion and the symmetric layout of the cameras about the laser sheet

ratio (height to radius), of the cylindrical cavity (H/R) is controlled by varying the position of the top disk. The octagonal shape allows the exterior faces of the rig to be flat in order to reduce refraction effects that result in optical distortion errors during the use of image-based measurement techniques. A flat, circular disk acted as the rotating bottom, and was located in the center of the base. The disk was rotated by means of a stepper motor and high-performance motion controller (National Instruments, USA).

The Stereo PIV technique detailed in Sect. 2 was used to measure this flow. Imaging was performed using three PixelFly (PCO, Germany) cameras with a resolution of $1,360 \times 1,024$ pixels. Magnification of 20.4 px/mm resulted in the relatively large field of view as shown schematically with dashed lines in Fig. 12. The stereo configuration used was $\beta_L = -45°$ and $\beta_R = 225°$. Illumination was provided by a QuantaRay (SpectraPhysics, USA) double pulsed NdYag Laser, focused into a 1 mm thin light sheet. The tracer particles used were Sphericel (Potters Industries, USA), silver coated hollow glass microspheres with a nominal diameter of 14 μm and specific gravity of 1.6 (Fig. 13).
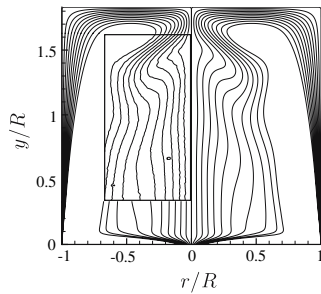
Exp Fluids

Fig. 13 Comparison of matched iso-contours for the out-of-plane velocity component between symmetric experimental data (in the *boxed region*) and numerical data (in the *surrounding region*)

PIV analysis was performed (see Fig. 2b) with a multi-window iterative analysis, a final window size of 16×16 px and a spacing between sampling windows of 8×8 px. As the flow was steady images pairs were analysed using correlation averaging to produce more accurate results.

5.2 Results and discussion

The Reynolds number based on the the radius of the cavity and the tip speed of the rotating lid is defined as $Re = \omega R^2 / v$, where v is the kinematic viscosity of the fluid. Data presented here are taken from experiments conducted at $Re = 2,200$ and $H/R = 1.85$. Under these conditions, the flow is steady and contains one vortex breakdown (Escudier 1984). For the sake of brevity, this paper will focus on the out-of-plane component since this is the reconstructed component.

In these types of flow, it has been found that even the slightest imperfections in the apparatus will create asymmetries (Thompson and Hourigan 2003). In order to validate against an axisymmetric CFD simulation, flow measurements have been averaged to produce symmetric data. All experimental data are non-dimensionalised with the previously defined characteristic scales to allow direct comparison with numerical results.

Figure 14 shows the comparison of matched iso-contours for the out-of-plane velocity component between symmetric experimental data (in the boxed region) and numerical data (in the surrounding region). Note the excellent agreement between the numerical and the experimental data. It should be recall that there is no smoothing or filtering of the experimental data from the SPIV process. The PDF of the relative error of these data is shown in Fig. 14. As a direct result of the enforced symmetry, the
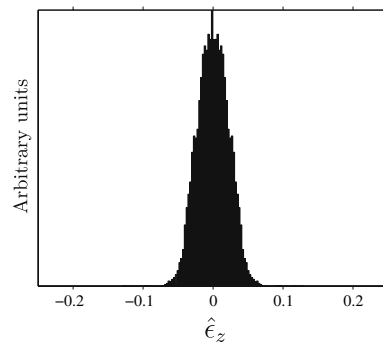

Fig. 14 Probability density function of the δz component of relative velocity error $(\hat{\epsilon} = (\mathbf{u}_{exp} - \mathbf{u}_{num}) / \max(\mathbf{u}_{num}))$. The Gaussian nature of this error is clearly visible

PDF shows no bias error. However, the Gaussian nature of the errors and the low magnitude of these errors can be clearly seen.

Tabulated data of the errors for all three velocity components are presented in Table 4. The bias and standard deviations indicate the high degree of accuracy to which the flow has been measured. Also shown are the $\Delta \mu$ and $\Delta \sigma$ values which are the relative differences introduced by setting one of the MFs to null. Note that unlike the translation and rotation cases shown in Table 2, the change is significant when compared to data with the correct MFs. This demonstrates that when the mapping process has errors introduced, errors of similar magnitude appear in the reconstructed errors. The confined swirling flow (combined with its evaluation with CFD) is therefore a candidate as a benchmark flow for Stereo PIV.

As discussed in Sect. 2, the least-squares solution not only provides a highly accurate solution for the reconstructed vector field but also a useful residual. In Fig. 9, it was shown that the mean of the residual, $\mu(\chi)$, should be an reliable indicator of the accuracy of the experimental

Table 4 Table of numerical values of relative bias and standard deviation (σ) associated with the confined vortex breakdown, at $Re = 2,200$, when compared to numerical simulation

	μ (10^{-2})	$\Delta\mu$ (%)	σ (10^{-2})	$\Delta\sigma$ (%)
$\hat{\epsilon}_x$	NA	NA	4.38	24.06
$\hat{\epsilon}_y$	−1.84	41.51	3.49	27.62
$\hat{\epsilon}_z$	NA	NA	2.21	54.90

Also shown are the $\Delta\mu$ and $\Delta\sigma$ values which are the differences introduced by setting one of the MFs to null. Note that the change is significant when compared with data with the correct MFs

Table 5 Table of the accuracy of the predicted errors for the rotational case presented in Sect. 3 and the vortex breakdown case

	$\mu(\chi)$	Predicted $\|\boldsymbol{\sigma}_{\mathrm{out}}\|$	Measured $\|\boldsymbol{\sigma}_{\mathrm{out}}\|$
Rotation case	0.1227	0.1003	0.1091
Vortex breakdown case	0.3623	0.2961	0.3230

Predicted $\|\boldsymbol{\sigma}_{\mathrm{out}}\|$ is the product of $\mu(\chi)$ and the value of the gradient of the Monte Carlo simulation shown in Figs. 9 and 10d at the appropriate angles

results. For a particular configuration, Fig. 10d provides the practitioner with $\|\boldsymbol{\sigma}_{\mathrm{out}}\|/\mu(\chi)$. Therefore it is a trivial task to obtain a estimate of the measurement error by multiplying this value by the $\mu(\chi)$ valued obtained during the application of the reconstruction process to experimental data. Table 5 illustrates the usefulness of the mean residual $\mu(\chi)$. The accuracy of the predicted errors for the rotational case presented in Sect. 3 and the vortex breakdown case is given. The reader will appreciate the good agreement between the predicted and the measured error. The measured errors are slightly underestimated, a fact readily explained by the absence of calibration and other systematic, non-random errors in the Monte Carlo analysis.

6 Conclusions

A novel, accurate and simple Stereo PIV technique utilising three cameras has been presented. The key feature of the new technique is the elimination of a separate calibration phase. The calibration data are measured concurrently with the PIV data by a third paraxial camera. This has the benefit of improving ease of use and reducing the time taken to obtain data. These benefits can be achieved only if the paraxial view can be imaged with minimal distortion, which is in general the case, but for complex geometries distortion can often be minimised, for example, with the octagonal shaped rig as used in this study.

The new technique is rigorously validated using both pure translation and rotation test cases. However, while this kind of validation is standard, it is shown that such validation is substantially limited and an improved validation process is required.

This third camera also provides useful velocity information, significantly improving the accuracy of the resolved 3D vectors. It has been found that a fixed improvement of $\sqrt{2/3}$ improvement in the accuracy of the δy component can be achieved. Similar improvements (which are a function of camera stereo angles) are achieved for the δx and δz vector components.

The use of a least-squares approach to the solution of the reconstruction equations further improves the utility of

the technique by providing a robust and useful residual. While it has been shown that on an individual vector basis the residual is not meaningful, thorough error analysis shows that on a global basis this residual is an accurate predictor of resolved vector errors. This powerful predictive tool could possibly be used in conjunction with techniques other than that suggested here, provided it solves the reconstruction process with a least-squares process.

References

Arroyo M, Greated C (1991) Stereoscopic particle image velocimetry. Meas Sci Technol 2:1181–1186

Chen J, Katz J (2005) Elimination of peak-locking error in PIV analysis using the correlation mapping method. Meas Sci Technol 16:1605–1618

Dusting J, Sheridan J, Hourigan K (2006) A fluid dynamics approach to bioreactor design for cell and tissue culture. Biotechnol Bioeng 94:1196–1208

Escudier M (1984) Observations of the flow produced in a cylindrical container by a rotating endwall. Exp Fluids 2:189–196

Fouras A, Soria J (1998) Accurate out-of-plane vorticity calculation from in-plane velocity vector field data. Exp Fluids 25:409–430

Fouras A, Dusting J, Hourigan K (2007) A simple calibration technique for stereoscopic particle image velocimetry. Exp Fluids 42:799–810

Hori T, Sakakibara J (2004) High-speed scanning stereoscopic PIV for 3d vorticity measurement in liquids. Meas Sci Technol 15:1067–1078

Lawson N, Wu J (1997) Three-dimensional particle image velocimetry: experimental error analysis of a digital angular stereoscopic system. Meas Sci Technol 8:1455–1464

Lindken R (2006) Stereoscopic micro particle image velocimetry. Exp Fluids 41:161–171

Lopez J (1990) Axisymmetrical vortex breakdown. Part 1. Confined swirling flow. J Fluid Mech 221:533–552

Meinhart CD, Werely ST, Santiago JS (2000) A PIV algorithm for estimating time-avergaed velocity fields. J Fluids Eng 122:285–289

Meunier P, Leweke T (2003) Analysis and minimization of errors due to high gradients in particle image velocimetry. Exp Fluids 35:408–421

Perret L, Braud P, Fourment C, David L, Delville J (2006) 3-Component acceleration field measurement by dual-time stereoscopic particle image velocimetry. Exp Fluids 40:813–824

Prasad A (2000) Stereoscopic particle image velocimetry. Exp Fluids 29:103–116

Prasad A, Adrian R (1993) Stereoscopic particle image velocimetry applied to liquid flows. Exp Fluids 15:49–60

Press WH, Flannery BP, Teukolsky SA, Vetterling WT (1992) Numerical recipes in C: the art of scientific computing, 2nd edn. Cambridge University Press, Cambridge

Raffel M, Willert CE, Kompenhans J (1998) Particle image velocimetry: a practical guide. Springer, Berlin

Scarano F, David L, Bsibsi M, Calluaud D (2005) S-PIV comparative assessment: image dewarping + misalignment correction and pinhole + geometric back projection. Exp Fluids 39:257–266

Exp Fluids

Schroder A, Kompenhans J (2004) Investigation of a turbulent spot using multi-plane stereo particle image velocimetry. Exp Fluids 36:82–90

Soloff SM, Adrian RJ, Liu ZC (1997) Distortion compensation for generalized stereoscopic particle image velocimetry. Meas Sci Technol 8:1441–1454

Sørensen J, Christensen E (1995) Direct numerical simulation of rotating fluid-flow in a closed cylinder. Phys Fluids 7(4):764–778

Sørensen JN, Loc TP (1989) High-order axisymmetric Navier–Stokes code: description and evaluation of boundary conditions. Int J Num Methods Fluids 9:1517–1537

Spohn A, Mory M, Hopfinger E (1998) Experiments on vortex breakdown in a confined flow generated by rotating disk. J Fluid Mech 370:73–99

Thompson MC, Hourigan K (2003) The sensitivity of steady vortex breakdown bubbles in confined cylinder flows to rotating lid misalignment. J Fluid Mech 496:129–138

Vogel H (1968) Experimentelle ergebnisse über die laminare strömung in einem zylindrischen gehäuse mit darin rotierender scheibe. Bericht 6, Max–Planck-Institut für Strömungdforschung, Göttingen

Wieneke B (2005) Stereo-PIV using self-calibration on particle images. Exp Fluids 39:267–280

Willert C (1997) Stereoscopic digital particle image velocimetry for application in wind tunnel flows. Meas Sci Technol 8:1465–1479

Chapter 4

Volumetric PIV

4.1 Overview

While the previous chapter described a set of improvements to stereo PIV (which offers the advantage of a third velocity vector component), this chapter discusses a set of advances in PIV that share the aim of extending the dimensionality of PIV. Both papers in this chapter are based on PIV techniques that offer measurements over three dimensions, but utilising only a single perspective.
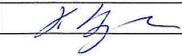
The chapter begins with a paper by Fouras et al (2007*b*), which represents the description of the second ever successful implementation of X-ray PIV. This work follows from a series of papers based on Lee and Kim (2003) and makes several significant advances over that work. These advances include the development of a correction process for the effects of volumetric illumination as provided by a X-ray light source, which resulted in significant errors in the original paper. The paper then demonstrates the development of a new correlation analysis algorithm, which under certain circumstances allows for the resolution of the full three-dimensional velocity vector field from a single perspective. The paper also describes how a fully three-dimensional velocity vector field may be calculated without the use of assumptions by means of multiple perspectives.

The chapter continues with a paper by Fouras et al (2008), which extends the concept of correlation analysis to yield a three-dimensional velocity vector field. This technique utilises the effect of focus in visible light imaging to allow the velocity to be resolved at each position in depth. This allows for a fully three-dimensional vector field without assumptions and without additional perspectives. This technique offers substantial advantages over other three-dimensional techniques, both in terms of information density (with no limit to the number of vectors per image) and simplicity of experimental set-up (with identical set-up to standard planar PIV). This paper has received extremely favourable reviews and it is expected to be accepted for publication in the near future.

4.2 Three-dimensional Synchrotron X-ray particle image velocimetry

The following paper was published in 2007 in *Journal of Applied Physics*. This work was co-authored by J. Dusting, R. Lewis and K. Hourigan, and is entitled *"Three-dimensional Synchrotron X-Ray Particle Image Velocimetry"*. The paper is reproduced in this thesis directly from the version published online.

Declaration

Declaration for manuscript included in PhD Thesis

Monash University

Declaration for Thesis Chapter 4.2

Declaration by candidate

In the case of Chapter 4.2, the nature and extent of my contribution to the work was the following:

Nature of contribution	Extent of contribution (%)
Initiated the paper, performed experiments, wrote analysis software, analysed data, wrote manuscript, revised manuscript.	60

The following co-authors contributed to the work. Co-authors who are students at Monash University must also indicate the extent of their contribution in percentage terms:

Name	Nature of contribution	Extent of contribution (%) for student co-authors only
Dr. J. Dusting	Performed experiments, analysed data, co-wrote manuscript	N.A.
Professor R. Lewis	Technical advice, advice on the manuscript	N.A.
Professor K. Hourigan	Co-wrote manuscript	N.A.

Candidate's Signature		Date 08 Nov 07

Declaration by co-authors

The undersigned hereby certify that:

(25) the above declaration correctly reflects the nature and extent of the candidate's contribution to this work, and the nature of the contribution of each of the co-authors.
(26) they meet the criteria for authorship in that they have participated in the conception, execution, or interpretation, of at least that part of the publication in their field of expertise;
(27) they take public responsibility for their part of the publication, except for the responsible author who accepts overall responsibility for the publication;
(28) there are no other authors of the publication according to these criteria;
(29) potential conflicts of interest have been disclosed to (a) granting bodies, (b) the editor or publisher of journals or other publications, and (c) the head of the responsible academic unit; and
(30) the original data are stored at the following location(s) and will be held for at least five years from the date indicated below:

Location(s)	Division of Biological Engineering, Monash University.

Signature 1		Date
Signature 2		
Signature 3		

Three-dimensional synchrotron x-ray particle image velocimetry

A. Fouras[a)]
Division of Biological Engineering, Monash University, P.O. Box 31, Melbourne 3800, Australia

J. Dusting
Department of Mechanical Engineering, Monash University, P.O. Box 31, Melbourne 3800, Australia

R. Lewis
Monash University Center for Synchrotron Science, Monash University, P.O. Box 27, Melbourne 3800, Australia

K. Hourigan
Division of Biological Engineering, Monash University, P.O. Box 31, Melbourne 3800, Australia

There is great potential to vastly improve biological flow measurement by using a combination of synchrotron imaging and the latest experimental flow measurement techniques. In the current paper, the three-dimensional velocity field within a cylindrical tube is measured using a combination of phase-contrast x-ray imaging and particle image velocimetry (PIV). We greatly refine the techniques previously used to undertake velocity measurements with a synchrotron light source, substantially enhancing accuracy. Furthermore a PIV correlation peak analysis is developed to allow three-dimensional measurement of the velocity field. © *2007 American Institute of Physics*. [DOI: 10.1063/1.2783978]

I. INTRODUCTION

The potential applications for three-dimensional flow resolution inside closed, opaque vessels are numerous and significant. For instance, the detailed measurement of flow fields within blood vessels would facilitate more advanced research into the role of hemodynamics in the development and potential treatment of cardiovascular disease. Diseased conditions of the vasculature such as stenosis and aneurysm are the continued focus of much research.[1,2] Techniques to measure the fluid dynamics properties of the blood flow through the effected vasculature with increased resolution and accuracy are key to developing treatments and understanding of these diseases.[3–6] Many current blood flow measurement techniques can only quantify peak systolic velocity, a single indicator of the average flow field. Fully three-dimensional (3D) velocity measurements would also yield a number of more useful flow parameters such as flow rate, wall shear, and turbulence levels. Other possible biomedical applications include the study of flow through optically opaque heart valves and artificial hearts, both of which are challenging flow geometries to evaluate.

The ability to resolve the instantaneous velocity field across a 3D volume is a highly desirable technology that has alluded fluid mechanics experimentalists. Three-dimensional holographic particle image velocimetry (PIV) has reportedly been used to measure instantaneous turbulent flow fields in three dimensions,[7] but this technique has several shortcomings. These include an immensely complex optical setup for data acquisition and reconstruction,[8] a very poor signal to noise ratio, and the inability to record a time sequence of velocity fields. Scanned, multiplane PIV (Ref. 9) or stereo-

scopic particle image velocimetry[10] (SPIV) can be used to compile 3D flow fields; however, scanning techniques require the data within each plane to be captured at different points in time and therefore necessitate the interrogated flow to be stationary in time.

It is problematic to measure flows within opaque vessels, such as blood vessels, using current technologies. Most common spatially resolved flow measurement techniques, such as PIV or SPIV, require clear optical access to the region of interest. Medical imaging techniques that have previously been used to measure flows *in vivo*, such as ultrasonography and magnetic resonance imaging (MRI), are generally restricted to velocity field measurements with spatial resolutions of millimeter precision.

X-ray imaging has also rarely been applied to flow measurement. Seeger *et al.*[11] tracked individual particles in a bubble column in 3D space using dual x-ray detector systems. In general, though, particle tracking velocimetry (PTV) leads to low levels of information being recorded as it relies on identification of individual tracers that must be present in low numbers, especially when used with volume illumination. Lee and Kim subsequently used PIV rather than PTV and achieved far more measurements.[12] PIV is a newer flow measurement technique than PTV, however, it is well established within the field of fluid mechanics. Importantly it has been shown to be capable of accurately measuring instantaneous velocity fields that have a high dynamic range. In PIV, regions of fluid containing multiple tracer particles are imaged at two points in time separated by a known time interval and processed using correlation software. This process produces correlation "peaks" at separate sampling window locations across the interrogation region, which are then converted into velocity vectors by assuming that the mode value

---

a)Electronic mail: fouras@eng.monash.edu

102, 064916-1

represents the average velocity within the window. As it is statistically based, PIV can work with poorer signal to noise ratios and higher particle numbers than PTV.

Using an x-ray light source to conduct PIV poses its own significant problems, especially due to the fact that the fluid region is volume illuminated. In PIV, the light source is ideally narrowed to a flat plane, meaning that only a single cross section of the flow is interrogated and any velocity variations in the out-of-plane (or z) direction are not recorded. As the light sheet is thickened, the velocity variation in z is included within the imaged region and contaminates the PIV signal. This is particularly serious for flows that are significantly variable in the out-of-plane direction, such as a pipe flow viewed from the side. As Lee and Kim[13] used a flow with a Poiseuille velocity profile, they were only capable of measuring pipe flow in a z-averaged sense. The problem of volume illumination is also currently endemic to micro-PIV.[14,15] The amount of information contaminating the flow from outside the desired imaging plane is a function of the depth of focus and is therefore mostly controlled by the numerical aperture of the microscope lens. This makes resolution of velocity data in the z direction from a volume-averaged cross-correlated particle field even more advantageous.

Synchrotron phase-contrast x-ray imaging is a powerful tool for anatomical measurement and offers much improved contrast over conventional imaging for biological tissues.[16,17]

In the current paper we develop a PIV correlation peak analysis combined with phase-contrast x-ray imaging to measure 3D velocity fields. Research in developing the technique exposes flaws in the way previous volume-averaged x-ray PIV has been undertaken.

II. 2D X-RAY PIV

PIV is a well established tool for measuring the displacement of tracer particles within a measurement plane.[18] The two-dimensional (2D) region imaged by a camera is typically illuminated over a limited depth by the use of a thin laser sheet, allowing the statistical (2D) measurement to be applicable to any region of flow that is approximately 2D. This process works by discretizing the 2D image into sampling windows and performing a cross-correlation analysis between the sampling windows of frames taken a short time interval (Δt) apart. The peak in the cross correlation typically represents the modal displacement inside the measurement volume over the time between exposures. The representative velocity inside that sampling window at that time is then simply the ratio of the displacement and the time separation.

Local variation in the peak is mainly due to the statistical certainty of noninteger displacements; interrogation of the local variation of the peak yields an estimate of subpixel component of the displacement.[19] The width of the signal peak is typically twice the length of the particle diameter. In the unusual case where there are large displacement gradients inside the imaging plane, the peak is smeared by these gradients. The common solution to this is to estimate the gradients and distort the image to deconvolve, or "unsmear," the peak against these distortions[20] improving the signal to noise ratio.
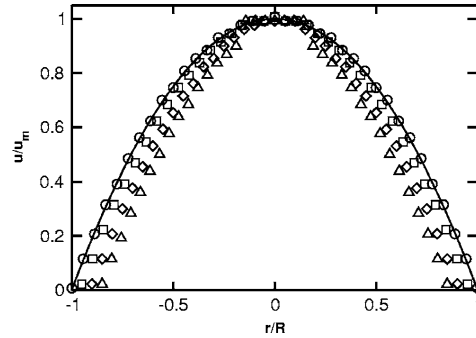

FIG. 1. Profiles calculated by taking the modal velocity inside discrete windows of a simulated 3D pipe flow data field. The different symbols represent different sampling window sizes. ○ symbols represent S/R $=10^{-3}$; □ symbols represent $S/R=0.05$; ◇ symbols represent $S/R=0.10$; and △ symbols represent $S/R=0.15$. For comparison, the exact maximum u profile is plotted as a solid line.

Lee and Kim,[13] have reported the 2D measurement of a duct flow using x-ray PIV. While the flow in the axial (x) and vertical (y) axes was presented, the flow in the out-of-plane direction (z) was not shown. However, any gradients in the z direction will certainly contribute to variation of the correlation peaks from which the 2D measurement was derived. Lee and Kim understood this and explained their substantial underestimation of the velocity field as being caused by the PIV measurement representing the mean velocity. However, PIV measures the modal, rather than the mean, velocity at each window location.

Figure 1 shows computer modeling of the modal velocity at spanwise locations across a cylindrical tube at low Reynolds numbers (Re). The Reynolds number represents the ratio of momentum and viscous fluid forces and is calculated as $\mathrm{Re}=uD/v$ where u is the velocity, D is the pipe diameter, and v is the kinematic viscocity of the fluid. The velocity in the radial and azimuthal directions is assumed to be 0, while the axial flow, given by velocity u, is assumed to be parabolic in nature. That is,

$$u/u_m = 1 - r^2/R^2, \qquad (1)$$

where u_m is the maximum axial velocity, r is the radial position from the tube axis of symmetry, and R is the total radius of the tube. For the simulation, a representative circular cross section of the pipe flow was discretized into 5000 $\times$ 5000 points, which were then used to develop histograms. The modal values within discrete windows of varying size S are plotted in Fig. 1 as a function of the window midpoint location in the r direction. For this flow configuration, the modal velocity is very nearly equal to the maximum velocity, with any difference caused by the finite histogram bin size. The underestimation visible at the edges of the figure is a function of the finite size of the window. This effect increases as the relative window size increases. Lee and Kim were subject to a similar underestimation phenomenon in their data, but attributed it to the sinking of tracer particles near the wall. However, the terminal velocity of relatively
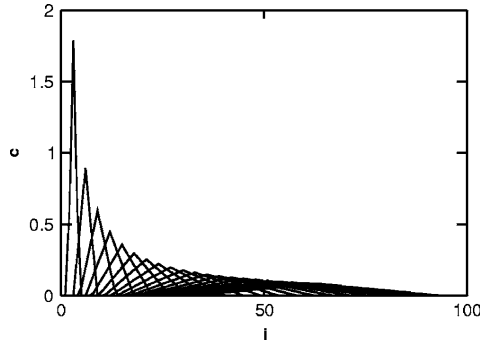
FIG. 2. Sequence of functions (c) depicting convolution matrix C as a function of displacement component i. Note that the area under each triangle is constant. The experiments conducted as part of this study have ϵ_τ =0.495.
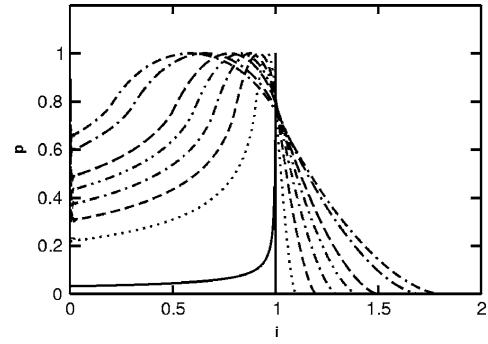
FIG. 3. Theoretical peak constructed from the PDF of center line Poiseuille circular pipe flow, with peaks convolved by convolution functions constructed with ϵ_τ varying from 0.1 to 0.7. In each case the peak magnitude p is plotted as a function of displacement component i. The solid line represents the theoretical peak, $\cdots$ represents ϵ_τ=0.1, $---$ represents ϵ_τ=0.2, $-\cdots$ represents ϵ_τ=0.3, $-\cdots$ represents ϵ_τ=0.4, —— represents ϵ_τ=0.5, —·— represents ϵ_τ=0.6, and ·— ·— represents ϵ_τ=0.7.

heavy particles would not be more significant near the wall than at the center, and the underestimation in their data is more likely due to the finite window size effect.

The underestimation of peak velocity for finite window sizes is, in fact, related to a completely different phenomenon than sinking tracer particles. Typically PIV is performed using pulsed lasers. These lasers deliver a moderate amount of light energy in an extremely short period of time, characteristically a few nanoseconds. This means that the exposure time (effectively the pulse duration for a pulsed light source) is very short compared to the time between exposures. However, when performing x-ray PIV with a synchrotron light source, particle images will be smeared by the motion captured by the psuedocontinuous illumination. This smears the correlation peaks in a manner proportional to the particle velocity. As there are multiple velocities present within each window, the smearing of the correlation peaks becomes complex.

In the technique developed here, each velocity component is considered separately and convolved by a function that is itself a function of the velocity. These functions are easily derived with an analytical consideration of the cross correlation of top-hat functions. The length of the top-hat function is given by the product of the velocity (u) and exposure time, and the displacement is given by the product of u and Δt. These equations can be conveniently nondimensionalized by the use of the term ϵ_τ, the ratio of the exposure time to Δt.

Each smeared particle image can be approximated by a top-hat function. The cross-correlation peak of two top-hat functions is triangular, and since each volumetric region contributes equally to the peak, the area under each triangle is fixed. The higher the velocity, the longer the top hat, and the longer and therefore lower the triangle. As an illustration of this concept, Fig. 2 shows a number of the functions $c(i,j)$ that make up the convolution matrix C. As the displacement increases, the response becomes broader, with a lower maximum value. When a range of displacement components is

present, this results in a bias toward the lower displacement components, and hence a potential underestimation of velocity.

Figure 3 shows how a theoretical peak, which also represents a probability density function of displacement, is smeared by the convolution functions with varying ϵ_τ. A shift of the peak toward zero caused by the convolution process is clearly visible. This shift is approximately proportional to ϵ_τ, the ratio of exposure time t_e, and time between exposures Δt. Figure 4 demonstrates the extent to which the peak value moves as a function of ϵ_τ. It is evident that the process is nearly linear.

Since we know that the peak shifting effect is approximately linear with ϵ_τ, we can establish a new technique for its removal. This involves solving for the velocity field twice and then using a technique similar to Richardson's extrapolation to solve for the correct velocity. The two estimates for the velocity are obtained by using two distinct time intervals
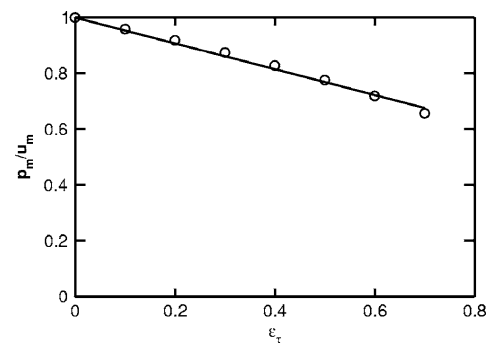
FIG. 4. Relative i position maximum value of peak as a function of ϵ_τ for Poiseuille circular pipe flow. A regression line is also included to demonstrate the extent to which the phenomenon is linear.
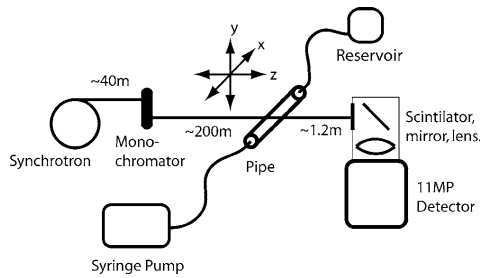
FIG. 5. Schematic of the synchrotron x-ray PIV and pipe flow system, as well as the coordinate system.

FIG. 6. Measured two-dimensional velocity vector field prior to peak analysis. For clarity, only the upper half of the vessel and every fourth vector are shown. The actual resolution is 59×37 vectors.

over which to perform the PIV process. For the current study we used frame intervals of 1 and 2 frames. This means that the PIV process was integrated between frames 1 and 2, 2 and 3, and so on for an interval of 1, and between 1 and 3 and 2 and 4, and so on for a frame interval of 2.

Mathematically, the solution to the problem can be expressed as in Eq. (2), where k is a constant specific to the velocity profile. This equation shows that by extrapolating between the two estimates of displacement, Δx_1 and Δx_2, a velocity estimate (Δx) without an ϵ_τ error term can be evaluated.

$$\Delta x_1 = u\Delta t + kt_e/\Delta t,$$

$$\Delta x_2 = 2[u\Delta t + kt_e/(2\Delta t)],$$

$$\Delta x = u\Delta t = \Delta x_2 - \Delta x_1. \tag{2}$$

This technique is simple to implement and means that in future x-ray PIV practitioners will be able to achieve simple two-dimensional measurements with a synchrotron light source. The authors have completed this analysis for the flow in a round pipe at $\mathrm{Re} \approx 10^{-4}$. This flow was achieved in a 15 mm diameter pipe filled with glycerin containing silver coated hollow glass microspheres (Potters Industries). The glycerin was pumped through the pipe using a syringe pump.

The experiments were conducted at the Spring8 synchrotron with the approval of the Japan Synchrotron Radiation Research Institute (JASRI). The experiments were conducted on the biomedical beam-line(20B2) with a 25 keV x-ray beam that was approximately 25 mm in height and 40 mm in width. The images were acquired with a Hamamatsu beam monitor (BM4) with 4000×2642 pixels and a pixel size of 5.87 μm. The exposures used were 2940 ms and the exposure delay was 5940 ms (ϵ_τ=0.495). Figure 5 shows the basic layout of the experiment and coordinate system.

Figure 6 shows a portion of the measured 2D velocity field presented for clarity at reduced resolution. Those familiar with PIV will recognize the spatial resolution of the flow displayed in a 2D sense. Since the beam is parallel and the flow is steady, we expect to see no variation of the flow in the x (streamwise) direction. The flow qualitatively agrees with the theoretical flow of Eq. (1). As expected, little or no variation in x is visible and a variation from very low flow at the wall to peak flow at the center line can be seen.
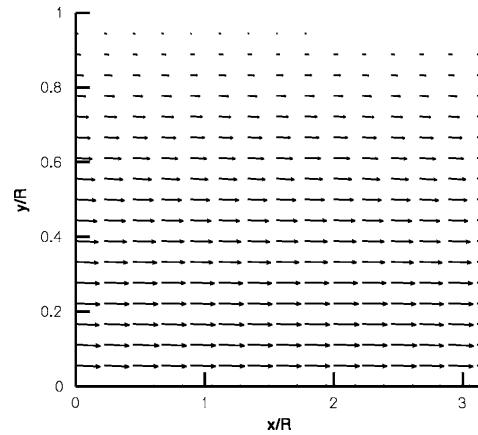
For a more quantitative evaluation of the technique, the calculated maximum flow profile is compared to the measured profile in Fig. 7. For completeness, measured profiles from the two estimates used to calculate the actual velocity are also shown. The excellent agreement between the measured maximum velocity and the theoretical value is clear. As described above, the slight underestimation near the walls is to be expected.

III. DECONVOLUTION OF PEAK SMEARING

By interrogating the correlation peak, further information can be extracted relating to the velocity gradients in the measurement volume of each window. As mentioned above, the relatively long exposure times required for synchrotron imaging smear the correlation peak, causing distortion of ve-
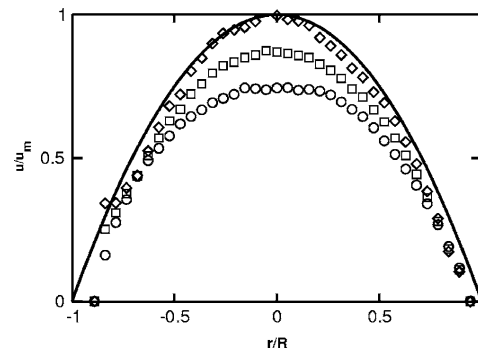

FIG. 7. Measured average velocity profile based on different cross-correlation peaks: $\bigcirc$ symbols represent velocities achieved using Δx_1; $\square$ symbols represent velocities achieved using $\Delta x_2/2$; and $\diamond$ symbols represent velocities achieved using Δx. For comparison, the theoretical u profile is plotted as a solid line.
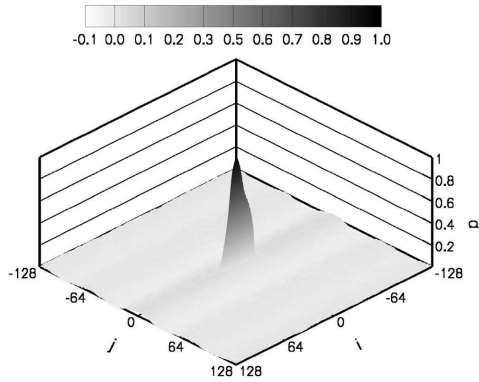
FIG. 8. Average measured two-dimensional cross-correlation peak p_1 corresponding to $y/R=0$, plotted as a function of displacement components i and j. Both the vertical axis and the shading represent the local p magnitude.

FIG. 10. i cross section of the average measured cross-correlation peaks at $y/R=0$: $2p_1$ ($\bigcirc$), p_2 ($\square$), and extrapolated peak $2p_e$ ($\diamond$).

locity information and underestimation of peak velocity. Before we can further interrogate the correlation peak, we must first deconvolve the smearing effects to discover the equivalent peak that would result from an instantaneous exposure.

Figure 8 shows p_1, the spatial average of the correlation peaks calculated as part of the evaluation of Δx_1, as a function of the discrete displacement components i and j. In this case, i and j are aligned in the x and y directions, respectively. As shown in Fig. 8, the peak is a thin (two particle diameters wide) linear feature since the velocity gradient is one dimensional. To simplify the analysis, the information in this peak is linearized along the i axis and then, once extracted, displayed as a line plot as in Fig. 9.

Once the data contained in the peak can be visualized in a linear fashion, an extrapolation process to derive the correct peak shape can be easily demonstrated. For this process, we use two peaks, p_1 and p_2, where p_1 results from the analysis of consecutive frames (i.e., 1–2, 2–3, 3–4,…,), and p_2 results from the analysis of every second frame (i.e., 1–3, 2–4, 3–5,…). In a similar manner as one could extrapolate
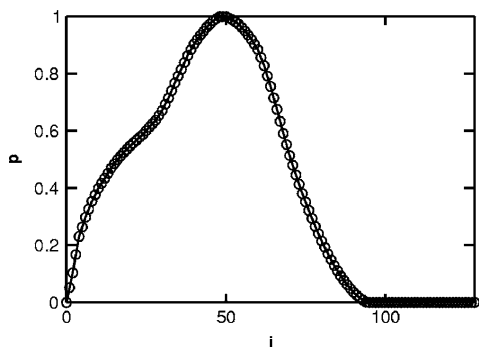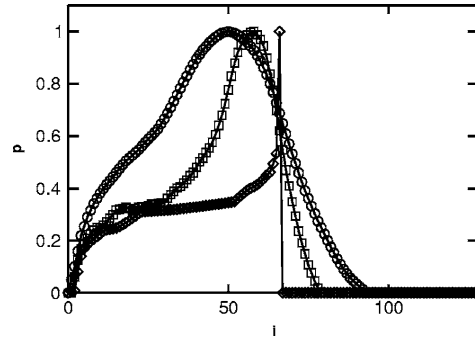
from $\Delta x_1, \Delta x_2$ to Δx, we can extrapolate from p_1, p_2 to the extrapolated peak p_e. The linearized plots of $2p_1$, p_2, and $2p_e$ are shown in Fig. 10. The extrapolated peak can be expressed as

$$\delta_e = \delta_2 - \delta_1, \tag{3}$$

where the variable δ represents the i (or displacement coordinate) of a normalized value of the peak. The extrapolated peak shown in Fig. 10 clearly has the same general shape as the theoretical peak shown in Fig. 3.

Now that the correct correlation peak can be reconstructed from Richardson's extrapolation process, it is possible to interrogate the peak to obtain 3D velocity information within the sampling window.

IV. 3D RECONSTRUCTION

As stated previously, each particle contributes to the correlation peak in a position corresponding to its velocity by an amount equal to the intensity of its image. With x-ray imaging there are no depth of focus effects, meaning that every particle contributes equally to the correlation peak. Furthermore, since we can assume in this case that the particle seeding density is equal throughout the volume, we can also assume that the entire flow measurement volume is equally represented in the correlation peak.

We can therefore assert that the correlation peak p_e represents a probability density function (PDF) of the velocity within the measurement volume. This is theoretically as far as the true measurement of the flow can be taken. However, if we can make further assumptions about the flow, then the PDF implies the complete velocity profile. For this particular case, two reasonable assumptions can be made about the flow.

First, we assume that flow near the center line is always greater than flow near the wall. At low and moderate Reynolds numbers, no instability which would violate this assumption will exist. Second, we assume that the flow is symmetric about the plane $z=0$. Given that at each (x,y) location, the same velocity will occur at two z locations, this assumption is necessary unless additional information can be
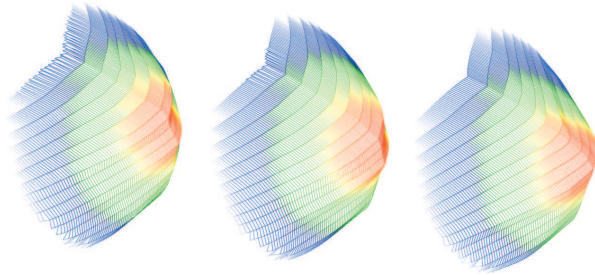

FIG. 9. i cross section of the average measured cross-correlation peak p_1 corresponding to $y/R=0$.

FIG. 11. (Color) Reconstructed three-dimensional velocity field inside a round pipe at a Reynolds number of 10^{-4}. Every node on the mesh corresponds to a different measured value. The colored contours represent the magnitude of u.

provided. The extrema of the z coordinates as a function of x and y are given by $z_m = \pm\sqrt{(R^2 - y^2)}$ as we are using a pipe of fixed radius.

It is now simple to convert the volumetric PDF of the velocity to a velocity profile. We start with the boundary condition corresponding to either the minimum or maximum velocity and integrate along the known displacement values and solve for the z value that matches each displacement. As stated above, in this case we start at $z=0$ for the maximum velocity and at $z=-z_m$ for the minimum velocity,

$$z(u) = z_e \left[1 - \frac{\int_{-\infty}^{u} p(i)di}{\int_{-\infty}^{\infty} p(i)di} \right]. \tag{4}$$

By using the above approach the velocity profile was calculated at each (x, y, z) position inside the pipe over a sequence of 40 frame pairs. These velocities were averaged over time and then plotted as a function of y and z at three different x locations, as shown in Fig. 11. The velocity field cross section is close to the expected Poiseuille profile, with little variation in profile at the different x locations. The colored contour shading included in Fig. 11 helps us illustrate this similarity.

V. CONCLUSIONS

In this paper the viability of x-ray PIV has been further demonstrated. Furthermore we have highlighted several flaws in the approach of investigators who have previously used x-ray PIV to measure 2D velocity vector fields of flows that vary over z.

We have demonstrated a useful technique for extrapolating correct 2D vector fields and correlation peaks. This allows not only accurate measurement of 2D vector fields but also interrogation of correlation peaks corresponding to velocity probability distribution in the z direction.

Under certain circumstances, this PDF can be used to infer the velocity profile over z. In this case, Poiseuille flow through a pipe has been measured in a 3D sense.

The authors anticipate that in the future similar measurements can be made with fewer or no assumptions about the nature of the flow, by extracting additional information during image acquisition. The most likely method for gaining this information would be through the measurement of the flow volume from multiple perspectives. This technique would combine the advantages of both SPIV and x-ray computed tomography.

[1]R. Ross, Nature (London) **362**, 801 (1993).
[2]J. Radermacher *et al.*, N. Engl. J. Med. **344**, 410 (2001).
[3]J. E. Moore, C. Xu, S. Glagov, C. K. Zarins, and D. N. Ku, Atherosclerosis **110**, 225 (1994).
[4]A. S. Anayiotos, S. A. Jones, D. P. Giddens, S. Glagov, and C. K. Zarins, J. Biomech. Eng. **116**, 98 (1994).
[5]X. He and D. N. Ku, J. Biomech. Eng. **118**, 74 (1996).
[6]D. N. Ku and D. P. Giddens, J. Biomech. **20**, 407 (1987).
[7]J. Zhang, B. Tao, and J. Katz, Exp. Fluids **23**, 373 (1997).
[8]Y. Pu and H. Meng, Exp. Fluids **29**, 184 (2000).
[9]C. Brucker, Meas. Sci. Technol. **8**, 1480 (1997).
[10]T. Hori and J. Sakakibara, Meas. Sci. Technol. **15**, 1067 (2004).
[11]A. Seeger, K. Affeld, L. Goubergrits, U. Kertzscher, and E. Wellnhofer, Exp. Fluids **31**, 193 (2001).
[12]S.-J. Lee and G.-B. Kim, J. Appl. Phys. **94**, 3620 (2003).
[13]S.-J. Lee and G.-B. Kim, J. Appl. Phys. **97**, 064701 (2005).
[14]C. D. Meinhart, S. T. Wereley, and M. H. B. Gray, Meas. Sci. Technol. **11**, 809 (2000).
[15]M. G. Olsen and R. J. Adrian, Exp. Fluids **29**, S166 (2000).
[16]R. A. Lewis, Phys. Med. Biol. **49**, 3573 (2004).
[17]R. A. Lewis , N. Yagi, M. J. Kitchen, M. J. Morgan, D. Paganin, K. K. W. Siu, K. Pavlov, I. Williams, K. Uesugi, M. J. Wallace, C. J. Hall, J. Whitley, and S. B.Hooper, Phys. Med. Biol. **50**, 5031 (2005).
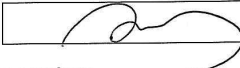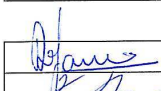[18]R. J. Adrian, Annu. Rev. Fluid Mech. **23**, 261 (1991).
[19]C. Willert and M. Gharib, Exp. Fluids **10**, 183 (1991).
[20]H. Huang, H. E. Fiedler, and J. J. Wang, Exp. Fluids **15**, 263 (1993).

4.3 Volumetric Correlation PIV: a New Technique for 3D Velocity Vector Field Measurement

The following paper was submitted in 2007 to *Experiments in Fluids*. This work was co-authored by D. Lo Jacono and K. Hourigan, and is entitled *"Volumetric Correlation PIV: a New Technique for 3D Velocity Vector Field Measurement"*. The paper is reproduced in this thesis directly from the version submitted to the editor for review.

Declaration

Declaration for manuscript included in PhD Thesis

Monash University

Declaration for Thesis Chapter 4.3

Declaration by candidate

In the case of Chapter 4.3, the nature and extent of my contribution to the work was the following:

Nature of contribution	Extent of contribution (%)
Initiated the paper, performed experiments, wrote analysis software, analysed data, wrote manuscript, revised manuscript.	60

The following co-authors contributed to the work. Co-authors who are students at Monash University must also indicate the extent of their contribution in percentage terms:

Name	Nature of contribution	Extent of contribution (%) for student co-authors only
Dr D. LoJacono	Performed experiments, analysed data, co-wrote manuscript	N.A.
Professor K. Hourigan	Co-wrote manuscript	N.A.

Candidate's Signature		Date 08 NOV 07

Declaration by co-authors

The undersigned hereby certify that:

(31) the above declaration correctly reflects the nature and extent of the candidate's contribution to this work, and the nature of the contribution of each of the co-authors.
(32) they meet the criteria for authorship in that they have participated in the conception, execution, or interpretation, of at least that part of the publication in their field of expertise;
(33) they take public responsibility for their part of the publication, except for the responsible author who accepts overall responsibility for the publication;
(34) there are no other authors of the publication according to these criteria;
(35) potential conflicts of interest have been disclosed to (a) granting bodies, (b) the editor or publisher of journals or other publications, and (c) the head of the responsible academic unit; and
(36) the original data are stored at the following location(s) and will be held for at least five years from the date indicated below:

Location(s)	Division of Biological Engineering, Monash University.

Signature 1		Date
Signature 2		

Andreas Fouras, David Lo Jacono and Kerry Hourigan

Volumetric Correlation PIV: a New Technique for 3D Velocity Vector Field Measurement.

Abstract A method is proposed that allows three-dimensional (3D) two-component measurements to be made in any volume illuminated by a light sheet of finite thickness by means of particle image velocimetry (PIV). The method is based on decomposing the cross-correlation function into various contributions at different depths in the light sheet. Because the technique is based on 3D decomposition of the correlation function and not reconstruction of particle images, there is no limit to particle seeding density as experienced by 3D particle tracking algorithms such as defocusing PIV, in-line holographic PIV and tomographic PIV. Correlations from different depths are differentiated by the variation in point spread function of the lens used to image the measurement volume over that range of depths. A number of examples are demonstrated by use of synthetic images which simulate micro-PIV (μPIV) experiments. These examples vary from the trivial case of Couette flow (linear variation of one velocity component over depth) to a general case where both velocity components vary by different complex functions over the depth. The paper also discusses using this method with thick light sheets in macro-scale PIV and in a stereo configuration for 3D three-component PIV.

A. Fouras, D. Lo Jacono, K. Hourigan

Fluids Laboratory for Aeronautical and Industrial Research (FLAIR)

Department of Mechanical Engineering, PO Box 31, Monash University, Clayton, 3800, Australia

Tel.: +61-3-99053959

Fax: +61-3-99051825

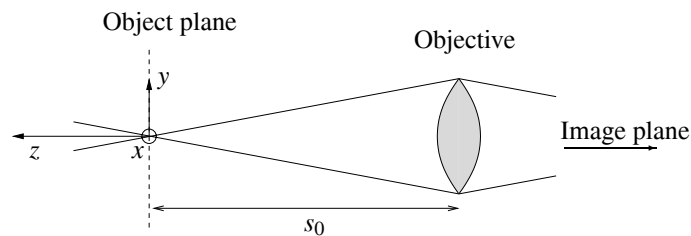E-mail: fouras@eng.monash.edu.au

68

2

Fig. 1 Schematic diagram of generic apparatus including coordinate system. The object plane (also the focal plane) is at the distance s_0 from the objective. The origin of the coordinates is the center of the object plane.

Keywords Volumetric Particle Image Velocimetry, PIV, 3D correlation analysis, micro-PIV

1 Background

Since its general acceptance as a powerful measurement tool for fluid mechanics, researchers have been searching for means of increasing the dimensionality of PIV above the standard two component velocity measurement over a plane. Throughout the paper the mDnC notation will be used, where m represents the dimension of the measurement volume and n represents the dimension of the resolved displacements. As an example, two component velocity measurements over a plane are expressed 2D2C measurements in this notation.

For three components of velocity vectors over a measurement plane, stereo PIV (SPIV) was one of the first variations in PIV methodology to be introduced. Since its first development (Arroyo and Greated, 1991) through to more recent advances (Fouras et al, 2007a,b), SPIV has been becoming better understood, more accurate and simpler to implement. With 2D3C systems, six of the nine terms of the velocity gradient tensor are available. In order to obtain all nine terms of the velocity gradient tensor, a pseudo 3D3C system is available by conducting SPIV on two adjacent planes. Multi-plane SPIV (Schroder and Kompenhans, 2004; Kahler, 2004) allows for differentiation across planes to obtain those additional three spatial velocity gradients.

Holographic PIV (HPIV) (Barnhart et al, 1994; Zhang et al, 1997) allows for truly 3D3C velocity measurements. This broad range of techniques has, in its various forms, advantages and disadvantages. In-line HPIV, and more recently available Digital In-line HPIV, is perhaps the simplest and easiest to implement, but is limited by signal to noise ratio (SNR). Furthermore, a limited number of particles that can be resolved

3

and therefore limited number of vectors is achievable. Off-axis HPIV, which does not have this limitation, is dramatically more complex to implement and requires considerable greater laser power. Although HPIV has demonstrated ability to accurately resolve 3D3C velocity fields, due to complexity and expense of implementation, HPIV has not enjoyed wide popularity.

A different approach to that of Holography is Tomographic image reconstruction. Tomographic PIV (Elsinga et al, 2006) utilises multiple cameras in different positions to image an illuminated volume. A 3D image pair is reconstructed and 3D cross-correlation analysis is performed. This technique, although recent, shows promise as an alternative 3D3C measurement tool. Unfortunately, like other techniques that reconstruct the image rather than the velocity field, this approach is also limited in the number of particles that can be resolved.

A simpler to implement, elegant technique that achieves 3D3C results is defocusing PIV (Willert and Gharib, 1992; Pereira et al, 2000). This technique utilises a lens mask to alter the point spread function (PSF) of the imaging system. The mask creates a PSF that is asymmetric about the focal plane. Particles out of focus appear as triangles, which invert as they cross the focal plane. This technique allows particles to be tracked throughout the illuminated volume, producing 3D3C particle tracking velocimetry (PTV). However, as a PTV variant, this technique is necessarily limited in the number of particles that can be individually identified. Furthermore, the introduction of the lens mask substantially reduces the light gathering power of the imaging system. Despite these limitations, the technique is gaining popularity and has achieved some considerable success recently (Forouhar et al, 2006). Another development similar to defocusing PIV is based on deconvolution imaging (Park and Kihm, 2006). This once again allows the direct identification and measurement of particles in 3D space allowing 3D3C PTV.

As discussed above, many techniques are available that have successfully resolved 3D3C vector fields. However, these techniques are typically based on the reconstruction of particle images, followed by either 3D cross-correlation or particle tracking analysis, which limits maximum spatial resolution. Furthermore, these techniques require additional or modified hardware not required for traditional PIV. This paper proposes a novel approach to gaining three-dimensional velocity vector fields without this spatial resolution limitation. The key principle is to conduct further analysis of the calculated correlation function, of single camera PIV images, to obtain the three-dimensional information. This results in a system that is identical to traditional

4

PIV implementations, differing only in the analysis of images post-acquisition. The technique is based on 3D decomposition of the correlation function into various contributions at different depths.

2 Introduction

It is well understood that particle images appear differently when they are not on the focal plane. Olsen and Adrian (2000b) discuss the effect of these out-of-focus particles on the measurement of the velocity field. In micro-PIV (μPIV) systems, the entire volume is illuminated. Therefore several aspects of an out-of-focus particle contribute to the velocity measurements, such as the variation in particle image intensity and diameter as a function of distance from the focal plane. A schematic diagram of the optical and geometrical parameters including the coordinate system is shown in Fig. 1. For a given particle diameter d_p and a given set of magnification M, focal number $f^{\#}$ and lens aperture diameter D_a, Olsen and Adrian (2000b) derived the expression of the effective diameter and the intensity distribution of that given particle as a function of depth as seen in the image plane:

$$d_e(z)^2 = M^2 d_p^2 + 5.95(M+1)^2 \lambda^2 f^{\#2} + \frac{M^2 z^2 D_a^2}{(s_0 + z)^2}, \tag{1}$$

$$I(r,z) = I_0 \exp\left(\frac{-4\beta^2 r^2}{d_e^2}\right), \tag{2}$$

with

$$I_0 = \frac{J_p D_a^2 \beta^2}{4\pi d_e^2 (s_0 + z)^2}, \tag{3}$$

where λ is the wavelength of the laser, J_p the flux of light emitted from the particle and $\beta^2 = 3.67$ (Adrian and Yao, 1985). The key assumptions are uniform particle diameter and laser intensity, isotropic light emission and that both the geometric optics term and the diffraction term can be approximated as Gaussian. To illustrate this, Eqs. (1) and (2) are represented in Fig. 2, for $M = 5$, $f^{\#} = 1$, $d_p = 0.5$ μm, and $D_a = 9000$ μm. The effect of out-of-focus particles is shown also in Fig. 3. Figure 3 shows the increase of the effective particle diameter and decrease of the peak light intensity emitted as the distance between the particle and the object plane (or focal plane) increases.

Of interest, Meinhart et al (2000a) and Olsen and Adrian (2000b) introduced the depth of correlation parameter. It defines the depth over which particles significantly contribute to the correlation function $2z_{\text{corr}}$for
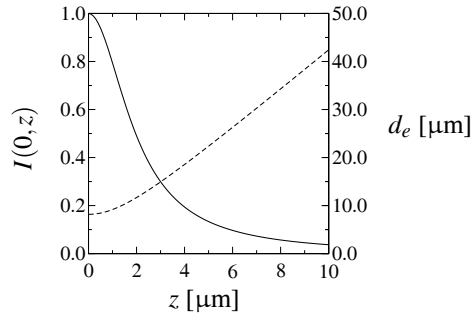
5

Fig. 2 Particle image intensity, $I(0,z)$, and effective diameter as a function of depth, distance from focal plane z, following Eqs. (1) and (2), represented by the solid and dashed line, respectively (Olsen and Adrian, 2000b)
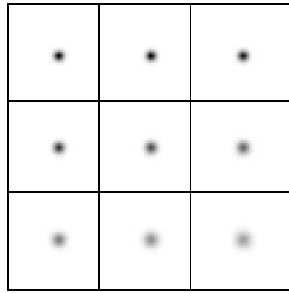

Fig. 3 Example of particle images at nine different depth from the focal plane, with depth increasing from left to right, top to bottom.

"simple flowfields". This relation must be modified if the flowfield contains either significant Brownian motion (Olsen and Adrian, 2000a) or out-of-plane motion (Olsen and Bourdon, 2003). Here, z_{corr} is given by:

$$z_{\mathrm{corr}} = \left[\frac{1-\sqrt{\varepsilon}}{\sqrt{\varepsilon}} \left(f^{\#2} d_p(z)^2 + \frac{5.95(M+1)^2 \lambda^2 f^{\#4}}{M^2} \right) \right]^2, \tag{4}$$

where ε is the ratio of the correlation contribution of a particle of $z = 0$ to the correlation contribution at z. Typically, the choice of $\varepsilon = 0.01$ is reasonable (Olsen and Adrian, 2000b). It is important to note that for cases where the PSF does not match aforementioned Eq. (1) and Eq. (2), it has been shown (Bourdon et al, 2004) that the PSF can be readily measured experimentally.

6

It had previously been thought (Meinhart et al, 2000a; Olsen and Adrian, 2000b) that the major problem in

μPIV is that the out-of-focus particles in as far as they contribute to the correlations produce bias. Therefore,

several attempts have been made to overcome these difficulties by filtering, subtracting, and then tracking

these particles. It is proposed here that the additional information provided by these out-of-focus particles

should not be discarded. Instead, it provides the opportunity to resolve the displacement as a function of

depth.

3 Description of New Technique

This proposed technique is based on the proposition that at any (x, y) location, the full cross-correlation

function C_{full} of the image pairs at that location is equal to the sum of cross-correlation functions at each

depth, C_{2D}, each with its own δ_x, δ_y and PSF. This can be expressed as:

$$C_{\text{2D}}(\hat{x}, \hat{y}, z) = \alpha I_0(z) \exp\left(-\frac{\|\hat{\underline{x}} - \underline{\delta}\|^2}{2\sigma(z)}\right), \tag{5}$$

$$C_{\text{full}}(\hat{x}, \hat{y}) = \alpha \sum_{z=z_{\text{min}}}^{z_{\text{max}}} C_{\text{2D}}(\hat{x}, \hat{y}, z), \tag{6}$$

where $\sigma = M d_e$ is the effective particle diameter in the image plane measured in pixels, and z_{min} and z_{max} are

the boundaries of the illuminated particle field.

To assist in the further description of the technique, the Couette flow is considered; that is, a uniform

shear through a channel of depth h. Synthetic image pairs of particles (at a given δt) within the whole channel

have been generated, using the Eqs. (1, 2). The synthetic image pairs are then cross-correlated to yield the

cross-correlation function. Figure 4 shows the measured cross-correlation function, C_{meas}, obtained for this

flow viewed at a $45°$ angle. The coordinates in the cross-correlation space are $\hat{x}$ and $\hat{y}$. It can be seen that the

pattern is not representative of a Gaussian distribution, as one would expect from cross-correlation of focused

particles, but is stretched along λ, the direction of the flow. Therefore, the pattern populates *all* the velocities

occurring in the illuminated field. It is clear that if one were to take the maximum of the peak— as is done in

classical PIV —the displacement obtained would be a complex function of both the velocity profile and the

PSF. This justifies previous attempts of narrowing the depth of field in order to minimised this bias.

In the case of Couette flow, or any other unidirectional flow, the λ coordinate can be trivially expressed

with $(\hat{x}, \hat{y})$. The aim as stated earlier in the section is to find a $\underline{\delta}(z)$ such that $C_{\text{full}}(\hat{x}, \hat{y})$ approaches $C_{\text{meas}}(\hat{x}, \hat{y})$.
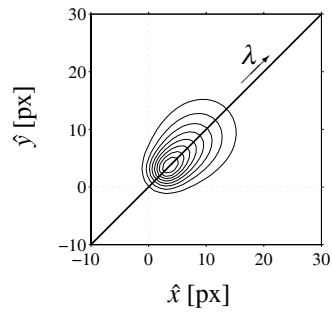
7

Fig. 4 An averaged cross-correlation function for a Couette flow. The curvilinear coordinate λ represents the relationship between $\hat{x}$ and $\hat{y}$ —the direction of the flow. Note that for this flow λ lies on the maximum envelope of the cross-correlation peak.

This approach is only valid while I_0 and d_e are unique for all z in the measurement volume. This uniqueness is achieved by placing the focal plane outside the measurement volume. The ideal case is to utilise the linear region of the $I_0(z)$ and $d_e(z)$ functions. However the maximum intensities of particles far from the focal plane also need to be considered in combination with the bit depth of the acquisition system.

This solution is implemented via a non-linear least squares solver. To achieve this, it is most convenient to express the solution $\delta_x(z)$ and $\delta_y(z)$ as continuous analytical functions. The choice of these functions is arbitrary but selected here are the piece-wise linear and cubic spline functions.

4 Results and discussion

A uniform channel geometry, depth $h = 6$ μm, has been used to validate this technique. Four different flow profiles have been selected, namely a Couette flow (linear in z); Poiseuille flow (parabolic in z); separated channel flow (cubic in z); mixing-layer flow profile (tanh in z). Finally, a generalisation of the technique is proposed via a skewed (general) boundary layer profile.

4.1 Validation

For the sake of simplicity of explanation, these four seminal cases have been implemented with $\delta_y = 0$. In cases such as these, where λ is a straight line (δ_x and δ_y are linearly related), the solution is independent of
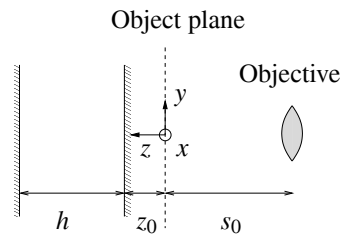
8

Fig. 5 Schematic diagram of the channel (depth h) including coordinate system. The object plane (also the focal plane) is at the distance s_0 from the objective, and at distance z_0 from the channel. The origin of the coordinates is the center of the object plane. The principal flow direction is out of the page.

the orientation of λ. In this circumstance, λ lies on the maximum envelope of the cross-correlation function and hence is easily found. Figure 5 shows a schematic of the geometrical configuration used as well as the coordinate system. Synthetic image pairs have been generated for particles of diameter $d_p = 0.5$ μm magnification, $M = 5$, focal number $f^{\#} = 1$ and aperture diameter $D_a = 9\,000$ μm, typical of a μPIV setup. Similar results have been obtained for other μPIV optical configurations. The particles were located over the entire channel depth. As discussed earlier, to achieve optimal conditions for linearity without exceeding depth of correlation, a measurement volume spanning from $z_0 = 2$ μm to 8 μm was chosen. These pairs were successively cross-correlated then averaged and normalised. As pointed out by Meinhart et al (2000b), averaging the cross-correlation samples overcomes problems such as insufficient seeding density and poor signal to noise ratio. Unless otherwise specified, the number samples used for each average in this study is 1 024.

Figure 6 shows the results of the analysis for the test cases described above. It can be seen that in all cases the solution has successfully captured the flow over the entire depth. Furthermore, these calculated velocities are obtained with a zero initial guess. The computational time and accuracy are improved if the practitioner has *a priori* knowledge of the flow. However in the case where such knowledge is not available, and for complicated topologies, the spline can be supplemented with a piece-wise linear approach as a first step, as exemplified in Fig 6(c) for the separated flow.

Interestingly the accuracy does not vary with the magnitude of shear, as illustrated by the increasing rates of shear from Figs. 6(a)-(d).
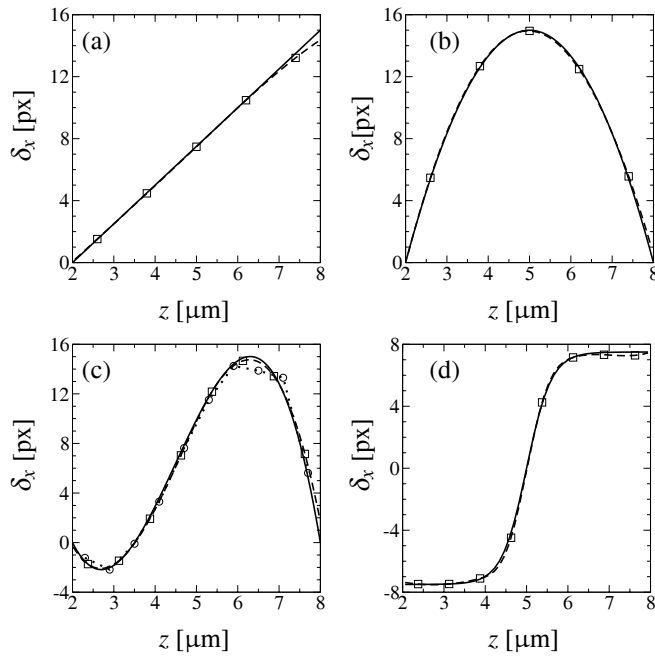
9

Fig. 6 Calculated values of the displacement δ_x as a function of depth for (a) Couette; (b) Poiseuille; (c) separated; (d) mixing layer. The solid line represents the exact solution. Squares represent the knots for the spline solution (dashed lines). The separated flow example illustrates the iterative approach consisting of first a linear guess (circles and dotted line) followed by a spline scheme.

Finally the authors wish to stress that all of the above examples relate to the volumetric correlation analysis of cross-correlation peaks at a single interrogation window location. These depth resolved measurements would be available at each sampling window location throughout a PIV measurement region.

Figure 7 shows both the effect of the number of samples N of the PIV interrogation window and the effect of the particle seeding density ρ on the accuracy of the calculated solution (σ). Clearly, increasing the number of samples increases the accuracy of the resolved displacement field. However, even for low number of sample ($N = 16$), the results qualitatively follow the exact solution. Furthermore, it can be seen that for low N the velocity profiles is biased towards the focal plane. The effect of seeding density follows an interesting trend,
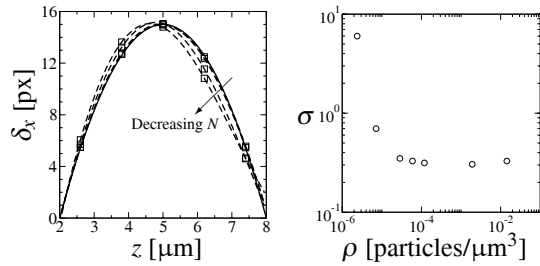
10

Fig. 7 Left: Effect on δ_x of the number of samples N of the PIV interrogation window; $N = 1024, 256, 64, 16$. All solutions are obtained with a 5 knotted spline (solid squares with dashed line) with a zero initial guess. Solid line represents the exact solution. Right: Effect of the particle seeding density ρ on the accuracy of the calculated solution (σ). Data shown are for $N = 1024$.

which is that after significant benefit for increases in density at low values of density, a plateau is attained for a large range of seeding density.

4.2 Generalisation

To demonstrate the general applicability of this technique, we extended the analysis to different channel depth with their appropriate optical configuration. These objectives are typical in μPIV as they are inexpensive and readily available. Figure 8 demonstrates the applicability of the technique to various depth of channels. The
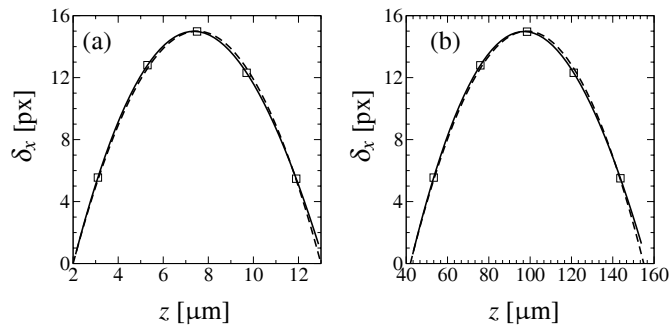

Fig. 8 Parabolic profile for typical objectives and associated channel depth. Left: channel from 2 to 13μm with a 20x0.3 objective. Right: 42 to 155μm with 5x0.12 objective.

11

selected range varies from few microns depth to over a hundred microns depth. More precisely, the notion of depth is purely arbitrary, just like the field of view in the laser plane, in a volumetric sense the field of view is selected by the practitioner through the choice of lenses cameras magnification tube etc.
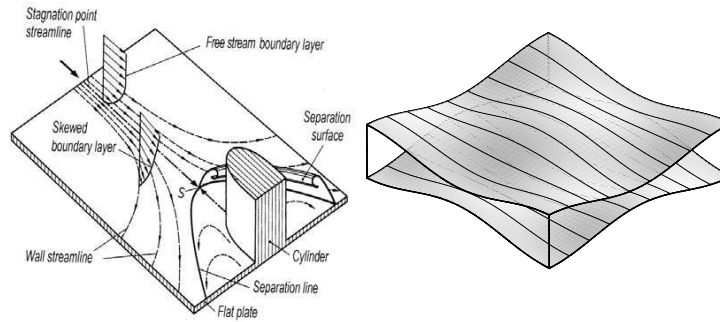

Fig. 9 Left: Sketch of a skewed boundary layer caused by a cylinder. Taken from Schlichting and Gersten (2003) ©Springer–Verlag 2000. Right: Example of a geometry producing skewed boundary-layer (Lo Jacono et al, 2005).

The final step of validation described in this paper is the more general case where the velocity profile is skewed. Figure 9 shows two examples of flow geometries that would produce such skewed boundary layers. In this case δ_y cannot be expressed as a simple linear function of δ_x and λ is curved as can be seen in Fig 10.
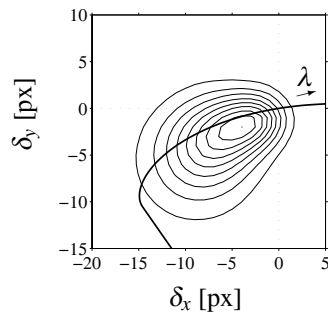

Fig. 10 (a) Average cross-correlation function for the skewed boundary layer flow. The curvilinear coordinate λ represents the relationship between δ_x and δ_y. Note that for this flow λ does not lie on the maximum envelope of the cross-correlation peak.

12

Figure 11 shows the calculated values of the displacement field δ_x and δ_y as a function of depth for the skewed boundary layer flow. Solid lines represent exact solution. Crosses and circles represent the δ_x and δ_y components, respectively, using the piece-wise linear approach. It can be seen in this general case that the technique has worked to a high degree of accuracy, completing the validation of the technique.
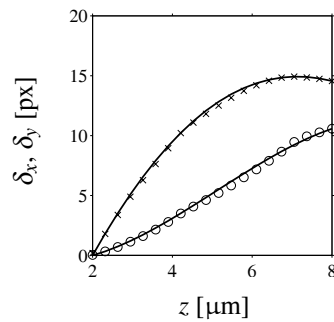

Fig. 11 Calculated values of the displacement field δ_x and δ_y as a function of depth for the skewed boundary layer flow. Solid lines represent exact solution. Crosses and circles represent δ_x and δ_y component, respectively, using the piece-wise linear approach.

5 Conclusions

A method has been proposed that allows 3D2C measurements to be made in any volume illuminated by a light sheet of finite thickness. The method is based on the decomposition of the cross-correlation function into various contributions at different depths in the light sheet. This technique does not suffer from many of the limitations of other techniques designed to improve the dimensionality of PIV. A number of examples of the viability of this technique have been demonstrated by use of synthetic images which simulate micro-PIV experiments. These examples vary from trivial cases of linear variation of one velocity component over depth to a general case where both velocity components vary by different complex functions over depth. This technique could be implemented in both macro and micro-PIV experiments. Furthermore, this technique could be expanded by the use of a second camera and performed in stereo to yield fully 3D3C velocity vector

13

field data with only two cameras. Alternatively in wall bounded flows, by using the continuity equation, one can recover out-of-plane velocity.

References

Adrian R, Yao C (1985) Pulsed laser technique application to liquid and gaseous flows and the scattering power of seed materials. Appl Optics 24:42–52

Arroyo M, Greated C (1991) Stereoscopic particle image velocimetry. Measurement Science and Technology 2:1181–1186

Barnhart D, Adrian R, Papen G (1994) Phase-conjugate holographic system for high-resolution particle image velocimetry. Applied Optics 33:7159–7170

Bourdon C, Olsen M, Gorby A (2004) Validation of an analytical solution for depth of correlation in microscopic particle image velocimetry. Measurement Science and Technology 15:318–327

Elsinga G, Scarano F, Wieneke B, van Oudheusen B (2006) Tomographic particle image velocimetry. Experiments in Fluids 41:933–947

Forouhar A, Liebling M, Hickerson A, Nasiraei-Moghaddam A, Tsai HJ, Hove J, Fraser S, Dickinson M, Gharib M (2006) The embryonic vertebrate heart tube is a dynamic suction pump. Science 312(5774):751 – 753

Fouras A, Dusting J, Hourigan K (2007a) A simple calibration technique for stereoscopic particle image velocimetry. Experiments in Fluids 42:799–810

Fouras A, Lo Jacono D, Hourigan K (2007b) Target-free Stereo PIV: a novel technique with inherent error estimation and improved accuracy. Experiments in Fluids (In Press)

Kahler C (2004) Investigation of spatio-temporal flow structure in the buffer region of a turbulent boundary layer by means of multiplane stereo PIV. Experiments in Fluids 36:114–130

Lo Jacono D, Plouraboué F, Bergeon A (2005) Weak-inertial flow between two rough surfaces. Physics of Fluids 17:63,602–63,612

Meinhart C, Wereley S, Gray M (2000a) Volume illumination for two-dimensional particle image velocimetry. Meas Sci Technol pp 809–814

14

Meinhart CD, Werely ST, Santiago JS (2000b) A PIV algorithm for estimating time-averaged velocity fields.
   Journal of Fluids Engineering 122:285–289

Olsen M, Adrian R (2000a) Brownian motion and correlation in particle image velocimetry. Optics and Laser
   Technology 32:621–627

Olsen M, Adrian R (2000b) Out-of-focus effects on particle image visibility and correlation in microscopic
   particle image velocimetry. Experiments in Fluids 29:S166–S174

Olsen M, Bourdon C (2003) Out-of-plane motion effects in microscopic particle image velocimetry. Journal
   of Fluids Engineering 125:895–901

Park J, Kihm K (2006) Three-dimensional micro-PTV using deconvolution microscopy. Experiments in Fluids
   40:491–499

Pereira F, Gharib M, Dabiri D, Modarress M (2000) Defocusing DPIV: A 3-component 3-D DPIV measure-
   ment technique. application to bubbly flows. Experiments in Fluids 29:S78–S84

Schlichting H, Gersten K (2003) Boundary-layer Theory, 8th edn. Springer–Verlag

Schroder A, Kompenhans J (2004) Investigation of a turbulent spot using multi-plane stereo particle image
   velocimetry. Experiments in Fluids 36:82–90

Willert C, Gharib M (1992) Three-dimensional particle imaging with a single camera. Experiments in Fluids
   12:353–358

Zhang J, Tao B, Katz J (1997) Turbulent flow measurement in a square duct with hybrid holographic PIV.
   Experiments in Fluids 23:373–381

Chapter 5

Conclusions

This thesis has presented six publications detailing a number of recent advances in the field of PIV. The body of the thesis has separated these advances into three chapters, treating each of the topics: Topographic PIV, Stereo PIV and Volumetric PIV.

5.1 Topographic PIV

The work described in the chapter on Topographic PIV relates to the use of PIV-like techniques and analyses to measure the free surface topography of a fluid flow. While these techniques are somewhat on the fringe of PIV, they have a number of applications. These applications include those studies for which the measurement of the free surface has direct utility. The most obvious of these types of studies are those utilising the hydraulic analogy. These techniques are also likely to be of use in studies where the free surface topography can be linked to the fluid pressure field.

While many researchers have worked on the development of techniques to measure the free surface topography, the techniques detailed in this chapter are largely based on the work of Tanaka et al (2000). The work described offers many significant advances. For the reference image topography technique (which only measures the free surface), the main advantages are an increase in data quality combined with a substantial decoupling of the data quality from specialised experimental skills. The Topographic PIV technique adds considerable utility to this technology though the availability of velocity data. It is believed that with these data, the relationship between pressure and topography will be even more important. An advance common to both papers is the utilisation of the knowledge that the topography is over-specified by the surface gradient field. While it is well understood that integration smoothes noise, the over-specification allows for an advanced integration technique that solves for the surface topography with very low sensitivity to errors inherent in the gradient data.

While these results are a significant addition to the field of surface topography, there is scope

for continued work on these ideas. This work would include experiments that investigate the relationship between topography and pressure. Also worth pursuing are numerical experiments to directly measure the sensitivity of the technique to various types of noise most likely to present in the measurement system.

5.2 Stereo PIV

With the maturity of classical PIV, practitioners are increasingly turning to more advanced variants of the technique. Perhaps the most common variant is stereo PIV. With this widespread use, any advances in SPIV technology will have an impact on a very large base of researchers. The chapter on Stereo PIV is based on two papers. The first paper describes a body of work on the most basic stereo configuration: two cameras utilising geometric reconstruction. The technology for the calibration technique described in these papers emerges directly from the research base of the calibration required for the Topographic techniques of the previous chapter.

The use of a contiguous target and PIV interrogation to derive the distortion map makes the process simple to implement, as much of the geometric analysis is no longer necessary. Furthermore, no interpolation is required since a common grid is used for both the distortion analysis and the flow analysis. Importantly, the calibration process also automatically takes into account any discrepancy between the field of view on the left and right camera images, thus reducing the sensitivity to camera misalignments, lens misalignments, or magnification differences.

A thorough error analysis of the geometric reconstruction has been performed. The measured ratios of σ_x and σ_z to σ_p agree closely with published predictions. The most accurate configuration for the measurement of Δx and Δz was determined to be a symmetric camera geometry, with small camera spacing for Δx and large camera spacing for Δz. The optimal configuration for overall measurement accuracy was found to be any geometry with a relative angle of $90°$ between cameras. Furthermore, it was found that under certain achievable circumstances, the error due to inaccurate measurement of camera geometry was zero. The level of measurement accuracy resulting from this new, simple technique may reduce the advantage in using more complicated SPIV techniques such as three-dimensional calibration.

The second paper in this chapter presents a novel, accurate and simple Stereo PIV technique utilising three cameras. The key feature of the new technique is the elimination of a separate calibration phase. The calibration data are measured concurrently with the PIV data by a third paraxial camera. This has the benefit of improving ease of use and reducing the time taken to obtain data. The new technique is rigorously validated using both pure translation and rotation

test cases. However, while this kind of validation is standard, it is shown that such validation is substantially limited and an improved validation process is required.

This third camera also significantly improves the accuracy of the resolved 3D vectors. The use of a least squares approach to the solution of the reconstruction equations further improves the utility of the technique by providing a robust and useful residual. While it has been shown that on an individual vector basis the residual is not meaningful, thorough error analysis demonstrates that on a global basis this residual is an accurate predictor of resolved vector errors. This powerful predictive tool has potential to be used in conjunction with any stereo technique (including those similar to Soloff et al (1997)), provided it solves the reconstruction process with a least-squares process.

These papers represent a significant increase in the level of understanding of the propagation of errors in SPIV measurements. The techniques described also allow for more simple implementation of SPIV. This is of substantial significance as set-up and calibration time can exceed the time required for experiments under many circumstances. In the case of the three-camera technique, considerable improvements to the robustness and accuracy of the measurements has been disseminated through these papers to the fluid mechanics community.

Logically following this work is a study on the further development of flow cases to test and validate SPIV techniques. All the most commonly employed SPIV techniques could be quantitatively compared with these test cases. These experiments would involve the powerful combination of CFD to evaluate expected velocity field data, SPIV to measure these data and least squares residuals to predict the statistics of the differences.

5.3   Volumetric PIV

The chapter on Volumetric PIV describes related set of advances in two much newer variants of PIV: micro PIV and X-Ray PIV.

The first paper in this chapter demonstrates the viability of X-ray PIV. Furthermore, several flaws in the approach of investigators who have previously used X-ray PIV to measure 2D velocity vector fields of flows that vary over the direction, z, of the X-ray beam, have been highlighted. A useful technique for extrapolating correct 2D vector fields and correlation peaks has been demonstrated. This technique allows not only accurate measurement of 2D vector fields but also interrogation of correlation peaks corresponding to velocity probability distribution in the z direction. Under certain circumstances, this probability density function (PDF) can be used to determine the velocity profile over z. The Poiseuille flow through a pipe has been measured in a 3D sense

using this technique. The velocity data are well matched to the expected axi-symmetric parabolic velocity flow profile.

The author anticipates that in future, similar measurements can be made with fewer or no assumptions about the nature of the flow, by extracting additional information during image acquisition. The most likely method for gaining this information would be through the measurement of the flow volume from multiple perspectives. This technique would combine the advantages of both SPIV and X-ray computed tomography.

The idea of extracting not only a single velocity that represents the modal velocity in a region, but of extracting the PDF has been taken further in the next paper.

A method has been proposed that allows three-dimensional, two component (3D2C) measurements to be made in any volume illuminated by a light sheet of finite thickness. The method is based on the decomposition of the cross-correlation function into various contributions at different depths in the light sheet. This technique does not suffer from many of the limitations of other techniques that are designed to improve the dimensionality of PIV. A number of examples of the viability of this technique have been demonstrated by use of synthetic images that simulate micro-PIV experiments. These examples vary from trivial cases of linear variation of one velocity component over depth to a general case where both velocity components vary by different complex functions over depth. This technique could be implemented in both macro and micro-PIV experiments. Furthermore, this technique could be expanded by the use of a second camera and performed in stereo to yield fully 3D3C velocity vector field data with only two cameras. Alternatively in wall bounded flows, by using the continuity equation, one can recover out-of-plane velocity.

This work forms a platform from which a significant number of projects are being undertaken. Experimental work to validate the technique described in this paper is progressing well and will be published shortly. Furthermore, the ideas for this work, which originated in the X-Ray PIV study, have great scope to feed back into that work.

5.4 Final Remarks

One common thread throughout this thesis is an attention to rigorous validation against known test cases. In the recent review article, Adrian (2005) comments that this is sorely lacking from the field of PIV technique development. Another common thread is rigorous error and sensitivity analyses, which in the author's opinion should become much more prevalent and should also become one standard against which works in this field are measured for suitability for publication.

These papers, as a single body of work, represent a significant contribution to the field of PIV. While the papers focus on the seemingly different areas of Topographic, Stereo and Volumetric PIV, they are all underpinned by the same body of knowledge. This is highlighted by the flow of ideas and technology between these studies. This flow of ideas also indicates that the likelihood of future publication in any of these areas is strengthened by the body of work as a whole.

Bibliography

Adrian R (1991) Particle-imaging techniques for experimental fluid mechanics. Annual Review of Fluid Mechanics 23:261–304

Adrian R (2005) Twenty years of particle image velocimetry. Experiments in Fluids 23:261–304

Anayiotos A, Jones S, Giddens D, Glagov S, Zarins C (1994) Shear stress at a compliant model of the human carotid bifurcation. Journal of Biomechanical Engineering 116:98–106

Arabadzhi V (1996) On the active cancellation of ship waves. Experiments in Fluids 20:225–226

Arroyo M, Greated C (1991) Stereoscopic particle image velocimetry. Measurement Science and Technology 2:1181–1186

Barnhart D, Adrian R, Papen G (1994) Phase-conjugate holographic system for high-resolution particle image velocimetry. Applied Optics 33:7159–7170

Bourdon C, Olsen M, Gorby A (2004) Validation of an analytical solution for depth of correlation in microscopic particle image velocimetry. Measurement Science and Technology 15:318–327

Braza M, Chassaing P, Minh H (1986) Numerical study and physical analysis of the pressure and velocity fields in the near wake of a circular cylinder. Journal of Fluid Mechanics 169:79–130

Brocher E, Makhsud A (1997) New look at the screech tone mechanism of underexpanded jets. Eur J Mech B/Fluids 16:877

Brucker C (1997) 3d scanning piv applied to an air flow in a motored engine using digital high-speed video. Measurement Science and Technology 8:1480–1492

Buchanan A, Macartney R, Thompson M, Brocher E, Hourigan K (2007) Hydraulic analogy study of supersonic rectangular jet screech control with cylinders. Accepted for publication in AIAA Journal

Calluaud D, David L (2004) Stereoscopic particle image velocimetry measurements of the flow around a surface-mounted block. Experiments in Fluids 36:53–61

Chen D, Jerka G (1997) Absolute and convective instabilities of plane turbulent wakes in a shallow water layer. Journal of Fluid Mechanics 338:157–172

Chen J, Katz J (2005) Elimination of peak-locking error in PIV analysis using the correlation mapping method. Measurement Science and Technology 16:1605–1618

Cochard A, Ancey C (2007) Tracking the free surface of time-dependent flows: image processing for the dam-break problem. Experiments in Fluids Online First:1–13

Dabiri D, Gharib M (2001) Simultaneous free-surface deformation and near-surface velocity measurements. Experiments in Fluids 30:381–390

Dusting J, Sheridan J, Hourigan K (2006) A fluid dynamics approach to bioreactor design for cell and tissue culture. Biotechnology and Bioengineering 94:1196–1208

Elsinga G, Scarano F, Wieneke B, van Oudheusen B (2006) Tomographic particle image velocimetry. Experiments in Fluids 41:933–947

Escudier M (1984) Observations of the flow produced in a cylindrical container by a rotating endwall. Experiments in Fluids 2:189–196

Fei R, Merzkirch W (2004) Investigations of the measurement accuracy of stereo particle image velocimetry. Experiments in Fluids 37:559–565

Fey U, Konig M, Eckelmann H (1998) A new Strouhal Reynolds - number relationship for the circular cylinder in the range $47 < Re < 2 \times 10^5$. Physics of Fluids 10-7:1547–1550

Fomim N, Lavinskaja E, Merzkirch W, Vitkin D (1999) Speckle photography applied to statistical analysis of turbulence. Optics & Laser Tech 31:13

Forouhar A, Liebling M, Hickerson A, Nasiraei-Moghaddam A, Tsai HJ, Hove J, Fraser S, Dickinson M, Gharib M (2006) The embryonic vertebrate heart tube is a dynamic suction pump. Science 312(5774):751 – 753

Fouras A, Soria J (1998) Accurate out-of-plane vorticity calculation from in-plane velocity vector field data. Experiments in Fluids 25:409–430

Fouras A, Hourigan K, Kawahashi M, Hirahawa H (2006) An improved free surface topographic technique. Journal of Visualization 9:49–56

Fouras A, Dusting J, Hourigan K (2007*a*) A simple calibration technique for stereoscopic particle image velocimetry. Experiments in Fluids 42:799–810

Fouras A, Dusting J, Lewis R, Hourigan K (2007*b*) Three-dimensional synchrotron x-ray particle image velocimetry. Journal of Applied Physics 102, 064916:1–6

Fouras A, Lo Jacono D, Hourigan K (2007*c*) Target-free Stereo PIV: a novel technique with inherent error estimation and improved accuracy. Experiments in Fluids (Available Online)

Fouras A, Lo Jacono D, Sheard G, Hourigan K (2007*d*) Measurement of instantaneous velocity and surface topography of a cylinder at low reynolds number. In: Braza M, Hourigan K (eds) In Proceedings IUTAM Symposium on Unsteady Separated Flows and Their Control

Fouras A, Lo Jacono D, Hourigan K (2008) Volumteric correlation piv: a new technique for 3D velocity vector field measurement. Experiments in Fluids (Under Review)

Fu H, Rockwell D (2005*a*) Shallow flow past a cylinder: Control of near wake. Journal of Fluid Mechanics 539:1

Fu H, Rockwell D (2005*b*) Shallow flow past a cylinder: transition phenomena at low Reynolds number. Journal of Fluid Mechanics 540:75–97

Grant I (1997) Particle image velocimetry: a review. In: In Proceedings Instn Mech Engnrs, vol 211 Part C, pp 55–76

Green R, Gerrard J (1993) Vorticity measurements in the near wake of a circular cylinder. Journal of Fluid Mechanics 246:657–691

He X, Ku D (1996) Pulsatile flow in the human left coronary artery bifurcation: average conditions. Journal of Biomechanical Engineering 118:74–82

Hori T, Sakakibara J (2004) High-speed scanning stereoscopic piv for 3d vorticity measurement in liquids. Measurement Science and Technology 15:1067–1078

Huang H, Fiedler H, Wang J (1993) Limitation and improvement of piv. 2. particle image distortion: a novel technique. Experiments in Fluids 15:263–273

Hughes H, Grant H, Chappell RW (1977) A fast response surface-wave slope meter and measured wind-wave moments. Deep-Sea Research 24:1211

Jahne B, Klinke J, Waas S (1994) Imaging of short ocean wind waves: a critical theoretical review. J Opt Soc Am A 11:2197

Kahler C (2004) Investigation of spatio-temporal flow structure in the buffer region of a turbulent boundary layer by means of multiplane stereo PIV. Experiments in Fluids 36:114–130

Ku D, Giddens D (1987) Laser doppler anemometer measurements of pulsatile flow in a model carotid bifurcation. Journal of Biomechanical Engineering 20:407–421

Lawson N, Wu J (1997a) Three-dimensional particle image velocimetry: error analysis of stereoscopic techniques. Measurement Science and Technology 8:894–900

Lawson N, Wu J (1997b) Three-dimensional particle image velocimetry: experimental error analysis of a digital angular stereoscopic system. Measurement Science and Technology 8:1455–1464

Lee SJ, Kim GB (2003) X-ray particle image velocimetry for measuring quantitative flow information inside opaque objects. Journal of Applied Physics 94:3620–3623

Lee SJ, Kim GB (2005) Synchrotron microimaging technique for measuring the velocity fields of real blood flows. Journal of Applied Physics 97:064,701

Lewis R (2004) Medical phase contrast x-ray imaging: current status and future prospects. Physics in medicine and Biology 49:3573–3583

Lewis R, Yagi N, Kitchen M, Morgan M, Paganin D, Siu K, Pavlov K, Williams I, Uesugi K, Wallace M, Hall C, Whitley J, Hooper S (2005) Dynamic imaging of the lungs using x-ray phase contrast. Physics in medicine and Biology 50:5031–5040

Lindken R (2006) Stereoscopic micro particle image velocimetry. Experiments in Fluids 41:161–171

Lo Jacono D, Plouraboué F, Bergeon A (2005) Weak-inertial flow between two rough surfaces. Physics ofFluids 17:63,602–63,612

Lopez J (1990) Axisymmetrical vortex breakdown. part 1. confined swirling flow. Journal of Fluid Mechanics 221:533–552

Meinhart C, Wereley S, Gray M (2000*a*) Volume illumination for two-dimensional particle image velocimetry. Meas Sci Technol pp 809–814

Meinhart CD, Werely ST, Santiago JS (1999) PIV measurements of a microchannel flow. Experiments in Fluids 27:414–419

Meinhart CD, Werely ST, Santiago JS (2000*b*) A PIV algorithm for estimating time-avergaed velocity fields. Journal of Fluids Engineering 122:285–289

Meunier P, Leweke T (2003) Analysis and minimization of errors due to high gradients in particle image velocimetry. Experiments in Fluids 35:408–421

Moore J, Xu C, Glagov S, Zarins C, Ku D (1994) Fluid wall shear stress measurements in a model of the human abdominal aorta: oscillatory behaviour and relationship to atherosclerosis. Atherosclerosis 110(2):225–240

Olsen M, Adrian R (2000*a*) Brownian motion and correlation in particle image velocimetry. Optics and Laser Technology 32:621–627

Olsen M, Adrian R (2000*b*) Out-of-focus effects on particle image visibility and correlation in microscopic particle image velocimetry. Experiments in Fluids 29:S166–S174

Olsen M, Bourdon C (2003) Out-of-plane motion effects in microscopic particle image velocimetry. Journal of Fluids Engineering 125:895–901

Park J, Kihm K (2006) Three-dimensional micro-PTV using deconvolution microscopy. Experiments in Fluids 40:491–499

Pereira F, Gharib M, Dabiri D, Modarress M (2000) Defocusing DPIV: A 3-component 3-D DPIV measurement technique. application to bubbly flows. Experiments in Fluids 29:S78–S84

Perret L, Braud P, Fourment C, David L, Delville J (2006) 3-component acceleration field measurement by dual-time stereoscopic particle image velocimetry. Experiments in Fluids 40:813–824

Prasad A (2000) Stereoscopic particle image velocimetry. Experiments in Fluids 29:103–116

Prasad A, Adrian R (1993) Stereoscopic particle image velocimetry applied to liquid flows. Experiments in Fluids 15:49–60

Preiswerk E (1938) Application of the methods of gas dynamics to water flows with a free surface. Mitteilungen der Institut fr Aerodynamik, ETH, Zurich 7:934–935

Press WH, Flannery BP, Teukolsky SA, Vetterling WT (1992) Numerical Recipes in C: The Art of Scientific Computing, 2nd edn. Cambridge University Press, Cambridge (UK) and New York

Pu Y, Meng H (2000) An advanced off-axis holographic particle image velocimetry (hpiv) system. Experiments in Fluids 29:184–197

Radermacher J, Chavan A, Bleck J, Vitzthum A, Stoess B, Gebel M, Galanski M, Koch K, Haller H (2001) Use of doppler ultrasonography to predict the outcome of therapy for renal-artery stenosis. New England Journal of Medicine 344:410–417

Raffel M, Willert CE, Kompenhans J (1998) Particle Image Velocimetry: A Practical Guide. Springer, Berlin, Germany

Ross R (1993) The pathogenesis of atherosclerosis - a perspective for the 1990s. Nature 362:801–809

Santiago JG, Wereley ST, Meinhart CD, Beebe DJ, Adrian RJ (1998) A particle image velocimetry system for microfluidics. Experiments in Fluids 25:316–319

Scarano F, Riethmuller ML (2000) Advances in iterative multigrid piv image processing. Experiments in Fluids 29:S051–S060

Scarano F, David L, Bsibsi M, Calluaud D (2005) S-PIV comparative assessment: image dewarping+misalignment correction and pinhole+geometric back projection. Experiments in Fluids 39:257–266

Schenk O, Gartner K (2004) Solving unsymmetric sparse systems of linear equations with pardiso. Future Generation Computer Systems 20 3:475–487

Schlichting H, Gersten K (2003) Boundary-layer Theory, 8th edn. Springer–Verlag

Schroder A, Kompenhans J (2004) Investigation of a turbulent spot using multi-plane stereo particle image velocimetry. Experiments in Fluids 36:82–90

Seeger A, Affeld K, Goubergrits L, Kertzscher U, Wellnhofer E (2001) X-ray-based assessment of the three-dimensional velocity of the liquid phase in a bubble column. Experiments in Fluids 31:193–201

Soloff SM, Adrian RJ, Liu ZC (1997) Distortion compensation for generalized stereoscopic particle image velocimetry. Measurement Science and Technology 8:1441–1454

Sorensen J, Christensen E (1995) Direct numerical simulation of rotating fluid-flow in a closed cylinder. Physics of Fluids 7(4):764–778

Sorensen JN, Loc TP (1989) High-order axisymmetric Navier–Stokes code: Description and evaluation of boundary conditions. Int J Num Methods Fluids 9:1517–1537

Spohn A, Mory M, Hopfinger EJ (1993) Observations of vortex breakdown in an open cylindrical container with a rotating bottom. Experiments in Fluids 14:70–77

Spohn A, Mory M, Hopfinger E (1998) Experiments on vortex breakdown in a confined flow generated by rotating disk. Journal of Fluid Mechanics 370:73–99

Tanaka G, Okamoto K, Madarame H (2000) Experimental investigation on the interaction between a polymer solution jet and a free surface. Experiments in Fluids 29:178–183

Thompson MC, Hourigan K (2003) The sensitivity of steady vortex breakdown bubbles in confined cylinder flows to rotating lid misalignment. Journal of Fluid Mechanics 496:129.138

Vennemann P, Lindken R, Westerweel J (2007) In vivo whole-field blood velocity measurement techniques. Experiments in Fluids 42:495–511

Vogel H (1968) Experimentelle ergebnisse über die laminare strömung in einem zylindrischen gehäuse mit darin rotierender scheibe. Bericht 6, Max–Planck-Institut für Strömungdforschung, Göttingen

Westerweel J (1994) Efficient detection of spurious vectors in particle image velocimetry data. Experiments in Fluids 16:236–247

Westerweel J, Scarano F (2005) Universal outlier detection for piv data. Experiments in Fluids 39:1096–1100

Westerweel J, Dabiri D, Gharib M (1997) The effect of a discrete window offset on the accuracy of cross-correlation analysis of digital piv recordings. Experiments in Fluids 23:20–28

Wieneke B (2005) Stereo-PIV using self-calibration on particle images. Experiments in Fluids 39:267–280

Willert C (1997) Stereoscopic digital particle image velocimetry for application in wind tunnel flows. Measurement Science and Technology 8:1465–1479

Willert C, Gharib M (1991) Digital particle image velocimetry. Experiments in Fluids 10:183–193

Willert C, Gharib M (1992) Three-dimensional particle imaging with a single camera. Experiments in Fluids 12:353–358

Williamson CHK (1988*a*) Defining a universal and continous Strouhal-Reynolds number relationship for the laminar vortex shedding of a circular-cylinder. Physics of Fluids 31(10):2742–2744

Williamson CHK (1988*b*) Oblique and parallel modes of vortex shedding in the wake of a circular cylinder at low Reynolds numbers. Journal of Fluid Mechanics 206:579–672

Zang W, Prasad A (1997) Performance evaluation of a scheimpflug stereocamera for particle image velocimetry. Applied Optics 36:8738–8744

Zhang J, Tao B, Katz J (1997) Turbulent flow measurement in a square duct with hybrid holographic piv. Experiments in Fluids 23:373–381

Zhang X, Dabiri D, Gharib M (1994) A novel technique for surface elevation mapping. Physics of Fluids 6:S11